Hydrogen production through photoreforming of oxygenated organic substrates over Cu/TiO_2 catalysts

Thesis by
Laura Clarizia

Degree of Doctor of Philosophy
in

INDUSTRIAL PRODUCT AND PROCESS ENGINEERING (XXIX)

University of Naples "Federico II"
School of Polytechnic and Basic Sciences
Department of Chemical Engineering, Materials and Industrial Production (DICMAPI)

2014 - 2017

Hydrogen production through photoreforming of oxygenated organic substrates over Cu/TiO_2 catalysts

by

Laura Clarizia

Tutor: Prof. R. Andreozzi, Prof. R. Marotta, Prof. D. D. Dionysiou

Co-Tutor: Dr. I. Di Somma

Course coordinator: Prof. G. Mensitieri

ABSTRACT

Hydrogen is the ideal candidate to fulfill the growing energy demand in a sustainable manner because of its high energy content and no emission of greenhouse gases from its combustion. Currently most of hydrogen generation techniques involve the employment of fossil fuels, with consequent production of toxic greenhouse gases. The possibility to produce hydrogen by means of photocatalytic processes using the solar radiation as energy source fits in perfectly with the switch to a more sustainable energy production. The solar photocatalytic hydrogen generation can be achieved by reforming organic substances contained in civil or industrial wastewaters. This could allow to combine water decontamination with production of an energy carrier starting from a renewable source, the solar radiation.

Hydrogen production through photoreforming of organic species using copper-modified TiO_2 *photocatalysts is attracting a considerable attention during last years. It is reported that the doping of* TiO_2 *with copper species helps enhance to separate the electron-hole pairs, thus reducing the occurrence of the recombination reaction, and extend the light absorption to the visible range of the solar spectrum. The choice of copper is supported by its low-cost and abundance in Earth's crust.*

In particular, the use of catalysts prepared by in situ photodeposition processes, with nanometric size, could represent a straightforward promising strategy to improve the process efficiency.

In this study, the production of hydrogen by photocatalytic reforming of oxygenated organic species was investigated using metal copper-modified TiO_2 *nanoparticles, prepared "in situ" by reduction of cupric ions.*

The behavior of different alcohols and organic acids to undergo photoreforming with hydrogen production was investigated and compared. A characterization of the catalysts recovered at the end of the runs revealed the formation of zero-valent copper nanoparticles on the catalysts surface.

The effect of adopting different crystallographic phases of TiO_2 *was also assessed. In particular, three* TiO_2 *commercial samples of different crystalline phases (mixed-phase P25, pure anatase and pure rutile) were employed to prepare Cu-doped* TiO_2 *materials by in situ copper photo-deposition. The resulting samples were extensively characterized by several complementary techniques and tested as photocatalysts for hydrogen production through photoreforming of alcohols. Correlations between hydrogen production rates and physical-*

chemical properties (structural, compositional and optical properties) of the samples are discussed. The analyses highlighted the major roles played by physical sizes and surface properties of TiO_2 *particles in determining the morphology, the dispersion of zero-valent copper nanoparticles on* TiO_2 *surface and, ultimately, the photocatalytic performances.*

A modeling investigation was performed through the development of a simplified kinetic model taking into account the mass balance equations for the main reactive species involved in the photocatalytic system. The kinetic model was tested to predict hydrogen generation rates for experimental runs carried out at different initial concentrations of sacrificial agent (methanol and glycerol) and at varying photocatalyst load. The modeling investigation allowed to estimate for the first time the equilibrium adsorption constants and the kinetic constant for the hole-capture by sacrificial agents, as well as the quantum yield and the rate constant of electron-hole recombination for the copper modified-TiO_2 *nano-photocatalyst.*

The simultaneous presence in the aqueous matrix of an inorganic ion, that is chloride, was also investigated when formic acid was adopted as sacrificial agent. The effect on hydrogen generation rate of the initial concentrations of formic acid, chloride and cupric ion, and pH values was evaluated. These experimental outcomes were rationalized within a consistent reaction mechanism able to predict the system behavior under different operating conditions.

Therefore, this critical literature review has been performed with the aim of providing a complete and reliable approach to promote new competitive processes able to use waste organic streams for hydrogen generation through photacatalytic system based on solar energy.

INDEX

1 Background 1

2 State of the art 10

3 Aims of the thesis 42

5 Results I: *In-situ* photodeposited Cu-TiO_2 catalyst for phoreforming of organics

6 Results II: Effect of different crystalline phases

7 Results III: Kinetic modeling of H_2 generation over nano-Cu/TiO_2 catalyst through photoreforming of alcohols

8 Results VI: Photoreforming of formic acid in the presence of Cl^-, Cu(II), and TiO_2 suspended particles

List of Figures

List of Tables

1. Background

1.1 Hydrogen as en energy vector

Hydrogen represents as an important energy carrier for the future due to its high energy content and the absence of greenhouse-responsible and toxic emissions during its combustion [1]. It undergoes a clean combustion reaction with oxygen ($r_{1.1}$) to generate energy ($\Delta H = 120\ MJ/kg$).

$$2H_2{}^g + O_2{}^g \rightarrow 2H_2O^g \qquad r_{1.1}$$

As shown in Table 1.1, hydrogen has the highest energy content amongst different fuels.

Table 1.1: Energy content (MJ/kg) of different fuels [2].

Fuel Energy content	**(MJ/kg)**
Hydrogen	120
Liquefied natural gas	54.4
Propane	49.6
Automotive gasoline	46.4
Automotive diesel	45.6
Ethanol	29.6
Methanol	19.7
Coke	27
Wood (dry)	16.2

As hydrogen can be found on earth in combination with other elements, its industrial availability is closely related to production processes which starts from substances containing it. Such substances may be currently represented by fossil fuels (i.e., coal, oil, natural gas), biomasses [3], organic substances eventually contained in civil or industrial wastewaters, or by the water itself [4]. In particular, hydrogen is usually produced as syngas component from fossil fuels by steam reforming and water gas shift processes [5]. Further minor technologies for hydrogen generation include chemical, electrochemical, thermal, and biological processes [6-8]. The main sources of hydrogen production, together with their percentage, are reported in Figure 1.1.

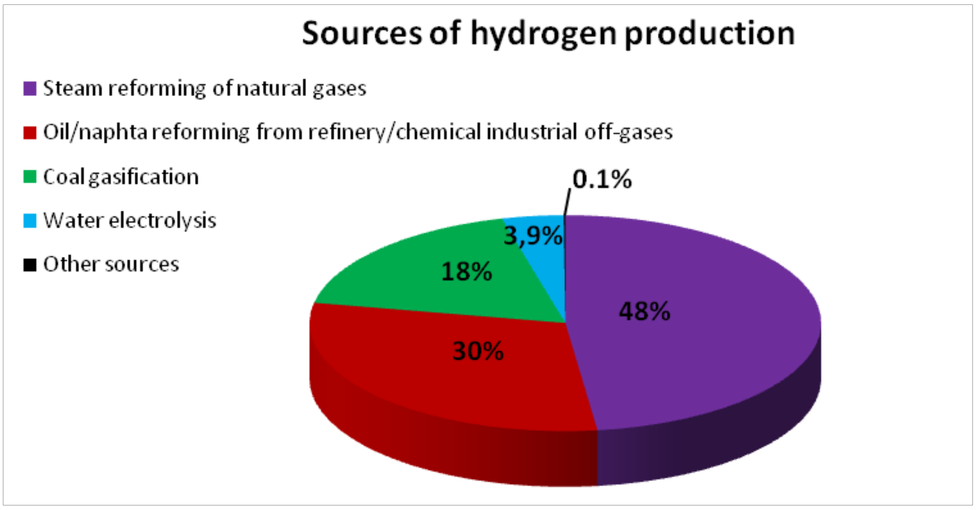

Figure 1.1: Main sources for hydrogen generation [3].

Although hydrogen production from fossil fuels is an established technology, such raw materials are unappealing for the future due to their unrenewable nature and the emission of greenhouse gases (carbon dioxide) to ensure the energy required for hydrogen production processes.

The attractive possibility to produce hydrogen by adopting solar energy may allow to employ a fully renewable energy source and avoid irreversible effects on the environment. As regards solar energy, hydrogen generation can be achieved by means of thermo-chemical [9], photo-electrochemical, and photo-chemical processes [10]. In particular, photochemical processes require the adoption of catalysts able to absorb the solar radiation, in order to promote electrons to the higher energy levels needed for hydrogen production. Photocatalytic processes for hydrogen production in aqueous solutions include water photosplitting [11] and photoreforming of organic species [12].

1.2 Photocatalytic processes for hydrogen generation

The generation of hydrogen from water or organic substances contained in industrial or civil wastewaters may be achieved by means of photocatalytic processes exploiting the solar radiation arriving daily on earth.

Two different approaches can be adopted for the photocatalytic hydrogen production: 1) photocatalytic water splitting and 2) photocatalytic reforming of organics.

1.2.1 Photocatalytic water splitting

The overall reaction of photocatalytic water splitting consists of water decomposition, which gives rise to the formation of hydrogen and oxygen gases ($r_{1.2}$).

$$H_2O^l \rightarrow H_2{}^g + 0.5O_2{}^g \qquad r_{1.2}$$

As shown in Figure 1.2, such method relies on the capability of water to be reduced and oxidized by reacting with photogenerated electrons and positive holes (generated after semiconductor catalyst irradiation), respectively [4,13,14].

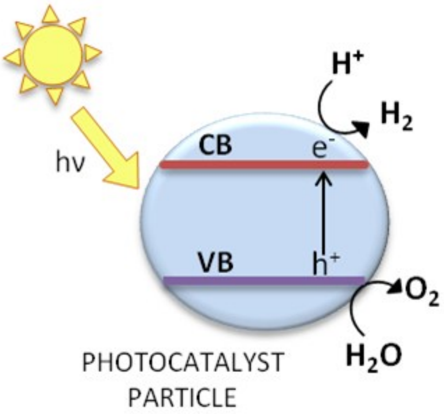

Figure 1.2: Schematic illustration of water photosplitting. Oxidation of water by positive holes in the valence band (VB) and reduction of proton by photogenerated electrons in the conduction band (CB).

The back reaction between hydrogen and oxygen regenerating water is kinetically and thermodynamically favored in photocatalytic water splitting. With the aim of avoiding hydrogen and oxygen recombination, photocatalytic processes may be performed by employing organic hole scavengers under inert atmosphere.

1.2.2 Photoreforming of organics

As shown in Figure 1.3, the so-called photocatalytic reforming is based on the ability of some organic species, named sacrificial agents, to donate electrons to the positive holes of the irradiated photocatalyst and be oxidized generating protons ions, which are reduced to hydrogen by photogenerated electrons. No oxygen gas generation is recorded in photocatalytic reforming processes.

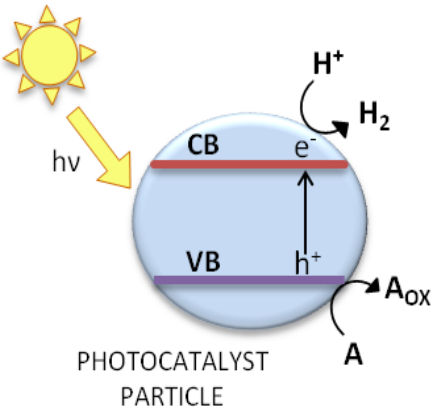

Figure 1.3: Schematic illustration for the photoreforming process. Oxidation of organics (A) by positive holes in the valence band (VB) and reduction of proton ions by photogenerated electrons in the conduction band (CB).

Short chain alcohols (e.g., methanol, ethanol and glycerol), carboxylic acids, (e.g., formic acid), and carbohydrates (e.g., glucose) are the organic species most commonly adopted in photoreforming processes [15,16]. The possibility of using industrial and civil wastewater streams containing such organics species can be considered, thus leading to a combined process of wastewater treatment with simultaneous hydrogen generation.

1.2.3 Photocatalytic processes for hydrogen generation: experimental setups

Both photocatalytic water splitting and reforming of organics may be performed through different experimental setups. The first method consists of a system in which the photocatalyst is merely suspended in solution; the second approach employs a photoelectrochemical cell [17] with the catalyst immobilized on a photoanode. As regards irradiated photoelectrochemical cells, water (in photosplitting) or organic species (in photoreforming) are oxidized at the photoanode, whereas protons are reduced at the cathode in a second compartment, being the two electrodes electrically connected (Fig. 1.4).

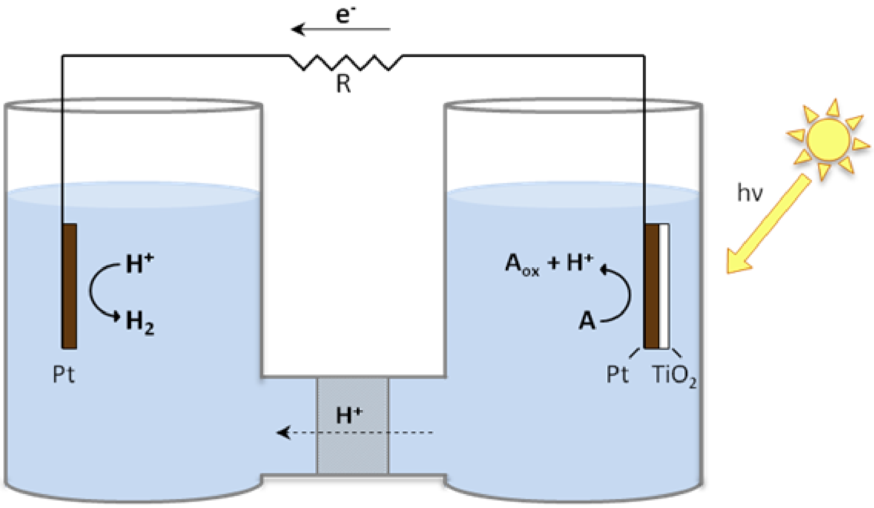

Figure 1.4: Photoelectrochemical cell for photoreforming. Oxidation of organics (A) at the anode (i.e., Pt and TiO_2) and proton production; proton migration to the anodic compartment through the ion-permeable membrane; proton reduction at the cathode (i.e., Pt).

A combination of photosplitting and photoreforming processes is feasible by adopting selected inorganic electron donors (i.e., I^- or Fe^{2+}). The oxidized forms of such species may be reduced on a second photocatalyst, thus enabling simultaneous water oxidation and oxygen formation [18]. For example, two photocatalysts may be properly selected and suspended in the same solution in the case of iodide: a first catalysts on which protons (or water) reduction along with iodide to iodate oxidation occur, and (ii) a second one allowing a further iodate to iodide reduction while water is oxidized to oxygen. The resulting overall reaction is water photosplitting without any sacrificial organic consumption [19].

1.3 Effective photocatalyst hallmarks

In general, an efficient photocatalyst needs have the following characteristics [20]:

- to be capable to absorb in the UV-Vis region of the solar spectrum and to actually use this energy to generate electron-hole pairs. In this region, about 50% of solar energy is concentrated and, in particular, about 45% is in the visible range. The availability of photocatalysts capable of absorbing in the visible range of the electromagnetic spectrum may, in principle, guarantee the capture and storage in the photoproducts of a significant part of the energy emitted by the sun, provided that the energy absorbed is actually used to generate charge transporters (photogenerated electrons and holes);

- to be capable to immediately separate these pairs transferring electrons and holes at the liquid-semiconductor junction, where they participate to half-reactions; it is well known that photogenerated electrons and positive holes can recombine:

$$e^- + h^+ \rightarrow heat \qquad r_{1.3}$$

thus reducing the efficiency of the process of interest, including hydrogen generation. The incorporation in the photocatalyst of species capable of promoting this separation is necessary to achieve a significant efficiency. It has been reported that for any photocatalyst, to be considered commercially viable, it has to display an efficiency of overall energy capture of about 15% in the visible region of the electromagnetic spectrum [21];

- to be characterized by an electronic structure which makes the half-reactions of interest thermodynamically feasible. As indicated in Figures 1.2 and 1.3, the charge transporters formed upon the absorption of the radiation are allocated on electronic bands which are characterized by different potentials. In Figure 1.5, the importance of the position of energy bands in the semiconductor photocatalyst (e.g., TiO_2) is highlighted. As a matter of fact, the capability of photogenerated electrons to reduce protons (or water) is strictly related to the position of the conduction band (CB) potential in the photocatalyst hosting them, which must be lower than that of the H^+/H_2 couple, as shown in Figure 1.5. At the same time, the potential of the valence band (VB), in which the holes are present, has to be higher than that of the H_2O/O_2 couple for water photosplitting, or suitable for the organic species (e.g., methanol and formaldehyde) oxidation in photoreforming (Fig. 1.5);
- to be characterized by surface active sites that make possible the occurrence of these reactions.

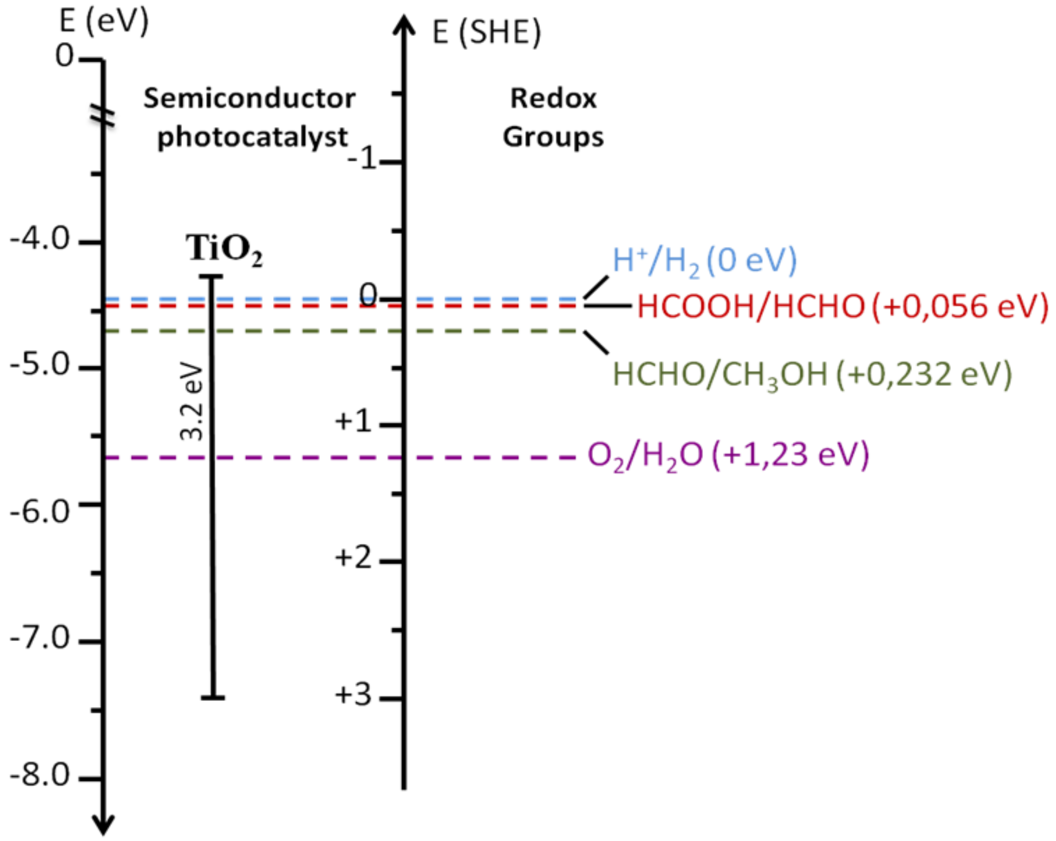

Figure 1.5: Positions of electronic bands of TiO_2 (anatase) and energy levels of some selected redox couples (data sources: [22], [23], [24],[25]). The energy scale is reported referring either to the vacuum level or to the Standard Hydrogen Electrode (SHE).

Metal oxides of transition elements whose cations show a d^0 or d^{10} configuration (Ti^{4+}, Zr^{4+}, Nb^{5+}, Ta^{5+}, W^{6+}, Ce^{4+}, Ga^{3+}, In^{3+}, Ge^{4+}, Sn^{4+}, Sb^{5+}) have been so far successfully adopted for water splitting tests [4].

1.4 Titanium dioxide

TiO_2, in different crystalline forms, pure or properly modified, is one of the most investigated photocatalysts due to its great availability and low cost [20]. However, the properties of TiO_2, both in anatase or rutile forms, for water photosplitting or photoreforming, are not particularly inspiring since this solid is characterized by an electronic band structure which allows to absorb radiation only in UV range and with a significant occurrence of the recombination reaction, which greatly contributes to lower the efficiency of the process. Many of these aspects are treated in details in several excellent reviews which have been published so far mainly for water photosplitting [4,18,26,27].

In the preparation of TiO_2-based catalysts, for both methods of hydrogen generation, the general approach followed by researchers is the use of some co-catalysts, mainly represented by noble metals, combined with the solid semiconductor [28,29]. These species, once deposited on the semiconductor surface, are believed to act as electron traps which significantly reduce the parasitic recombination reaction between photogenerated electrons and holes, responsible for the low efficiencies recorded on pure TiO_2 (Fig. 1.6), and to kinetically favor the reduction of water (in the case of splitting) or of proton ions (photoreforming).

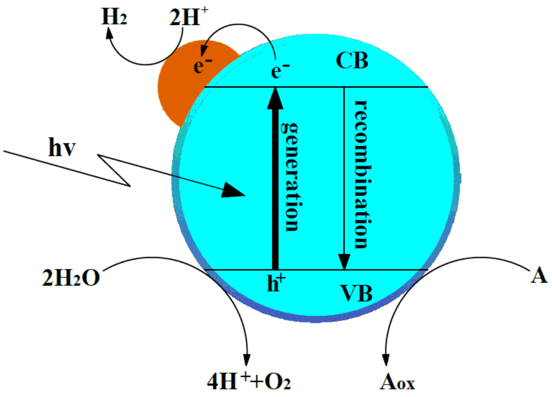

Figure 1.6: Effect of the incorporation of metal co-catalysts on the photocatalyst surface.

Another noticeable strategy to prevent the e^--h^+ recombination reaction is that of coupling photocatalyst particles with photosensitizers [30]. As shown in Figure 1.7, in these systems photogenerated electrons from the excited state of the sensitizers (S) can be quickly transferred to the CB of TiO_2, while the positive holes remain in the sensitizer, leading to an effective charge separation [30].

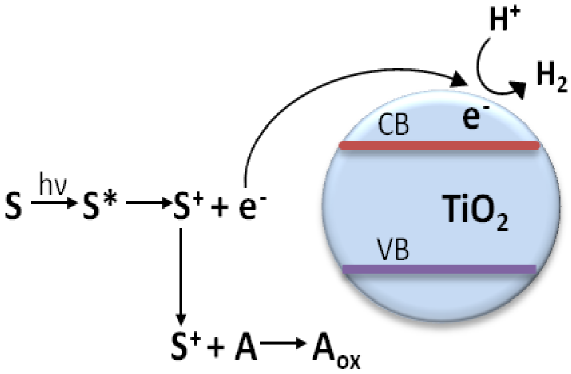

Figure 1.7: Mechanism of electron transfer in photosensitized systems.

Moreover, a growing interest is also nowadays recorded among researchers to extend the TiO_2 absorption capability to capture the more abundant fraction of the solar radiation arriving on earth represented by that contained in the visible light range [4]. To this purpose, several approaches have so far been adopted to prepare some photocatalysts for hydrogen generation (e.g., for water photosplitting). Among these methods the use of metal or non-metal doping to obtain narrower band gaps, or that of dye sensitizers, have often been reported [31-35].

2. State of the art

2.1 Copper modified-TiO_2 catalysts for H_2 generation through photoreforming of organics: introduction

A literature survey disclosed the increasing presence of papers in which hydrogen generation was attempted through photocatalytic reforming of organic species, by means of TiO_2-based catalysts modified with copper or used in the presence of copper salts.

The choice of copper is motivated by its cheapness and abundance in Earth's crust [36]. In particular, metal Cu, CuO, Cu_2O, $Cu(OH)_2$, and CuS, alone or in presence of a second co-catalyst have been proposed and tested to prepare copper-TiO_2 based photocatalysts [37]. It is reported that the doping of TiO_2 with copper species can effectively lower the band gap of TiO_2 by generating either structural defects into its framework, or active trap centers for electrons, due to heterojunction phenomena, thus limiting charge recombination [38-40].

Different techniques, such as hydrothermal/solvothermal processes, impregnation, precipitation, electrodeposition, and sol-gel method, have been so far adopted to include copper species on TiO_2 catalysts [37].

Therefore, a critical analysis of these papers was carried out by comparing mainly the different ways of preparation, the mechanisms proposed, the efficiencies recorded, the extension of TiO_2 light absorption capabilities, the sacrificial organics adopted and the pH of the test solutions, with the aim of collecting relevant references and stimulating the development of new ideas for the solution of problems which still limit the full exploitation on industrial scale of photocatalytic reforming for hydrogen generation.

2.2 TiO_2-Copper based photocatalytic systems and their preparation

Three groups of approaches for the combination of copper and TiO_2 have so far been used by researchers to develop photocatalytic systems for hydrogen generation:

A. Cupric ions dissolved in aqueous solutions in which TiO_2 is suspended;

B. Copper incorporated on the TiO_2 surface (as Cu^0 or Cu^{2+}, cupric or cuprous oxide, cupric hydroxide, $CuCr_2O_4$, $CuFe_2O_4$, CuS, $CuAlO_2$);

C. Copper incorporated on the TiO_2 surface in the presence of a second co-catalyst (nitrogen, graphene, carbon fibers, Al_2O_3, RuO_2, etc.).

In the case of Group A) approaches, there is no requirement of any particular preparation of the catalyst. Lanese et al. [41] reported that to generate hydrogen through a photocatalytic reforming process from a sacrificial organic species (i.e., formic acid), it is only necessary to suspend a commercial TiO_2 sample (i.e., pure anatase) in an acidic aqueous solution containing dissolved Cu^{2+} ions and chloride ions. Obviously, although the simplicity of assembling the system is an advantage, it is clear that the recovery of the reactants from the solution is not easy, due to the coexistence of different dissolved - Cu^{2+} - and suspended - TiO_2 and Cu^0 - chemical species present in the system.

Hydrogen can also be produced from UV irradiation of an aqueous solution in which both an organic sacrificial agent and cupric ions are present, suspending in it TiO_2 nanotubes [42]. The process is presented as a way of producing hydrogen through the simultaneous removal from water of both an organic species (which is oxidized) and cupric ions (which are reduced to Cu^0 and deposit on the TiO_2 surface). The main difference between the two works is represented by the fact that in the system reported by Lanese et al. [41] hydrogen forms when copper is substantially present as dissolved species, whereas Xu et al. [42] recorded a significant formation of hydrogen when Cu^0 is deposited on the TiO_2 surface.

In the case of Group B) approaches, to incorporate copper on the TiO_2 surface, one of the methods indicated in Table 2.1, lines 1-9, 11-13, 15-17, 20-24, 27, 29-30, 32-42, 44-48 is generally adopted.

It is interesting to observe that, according to the specific procedure for the preparation of the catalyst chosen, different active species can be incorporated on the TiO_2 surface. For example, for catalysts prepared through TiO_2 impregnation and calcination, a certain amount of TiO_2 is dispersed in an aqueous solution containing a copper salt, i.e. $Cu(NO_3)_2$, as reported in Table 2.1, lines 5, 10-11, 15-16, 29-30, 32-33, 37-38, 44. The water surplus is evaporated to dryness under slow heating and constant stirring. The samples are dried at 110 °C and calcined for some hours at different temperatures. It was indicated that the operating conditions of calcination (mainly the temperature) may influence both the oxidation state (+1 or +2) of copper [43] and its aggregation level [44,45]. Increase in the temperature beyond 300 °C results in reduction of the number of exposed Cu atoms and consequently the hydrogen generation rate [44,45].

In the case of electrodeposition, the electrolyte can be prepared, for example, by dissolving $CuSO_4$ in a lactic acid aqueous solution with pH adjustment to 11.0 with a NaOH solution [46]. The electrolyte is stirred and kept at a constant temperature of 25 °C. Different types of catalysts are obtained according to the deposition potential applied. The samples obtained are dried at 50 °C overnight in vacuum [46]. The characterization generally indicates that the lower the potential applied, the lower the size of Cu_2O particles deposited on TiO_2.

When photodeposition is adopted, a fixed amount of dried TiO_2 is suspended in aqueous solutions containing a dissolved copper salt [47]. A small amount of methanol is added as sacrificial agent and a medium pressure mercury lamp is used as light source. The irradiation is carried out for many hours under an inert atmosphere with continuous stirring of the mixture. At the end of the preparation, the solid is separated (by centrifugation) and washed with water to remove the residues of copper salt and methanol. After drying, it is calcined at different temperatures. With this method, Cu^0 particles were reported to form on the TiO_2 surface [47].

In the case of Group C) approaches, the preparation of the catalyst was performed as reported in Table 2.1, lines 18, 19, 25-26, 28, 31, 43. For example, if a copper species is incorporated along with carbon fibers [48], a certain amount of TiO_2 is added to a slurry containing dissolved copper nitrate and suspended carbon fibers. After ultrasonicating the final slurry for 4 hours, the water surplus is evaporated and the solid dried at 110 °C for 12 hours, and then calcined at 300 °C for 4 hours. The presence of CuO particles on the surface of the composite material obtained is demonstrated by XRD and Raman measurements.

To prepare a copper containing TiO_2-graphene composite, a hydrothermal method was proposed [49]. A certain amount of graphene oxide is dispersed by sonication in ethanol. After this treatment, both TiO_2 and CuO are added in a proper ratio to this suspension that is kept at 180 °C for 10 hours. The composite is recovered by filtration followed by rinsing with deionised water.

According to a mechanical mixing method also reported for the preparation of copper modified-TiO_2 catalyst in the presence of a second co-catalyst [50], the oxide powders of interest (i.e., CuO and Al_2O_3) are mixed with TiO_2 in a mortar before their sintering in a furnace under air atmosphere at 500 °C for about 3 hours.

An overview on the TiO_2 types used indicates that in 60% of cases commercial TiO_2 P25 was chosen as photocatalyst. In particular, P25 was preferred for catalysts preparation methods such as impregnation [43,51,52], complex precipitation [53-55], mechanical mixing [50], and hydrothermal methods [49,56,57]. In other cases, home-prepared titanium dioxide materials synthesized from appropriate precursors were used. Among other titanium precursors, titanium butoxide was used in electrospinning [58,59] and sol-gel [60] processes. In addition, titanium isopropoxide was largely employed in sol-gel methods [61-63], and in catalysts preparation techniques such as water-in-oil microemulsion method [64,65]. Pure anatase was adopted in a single case of TiO_2 suspended in a solution containing dissolved Cu^{2+} ions [41], and in experimental arrangements involving an impregnation method [66,67]. Finally, titanyl sulfate [62,65], titanium tetrachloride [68], and Ti foils [69] or plates [70] were also employed in further catalysts preparation procedures.

Table 2.1: Classification of Cu-TiO_2 catalysts used in photoreforming by sacrificial agent, preparation method and TiO_2 precursor selected, pH explored, Cu active species identified and overall quantum yield recorded.

	I **Sacrificial agent (s.a.)**		II **Reason for s.a. choice**	III **Catalyst preparation method (material)**	IV **TiO_2**	V **Cu active species**	VI **pH**	VII **Overall Quantum Yield**	VIII **Reference**
1	**Acetic Acid**		Selection of acetic acid as a model biomass-derived compound, since biomasses are regarded as promising renewable energy sources	1) Impregnation; 2) photodeposition; 3) mechanical alloying; (Cu added as $Cu(CO_2CH_3)_2 \cdot H_2O$, $Cu(NO_3)_2 \cdot 3H_2O$ and metallic copper, respectively)	Crude TiO_2 from the production line (sulfate technology)	Cu_2O and CuO	2.6	—	[47]
2	**Dyes**	**Acid Orange Ii**	Definition of a sustainable and economically viable strategy: azo dyes represent the most part of dye wastewaters readily available from industry	Electrospinning (Cu added as $Cu[CH_3(CH_2)_3CH(C_2H_5)CO_2]_2$)	$Ti(OBu)_4$	CuO	6.02	—	[58]
3		**Brilliant Red X-3b**	—	Centrifugation, drying and calcination of the suspension obtained by mixing TiO_2 and $CuSO_4$ solutions	$Ti(OBu)_4$	Cu_2O	—	—	[96]
4		**Methyl Orange (Mo)**	—	Synthesis by homogeneous hydrolysation followed by solvothermal crystallization and ethylene glycol-thermal reduction (Cu added as $Cu(CO_2CH_3)_2 \cdot H_2O$)	$Ti(OBu)_4$	Cu_2O	—	—	[94]
5		**Methylene Blue**	Treatment of seawater contaminated with dyes and sustainable H_2 production	Impregnation, drying and calcination (Cu added as $Cu(NO_3)_2 \cdot 3H_2O$)	P25	CuO	—	—	[88]

6	**Ethanol**	—	Mixture of $CuCl_2$ and mesoporous TiO_2 (synthesized by hydrolysis, sol-gel transition, hydrothermal treatment and calcination) within the water-ethanol solution	P25	Cu_n^0	—	—	[83]
7		—	Quick ion impregnation hydroxylation method (Cu added as $Cu(NO_3)_2 \cdot 3H_2O$)	P25 (80% anatase, 20% rutile)	Cu^{1+}	2÷12	—	[107]
8		Co-production of a valuable chemical (acetaldehyde) together with H_2 from waste organic streams	Synthesis of TiO_2 supports by: 1) sol-gel method; 2) precipitation; 3) water-in-oil microemulsion procedure (Cu added as $Cu(NO_3)_2 \cdot 3H_2O$ by photodeposition on TiO_2)	$Ti(OBu)_4$, $TiOSO_4$ and $Ti(\textit{i}\text{-}PrO)_4$, respectively	—	—	—	[65]
9		—	Precipitation method (Cu added as copper nitrate hemihydrate)	P25, (85% anatase, 15% rutile)	Cu^{2+} or CuO sub-monolayers	—	—	[55]
10		—	Wet impregnation and calcination process (Cu added as copper nitrate)	P25	CuO	—	—	[48]
11	**Ethanol and Glycerol**	Valorization of biomasses and sustainable H_2 production	1) Water-in-oil microemulsion method; 2) wet impregnation (Cu added as copper nitrate)	$Ti(O\text{-}i\text{-}Pr)_4$	Disperded Cu/CuO_x species and Cu ions into the titania lattice	—	—	[64]
12		Reuse of largely available second generation ethanol and sugars, extracted from vegetables, and glycerol, produced as a by-product of bio-diesel	Sol–gel method and precipitation, followed in both cases by calcination (Cu added as copper nitrate)	$Ti(O\text{-}i\text{-}Pr)_4$, $TiOSO_4$	—	—	—	[62]

13	**Ethylene Glycol**	—	Chemical bath deposition method (Cu added as $CuSO_4$)	Ti foils (99%)	$Cu(OH)_2$	—	—	[69]
14	**Formic Acid**	—	Aqueous solutions of TiO_2 and zero-valent copper or copper sulfate	Pure anatase	Cu^0 and Cu^{1+}	0÷2	2.47%	[41]
15	**Glycerol**	Production of biomass-derived glycerol in large amounts and its rapidly becoming waste with additional disposal costs	Impregnation method, drying and calcination (Cu added as $Cu(NO_3)_2$)	P25 (anatase-80%, rutile-20%)	Dispersed Cu^{1+}	—	—	[43]
16		Lower costs of organic wastes compared to fuels (such asMeOH) and simultaneous conversion of them into environmentally friendly products	Impregnation method, drying and calcination (Cu added as $Cu(NO_3)_2$)	P25	CuO clusters	—	13.4% (measures at 365 nm)	[51]
17		Production of biomass-derived glycerol in large amounts and its rapidly becoming waste with additional disposal costs	Electrodeposition method (Cu added as $CuSO_4$)	Ti foils (99%)	Cu_2O	7.4	—	[46]
18		Exceeding by-product of biodiesel production and of palm oil hydrolysis. Its photo-oxidation produces useful chemicals (dihydroxyacetone, glycolaldehyde, glyceraldehyde, formic acid and carbon dioxide)	Co-precipitation, drying and calcination (Cu added as $Cu(NO_3)_2 \cdot 3H_2O$)	P25	—	—	—	[35]

19	**Glycerol**	Sustainable organic waste from trans-esterification of vegetable oils to biodiesel	Sol-gel method (Cu added as copper nitrate)	Ti(O-i-Pr)$_4$	Cu^{1+} and Cu^0	—	—	[102]
20	**Glycol**	—	Deposition, drying and calcination (Cu added as $Cu(NO_3)_2 \cdot 3H_2O$)	P25	Cu_2O	—	—	[95]
21	**Methanol**	—	Incipient-wetness impregnation, calcination/reduction, and metallization process (Cu added as $CuCl_2 \cdot 2H_2O$). Synthesis of TiO_2 powder by sol–gel	$TiCl_4$	Oxidized Cu species	—	—	[68]
22		Reuse of industrial wastewater	Mixing $Cu(NO_3)_2$ and TiO_2 in aqueous solution, drying and calcinations	P25	CuO	—	—	[86]
23		—	Combined single-step sol–gel with surfactant-assisted templating mechanism (Cu added as $Cu(NO_3)_2 \cdot 3H_2O$)	Ti(O-i-Pr)$_4$	CuO	—	—	[61]
24		—	Impregnation method (mixture of TiO_2 and $CuNO_3$ in a MeOH solution, evaporation, drying and thermal treatment). Preparation of TiO_2 structure with a sol-gel method	Anatase	CuO	—	—	[66]
25		Best source for H_2 among high energy density liquid fuels; exothermic reactions with high reaction rates using POM	Deposition–precipitation method (addition of TiO_2 to the aqueous solution containing $Cu(NO_3)_2 \cdot 2.5H_2O$, drying and calcination)	P25	Cu_2O and CuO	—	—	[92]

26	**Methanol**	—	Synthesis of TiO_2-RuO_2 semiconductor by fusion; addition of copper phthalocyanine to the RuO_2-TiO_2 slurry containing MV^{2+}	Anatase	—	1÷11	—	[30]
27		—	Potentiostatic electrodeposition of Cu_2O (Cu added as $CuSO_4 \cdot 5H_2O$ within the electrolysis solution) on a TiO_2-coated ITO glass	P25	Cu_2O	—	—	[91]
28		—	Preparation of the binary support TiO_2–Fe_2O_3 by impregnation method. Preparation of Au–Cu/TiO_2–Fe_2O_3 catalysts by deposition-precipitation method (Cu added as $Cu(NO_3)_2 \cdot 2.5H_2O$). Drying and calcination of the mixture	P25	CuO	—	—	[53]
29		—	Impregnation method, drying and calcination (Cu added as $Cu(NO_3)_2$)	P25	CuO	4.8÷5.8	—	[93]
30		—	1) Complex precipitation; 2) impregnation methods (Cu added as $Cu(NO_3)_2 \cdot 3H_2O$)	P25	CuO	—	—	[54]
31		MeOH decomposition is a promising method for the practical and low-cost technologies in the H_2-based energy system	Mechanical mixing method, followed by the solid-state reaction at elevated temperature (Cu added as CuO nanopowder)	P25 (anatase 75%, rutile 25%)	CuO	—	—	[50]
32		—	1) In situ sol-gel (SG); 2) wet impregnation (WI) ; 3) chemical reduction of Cu salt (NR); 4) in situ photodeposition (PD) (Cu added as $Cu(NO_3)_2 \cdot 3H_2O$)	$Ti(OBu)_4$, P25	Cu_2O (NR); CuO (WI and SG); metallic Cu (PD)	0.5÷7	—	[60]

33	**Methanol**	—	1) Hydrothermal method via adsorption-calcination process; 2) wet impregnation process (Cu added as $Cu(NO_3)_2 \cdot 3H_2O$)	P25	CuO	—	—	[104]
34		—	Synthesis of mesoporous TiO_2 nanotube by hydrothermal-calcination process (Cu added as $Cu(NO_3)_2$)	P25	Cu^0	—	—	[42]
35		—	Hydrothermal-precipitation process (Cu added as $Cu(NO_3)_2$)	P25	$Cu(OH)_2$ and Cu^0	—	—	[56]
36		—	Sol-gel method (Cu added as $CuNO_3$)	$Ti(O\text{-}i\text{-}Pr)_4$	Cu_2O and CuO	—	—	[87]
37		—	Impregnation method, drying and calcination (Cu added as $Cu(NO_3)_2 \cdot 3H_2O$)	P25	Cu_2O	—	—	[45]
38		—	Impregnation method (Cu added as $Cu(NO_3)_2 \cdot 3H_2O$). Synthesis of TiO_2 nanotube by hydrothermal treatment	P25	CuO	—	—	[52]
39		—	Electrospinning and calcination (Cu added as $Cu(NO_3)_2 \cdot 3H_2O$)	$Ti(OBu)_4$	Cu_2O and CuO	5, 6	—	[59]
40		—	Pyrolisis of the homogeneous mixture of $Ti(SO_4)_2$ and $Cu(NO_3)_2$ (Cu added as $Cu(NO_3)_2$)	$Ti(SO_4)_2$	Cu_2O	—	—	[90]
41		—	Hydrothermal method at high temperature (Cu added as $Cu(NO_3)_2 \cdot 3H_2O$)	P25 (99.5%)	CuS	—	—	[57]

42	**Methanol**	—	Deposition by RF magnetron sputtering (Cu 99.99%pure)	Ti plates (99.9% pure)	Cu^{1+}	—	—	[70]
43		—	$CuO-TiO_2$ prepared by a simple impregnation method (Cu added as copper nitrate).Graphite oxide (GO) prepared by a modified Hummers' method. $CuO-TiO_2$-GR composite obtained via a hydrothermal method	P25	CuO	—	—	[49]
44	**Methanol and Sulfides**	—	Assembling $Cu@Cu_2O$ core-shell nanoparticles on TiO_2 nanotube arrays (NTAs) using an impregnation-reduction method (Cu added as $Cu(NO_3)_2\cdot 3H_2O$)	Anatase	Cu_2O and Cu^0	—	—	[67]
45	**Oxalic Acid**	—	Citric acid (CA)-assisted sol–gel method (Cu added as $Cu(NO_3)_2$)	P25	—	—	—	[97]
46	**Phenol**	—	Preparation of the TiO_2 system by a sol–gel method; dissolution of the of copper precursor, $Cu(NO_3)_2$, in the initial solution, drying and calcinations	$Ti(O-i-Pr)_4$	Cu^{1+}	—	—	[89]
47	**Sulfide and Thiosulfate**	Conversion into less harmful products (such as S_n^{2-} and $S_4O_6^{2-}$)	Directly mixing both catalysts,$CuAlO_2$ and TiO_2 (Cu added as CuO)	P25	—	5.5÷14	—	[82]
48	**Thiosulfate**	—	1) Solid state reaction; 2) co-precipitation; 3) sol-gel (Cu added as CuO and $Cu(NO_3)_2\cdot 3H_2O$)	$Ti(O-i-Pr)_4$	$CuFe_2O_4$	7, 13	1.30%	[63]
49	**DEA, TEA, TE, EDTA**	Comparison of H_2 evolution rate in the presence of various electron donors	Mixing $Cu(NO_3)_2$ and TiO_2 powder in aqueous solution, drying and calcination. Absorption of the dye onto the photocatalyst surface	P25	CuO	1÷14	5.10%	[98]

2.3 Efficiency of hydrogen generation

Although the amount of solar energy incoming daily on the earth's surface is huge and its capture virtually unlimited the problem of the efficiency is important in any case. In fact, considering that any method for hydrogen generation requires an investment of resources to be adopted on industrial scale (for example, the land surface used to absorb the radiation), it is clear that only those of them showing the highest efficiency values will be chosen for industrial applications.

There is more than one reason (Fig. 2.1) which makes the energy captured lower than that associated to the incident radiation [71]:

1) the energy of the irradiated photons may be lower than the bandgap, E_g, (in this case, no absorption happens) or higher than E_g (the absorption happens but the energy surplus is lost as heat);
2) only a fraction of the excited state energy is converted into chemical energy (the energy stored, for example, in a hydrogen molecule - e.g. its combustion energy - is generally a part of that necessary to transfer two electrons to the CB of the semiconductor used);
3) only a fraction of the absorbed photons is converted into photogenerated electrons (and holes) readily available for the reaction, due to the recombination reaction.

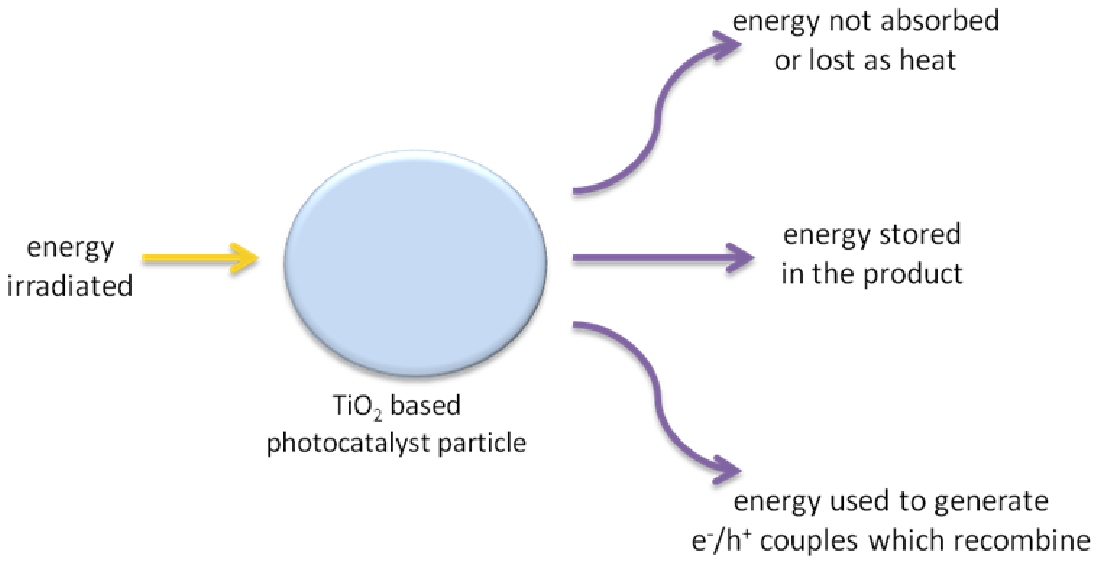

Figure 2.1: Fate of the energy irradiated on a TiO_2 photocatalytic particle.

Different indicators may be used to quantify the efficiency of the energy capture [29]. One of them is represented by the:

> Overall quantum yield ($\Phi_{overall}$). It is defined as the ratio between the rate of hydrogen generation r_{H_2} (mol/time), multiplied by 2, and the rate of photons incident on the catalyst particles (moles of photons/time):

$$\Phi_{overall} = \frac{2 \times r_{H_2}}{moles\ of\ incident\ photons/time} \times 100$$

Among the papers found to prepare this review, only few of them reported the data for the efficiency of generation (see Table 2.1).

As it is evident from Table 2.1, the few values indicated in the literature for the efficiency of generation were specified in terms of overall quantum yield and were in the range of 1.3-13.4%, well comparable with those found for the photocatalysts in which noble metals were incorporated on TiO_2. For example, Abe et al. [72] reported an overall quantum yield of about 2.0% for hydrogen generation on a photocatalyst based on Pt-TiO_2 sensitized by merocyanine, and Konta et al. [73] estimated a quantum yield for hydrogen evolution of 5.2% with a Rh-doped Sr-TiO_3 photocatalyst loaded with a Pt co-catalyst. Moreover, Astuti et al. [74] indicated a quantum yield in photogeneration of molecular hydrogen of 10±5%, employing a TiO_2 film catalyst sensitized with Zn-substituted cytochrome.

In all the other cases, the results were expressed in terms of simple rate or specific rate of hydrogen generation (normalized with respect to the mass of the engaged catalyst), which are absolutely not sufficient to carry out a comparison among the different data, since the values of the effective emission power were not written, whereas only the lamp type and the nominal powers were mostly specified in the experimental sections.

2.4 Sacrificial agents

As reported in Table 2.1, different organic species were adopted as sacrificial agents in photocatalytic reforming to generate hydrogen. This indication stresses the idea that this process is conducted under ambient conditions unselectively with respect to the photodegradable organic species. However, not all the organic compounds may ensure the same energy output in terms of hydrogen production. In the most part of the studies found, researchers used methanol, ethanol and glycerol as sacrificial agents (Table 2.1, lines 21-43, 6-10, 15-19, respectively). The reason for these choices may be represented by the fact that (1) these species ensure the highest yield of hydrogen, (2) their photocatalytic degradation has been extensively studied, and (3) they are derived from biomass production and therefore they may be considered as renewable sources for hydrogen. For example, the availability of glycerol, a side-product in the biodiesel production process, is nowadays so large that it may be considered as a waste material [43].

In recent years, the idea of using organic pollutants as sacrificial agents is becoming popular among researchers working in this field. The examples of adoption of formic and oxalic acids, reported in Table 2.1, go exactly in this direction, since often short-chain organic acids are the final refractory products of organic pollutants degradation by the most part of advanced oxidation processes [75-78].

Similar motivations were indicated for the choice as electron donors of dye molecules [79,80], of ethylene glycol [81], and of sulfide and thiosulfate [82]. In this way a combination of wastewater treatment with hydrogen generation could be possible. Some indications about the products of oxidation by positive holes of the sacrificial agent adopted were reported for the following compounds: ethanol, methanol, thiosulfate and glycerol.

<u>Ethanol</u>

Chen et al. [55], in an attempt to explain the results they obtained with a low cost CuO-TiO_2 catalyst, reported the following overall reaction of ethyl alcohol with positive holes:

$$2h^+ + CH_3CH_2OH \rightarrow CH_3CHO + 2H^+ \qquad r_{2.1}$$

On the other hand, Korzhak et al. [83], who carried out the experimental investigation on mesoporous Cu_n^0-TiO_2 nanocomposite catalyst, tried to depict a more detailed mechanism, indicating the single steps through which the alcohol may give rise to acetaldehyde:

$$h^+ + CH_3CH_2OH \rightarrow CH_3CH_2^{\bullet +}OH \rightarrow CH_3CH^{\bullet}OH + H^+ \qquad r_{2.2}$$

$$CH_3CH^{\bullet}OH + TiO_2(h^+/e^-) \rightarrow TiO_2(e^-) + CH_3CHO + H^+ \qquad r_{2.3}$$

Although not expressly indicated, the radical species formed in reaction $r_{2.2}$ still reacts with a positive hole also in reaction $r_{2.3}$ to generate acetaldehyde, leaving a photogenerated electron potentially available for further reactions. Anyway, also in this case, no indications are reported about further oxidation of the aldehyde.

Methanol:

Also for this species, some authors [56] reported an overall oxidation reaction of the system based on the use of TiO_2 nanotubes (TNTs):

$$\mathrm{TNTs} \xrightarrow{\text{UV irradiation}} \mathrm{TNTs}\ (h^+ + e^-) \qquad r_{2.4}$$

$$\mathrm{TNTs}\ (h^+) + CH_3OH + H_2O \rightarrow 6H^+ + CO_2 \qquad r_{2.5}$$

On the other hand, Choi et al. [66] tried to go further into the details of the process:

$$CH_3OH \xrightarrow{hv} :CH_2 + H_2O \xrightarrow{{}^{\bullet}OH} {}^{\bullet}CH_2OH \xrightarrow{{}^{\bullet}OH} CH_2(OH)_2 \qquad r_{2.6}$$

considering the intervention of OH radicals formed from H_2O/OH^- reaction with positive holes.

However, it is interesting to observe that the formation of $CH_2(OH)_2$ may also be explained through other more probable pathways, which consider that the radical species ${}^{\bullet}CH_2OH$ is still able to react with a positive hole, producing a proton and formaldehyde with the latter capable of generating hydrated compounds by the addition of water.

$$CH_2(OH)_2 \xrightarrow{\text{major decarboxylation}} CO_2 + 2H_2 \qquad r_{2.7}$$

$$CH_2(OH)_2 \rightleftarrows CH_2 = O + H_2O \xrightarrow{\text{decarbonylation}} CO_2 + 2H_2 \qquad r_{2.8}$$

Even for reactions $r_{2.7}$ and $r_{2.8}$, possible alternative pathways may be found. For example, it can be considered that the species $CH_2(OH)_2$ may still react with a positive hole to form acetic acid, instead of carbon dioxide and hydrogen. On the other hand, no evidence is provided by the authors on the decarboxylation and decarbonylation they tried to support.

Miwa et al. [50] proposed a mechanism for the organic oxidation, which only partially agrees with that reported by Choi et al. [66]:

$$\mathrm{CH_3OH + h^+ \rightarrow {}^{\bullet}CH_2OH + H^+} \qquad r_{2.9}$$

$$\mathrm{{}^{\bullet}CH_2OH + h^+ \rightarrow CH_2 = O + H^+} \qquad r_{2.10}$$

$$\mathrm{CH_2 = O + h^+ + {}^{\bullet}OH \rightarrow H^+ + HCOOH} \qquad r_{2.11}$$

$$\mathrm{HCOOH \rightarrow HCOO^- + H^+} \qquad r_{2.12}$$

$$\mathrm{HCOO^- + 2h^+ \rightarrow H^+ + CO_2} \qquad r_{2.13}$$

Even for reaction $r_{2.11}$ it is possible to propose an alternative one in which the hydrated form of formaldehyde reacts with the positive holes producing formic acid.

$$\mathrm{CH_2 = O \xrightarrow{+H_2O} CH_2(OH)_2 \xrightarrow{h^+} {}^{\bullet}CH(OH)_2 \xrightarrow{h^+} HCOOH} \qquad r_{2.14}$$

Thiosulfate:

Kezzim et al. [63], in a paper reporting on hydrogen generation over a $CuFe_2O_4$-TiO_2 based hetero-system, gave the following overall reaction for its oxidation by the holes and formation of sulfite ions:

$$\mathrm{S_2O_3{}^{2-} + 4h^+ + 6OH^- \rightarrow 2SO_3{}^{2-} + 3H_2O} \qquad r_{2.15}$$

In this way, it is possible to associate hydrogen generation with the removal of a species - thiosulfate - that is often present in industrial wastewaters from sources such as petroleum refineries, photo-processing, mining, paper industry and coal processing, and that can cause serious ecological issues [84].

Glycerol:

Lalitha et al. [43] reported the possibility that glycerol could be oxidized through reactions with hydroxyl radicals, generated by the oxidation of water molecules with positive holes, although no indications are given on the actual presence in the reacting solution of the intermediates included in the reaction scheme they proposed.

In a study on hydrogen generation with a Cu-TiO_2 catalyst and glycerol as sacrificial agent, Montini et al. [62] found in liquid phase 1,3-dihydroxypropanone and hydroxyacetaldehyde with minor occurrence of 2,3-dihydroxypropanal, 1,2-ethandiol, hydroxyacetone and two isomers of dimethyl-1,4-dioxane. For some of the intermediates detected, a possible formation pathway could be reasonably hypothesized as shown in Figure 2.2:

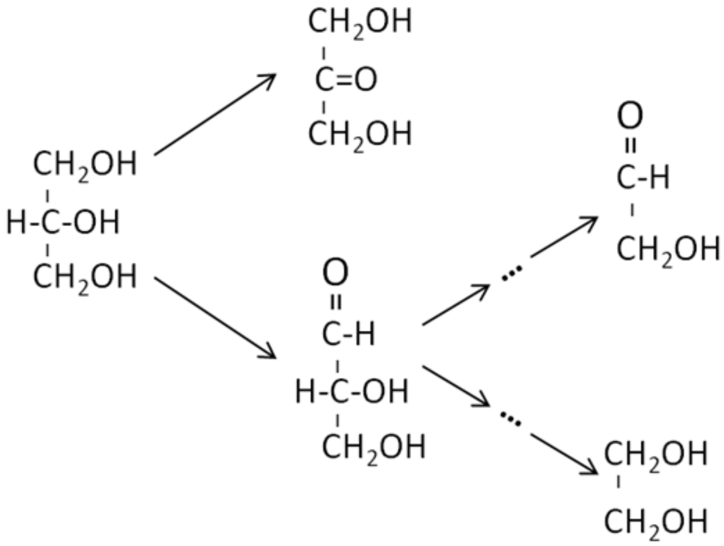

Figure 2.2: Possible reaction pathways for intermediates production from glycerol.

whereas for some other compounds, such as hydroxyacetone and two isomers of dimethyl-1,4-dioxane, the formation pathways appear less defined.

Kait et al. [35] identified glyceraldehyde, glycolic acid, and oxalic acid as intermediates of glycerol photooxidation under visible light illumination as shown in Figure 2.3.

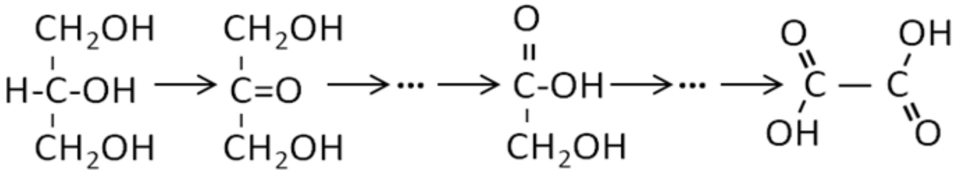

Figure 2.3: Schematic reaction mechanism of glycerol photooxidation under visible light.

Moreover, if more structurally complex sacrificial agents were adopted (i.e. dyes), no indications were reported about the presence of oxidation products which require further treatments before the final discharge of the solution. This fact limits the possibility to correctly evaluate the generation costs, since the availability of other treatment plants could be necessary in addition to the photocatalytic reactor when wastewaters are used to feed the system.

2.5 Enhancement of TiO_2 light absorption capability

Among the drawbacks of using TiO_2 as a photocatalyst for solar hydrogen generation, its activation by UV radiation with wavelength lower than 400 nm is surely one of the most relevant. In fact, UV accounts only for 5.0% of the solar radiation energy [20]. A modification of pure TiO_2 by incorporating other species is thus necessary to extend the range of absorption to visible light region. Pelaez et al. [85] published a comprehensive review on the development of visible light active TiO_2 photocatalysts and their environmental applications. Various strategies have been adopted to extend TiO_2 photoactivity to visible light domain and to enhance TiO_2 photocatalytic properties, and thus improve TiO_2 photocatalytic properties under solar light irradiation. In particular, non-metal and/or metal doping, dye sensitization, and coupled semiconductors exhibiting visible light-induced photoactivity have been presented and discussed, including their synthesis, properties, mechanism of activation, and applications [85].

From other studies, it resulted that a red shift is often observed when copper-incorporated TiO_2 catalysts are prepared. This is true for different species identified on the semiconductor such as CuO [48,51,55,58,59,86-88], Cu_2O [46,48,54,61,66,87,89-96], Cu^0 [41,42,69], $CuCr_2O_4$ [97], and $CuFe_2O_4$ [63]. However, it is important to stress that the photocatalysts' capability to absorb in the visible light spectrum is important only if, once irradiated, the solids are able to use the energy absorbed to generate electrons and holes. In other words, only if the visible energy absorbed by the catalysts is directly responsible for the formation of charge carriers, a beneficial effect may be expected from the enhanced absorption capability.

For example, a Cu_2O-TiO_2 nanotube array (TNA)-based catalytic system was irradiated by means of a Xe lamp, in which the UV range emission was removed by a UV-400 filter [46]. A significant increase in the specific rate of hydrogen generation was recorded on this catalyst with respect to the pure TNA. The results of these experiments demonstrates that the incorporation of copper as Cu_2O on TiO_2 allows the exploitation of visible light irradiation for the generation of electron-hole couples, which was not possible with bare TiO_2. On the other hand, a quite different situation was found for the CuO-TiO_2 hybrid catalyst. In a study on an Eosin sensitized CuO-TiO_2 catalyst for hydrogen generation in the presence of organic electron donors (e.g., triethanolammine, acetonitrile) under visible light radiation (>400 nm), Jin et al. [98] found that no hydrogen was produced in the absence of the sensitizer, thus confirming that, although the CuO-TiO_2 system is capable to absorb visible light radiation, the generation of electrons in the CB of CuO is not useful to make the system reactive without a transfer from the CB of TiO_2 (which is not photoactivated in the absence of the dye under visible light irradiation).

When $CuCr_2O_4$ was incorporated on TiO_2 [97], an intense absorption in the visible light range was recorded and a significant increase of the photoactivity was observed with respect to either TiO_2 or $CuCr_2O_4$ single catalysts, similarly to the case of the Cu_2O-based system. However, these results were collected in experimental runs in which a Xe lamp was used without the adoption of cutting filters to remove the UV component. That is, the irradiation adopted in the experiments was in both UV and visible light ranges and the increase of the reactivity after the incorporation on TiO_2 of copper could not unambiguously be attributed to the extension of the absorption range.

Kait et al. [35] tested the activity of a TiO_2 supported Cu-Ni photocatalyst under visible light illumination: in comparison with bare TiO_2, they found a narrower band gap for Cu-Ni-TiO_2 with consequent enhancement in visible light absorption and noticeable increase in hydrogen generation.

Indeed, it is well known that, to extend TiO_2 photocatalytic activity to visible region, its band gap needs to be narrowed [99]. Another good strategy to fulfill this purpose could be that of using anionic dopant species, i.e. nitrogen, as substitutes for lattice oxygen [100,101]. Taylor et al. [102] developed a novel binary N-Cu-TiO_2 photocatalyst for hydrogen production upon photoreforming of glycerol, under near-UV and visible light. Compared to P25 TiO_2, N-Cu-TiO_2 exhibits stronger light absorption in near-UV and visible ranges, and up to 44-times higher rates of hydrogen production.

2.6 Mechanisms of reaction

For the papers belonging to the Group A) approaches (cupric ions dissolved in aqueous solutions in which TiO_2 is suspended), the starting point to find a suitable mechanism able to explain the experimental findings is represented by the indications reported in the literature on the capability of cupric ions to be reduced to Cu^0 in the presence of TiO_2, UV irradiation and an organic species [103]. However, for the two papers quoted [41,42], the steps of generation of hydrogen are quite different. According to the first paper [41], the proton reduction is made possible by the capability of cuprous chloride complexes to release an electron in the solution upon UV irradiation:

$$\mathrm{CuCl + Cl^- \rightleftarrows CuCl_2{}^-} \qquad r_{2.16}$$

$$\mathrm{CuCl + 2Cl^- \rightleftarrows CuCl_3{}^{2-}} \qquad r_{2.17}$$

$$\mathrm{CuCl_2{}^- \overset{h\nu}{\rightarrow} Cu^{2+} + 2Cl^- + e^-} \qquad r_{2.18}$$

$$\mathrm{CuCl_3{}^{2-} \overset{h\nu}{\rightarrow} Cu^{2+} + 3Cl^- + e^-} \qquad r_{2.19}$$

Therefore, it can be hypothesized that when cupric ions are reduced to Cu^{1+} in the photocatalytic process, the latter immediately forms complexes with chlorides, which undergo a photolytic oxidation with electrons generation. If a further partial reduction of Cu^{1+} species to Cu^0 occurs, the formation of hydrogen can be explained through the photoxidation - catalyzed by chlorides- of zerovalent copper:

$$\mathrm{Cl^-_{ads} + H^+_{aq} \xrightarrow{h\nu, Cu^0} Cl^\bullet_{ads} + H^\bullet{}_{aq,ads}} \qquad r_{2.20}$$

$$\mathrm{Cl^\bullet_{ads} + Cu^0 \rightarrow CuCl_{aq,ads}} \qquad r_{2.21}$$

The rate of hydrogen generation is strongly reduced by an increase of pH in the solution for values higher than 2.0, for which probably proton reduction by the photogenerated electron becomes the rate determining step.

In the second paper belonging to the Group A) approaches [42], it was claimed that Cu^{2+} in solution is reduced to Cu^0 through reaction with the photogenerated electrons in the CB and settles on the TiO_2 surface. In other words, this system could be considered as the result of the deposition of metallic copper on TiO_2, *in situ*. As illustrated in Figure 2.4, once deposited, metallic copper functions as active site for H_2 formation, being the electrons in CB of TiO_2 prone to move to the Cu spots due to the lower Fermi level of metallic copper (Fig. 2.4). Obviously, since the reduction of Cu^{2+} competes with hydrogen formation, at the beginning of the run, when the cupric ions concentration is high, the rate of H_2 formation appears low.

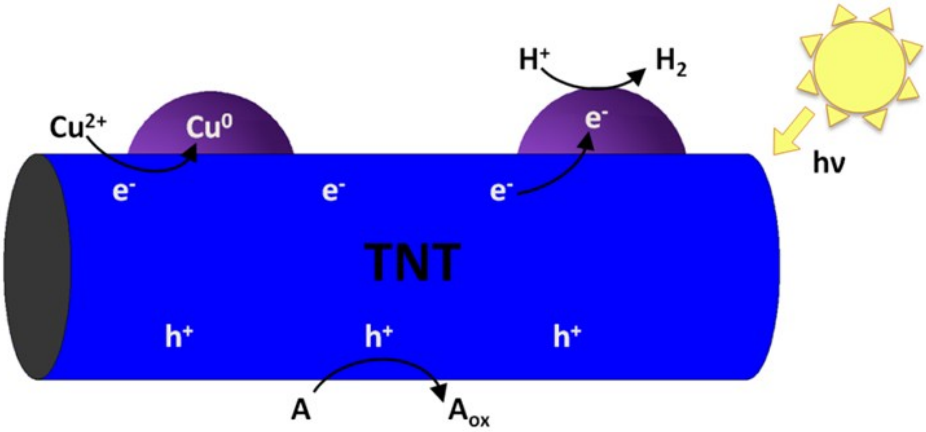

Figure 2.4: Illustration of the main photocatalytic reactions occurring on TiO_2 nanotube (TNT) surface under illumination: reduction of Cu^{2+} and H^+ by photogenerated electrons and oxidation of organics (A) by positive holes.

The incorporation of copper on TiO_2 may result in different chemical forms present on the semiconductor, according to the preparation procedure. The results of the characterization works reported in the papers analyzed evidenced the presence on TiO_2 of the following main forms: metal copper, CuO, $Cu(OH)_2$, Cu_2O, $CuCr_2O_4$, $CuFe_2O_4$, CuS, $CuAlO_2$ and CuO-Al_2O_3.

Metal copper

The copper photodeposition may be achieved also before the experiments, as Montini et al. [62] performed, allowing zero-valent copper to deposit on TiO_2, under UV irradiation. Surprisingly, during the runs, a small amount of zero-valent copper may be oxidized and leached into the solution. However, the degree of leaching is strongly dependent upon the type of irradiation used during the experiments. When the UV component is present in the radiation coming from the lamp, a very limited leaching is observed, due to a continuous photo-deposition of copper itself.

This enhancement in photoefficieny for hydrogen generation has been ascribed, in the case of Cu^0 and other metals (i.e., Pt, and Pd), to a reduced recombination process between photogenerated holes and electrons due to the formation of Schottky barriers at the metal/TiO_2 interface [180] (Figure 2.5). In other words, as the work function of the selected noble metal (ϕ_m) is higher than that of the titanium dioxide (ϕ_s), electrons flow from TiO_2 to the metal in order to align the Fermi energy levels (E_F), with a shift of the Fermi levels of the metal to the conduction band of titanium dioxide [181]. At the end of the process, the metal has more negative energy levels favoring the proton ion reduction from a thermodynamic point of view, and excess negative charges favoring the proton reduction from a kinetic point of view, whereas excess positive charge and a Schottky-type potential barrier are formed in the semiconductor.

Moreover, the potential energy barrier (V_D), formed at the noble metal-TiO$_2$ junction (heterojunction) acts as an effective electron trap preventing the recombination of electron/hole pairs. The decrease in charge carriers recombination results in enhanced photo-activity of the material towards hydrogen production.

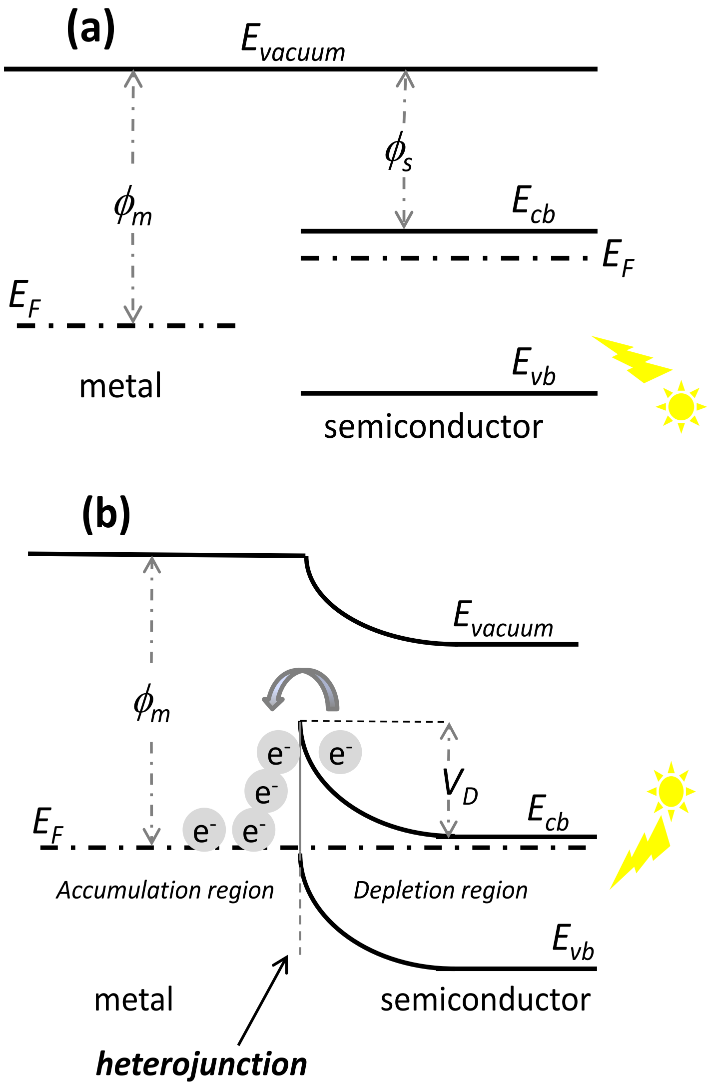

Figure 2.5: Scheme of Schottky junction between metal and semiconductor with energy level alignment. (a): before the heterojunction; (b): after the heterojunction.

In some cases, the deposition of metal nanoparticles (such as Ag and Au) on TiO_2 also enhances the visible light photo-catalytic activity of titania particles through the "Local Surface Plasmonic Resonance" (*LSPR*) [182]. The *LSPR* generally occurs if the oscillation frequency of the electromagnetic-field is in phase with free electrons of the metal [183]. The frequency of free electrons oscillation in a metal nanoparticle with minimal power dissipation is known as "plasmon resonance frequency". Under this condition, the conduction negative charges of the noble metal nanoparticles collectively oscillate generating electron plasma (called plasmons). This results in an enhancement of photocatalytic activity as metal nanoparticles can (*i*) act as antennas favoring a higher light absorption and (*ii*) sensitize the semiconductor by promoting the transfer of free excited electrons into the conduction band of the semiconductor through the so-called "Process of Plasmon Induced Resonance Energy Transfer" (*PIRET*) (Figure 2.6) [184].

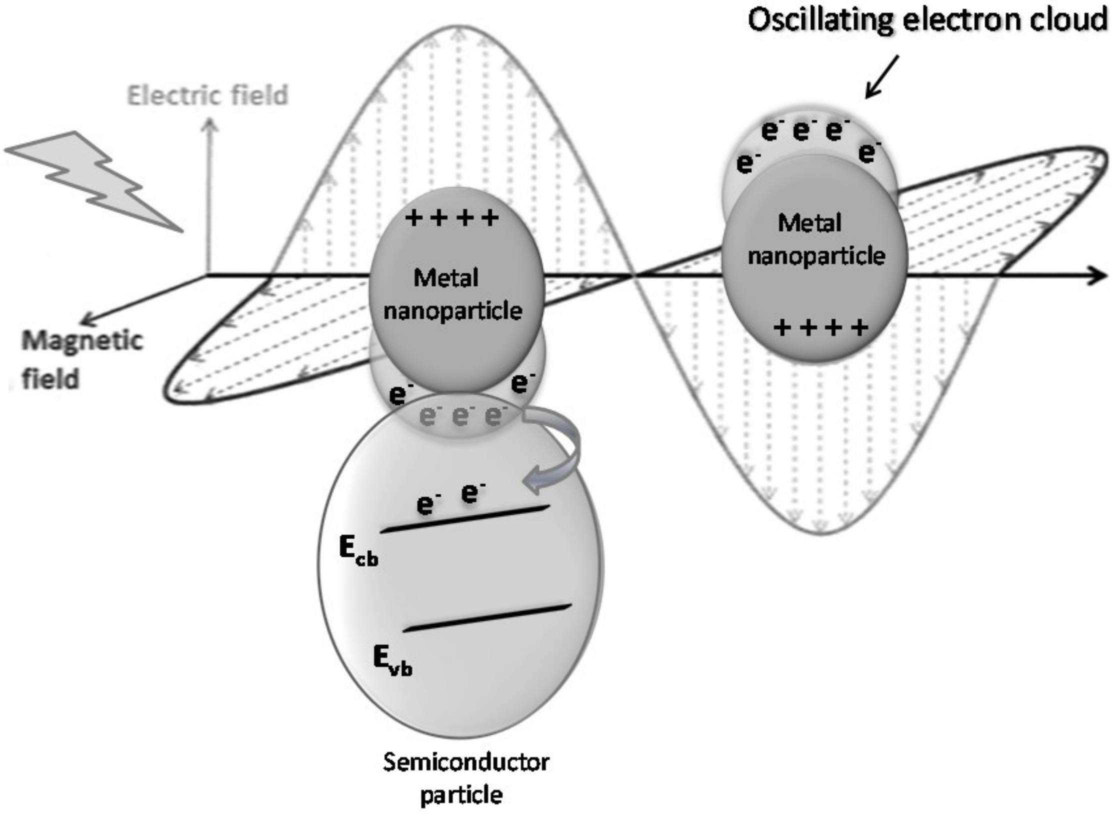

Figure 2.6: Dipole polarizability of metal nanoparticles under electric/magnetic fields and electron migration to the conduction band of the semiconductor.

CuO and Cu_2O

The presence of cupric and cuprous oxide on TiO_2 was observed by many researchers, both at nano or micro scales. The combination of two inorganic semiconductors is of particular interest to extend the absorption spectrum range and improve the photoactivity of the catalyst. For these purposes, it is required to couple TiO_2 (n-type semiconductor) with a p-type semiconductor.

The photocatalytic system involving two or more different semiconductors (n and p types) in presence of a selected shuttle redox mediator is known as "Z-scheme". Redox mediators are selected inorganic ions, such as, S^{2-}/SO_3^{2-} [185], IO_3^-/I^- [186] and Ce^{4+}/Ce^{3+} [187] used to increase the lifetime of photo-generated charges, and in some case to prevent the photocorrosion of metal sulfides used as n- or p- type semiconductors.

Chen et al. [55] reported that, depending on the copper load on TiO_2, CuO is found to be a sub-layer, for low Cu loads, and in the form of nanosized particles and then bulk when more than 3.0% of Cu is present on the semiconductor. These authors recorded a huge enhancement of reactivity passing from bare TiO_2 to CuO-TiO_2. In particular, they observed an increase of reactivity when increasing the Cu load up to 1.25%. Beyond this value, the reactivity reduces sharply, becoming 20% of the maximum observed for a Cu content equal to 15%. This behavior was explained considering the following: (1) the presence of CuO as co-catalyst makes possible an electron transfer from the CB of TiO_2 to that of CuO, which reduces the occurrence of the electron-hole recombination reaction; (2) in the literature, a quantum size effect was reported according to which the band gap of CuO decreases with increasing the particle size with the potential of both bands changing accordingly, as shown in Figure 2.7. From this figure, it is evident that when bulk CuO particles are present on TiO_2, the hydrogen formation is depressed since the electron transfer from the CB of bulk CuO to the couple H^+/H_2 is hindered by the difference of potential existing. Similar explanations were reported also by others [51].

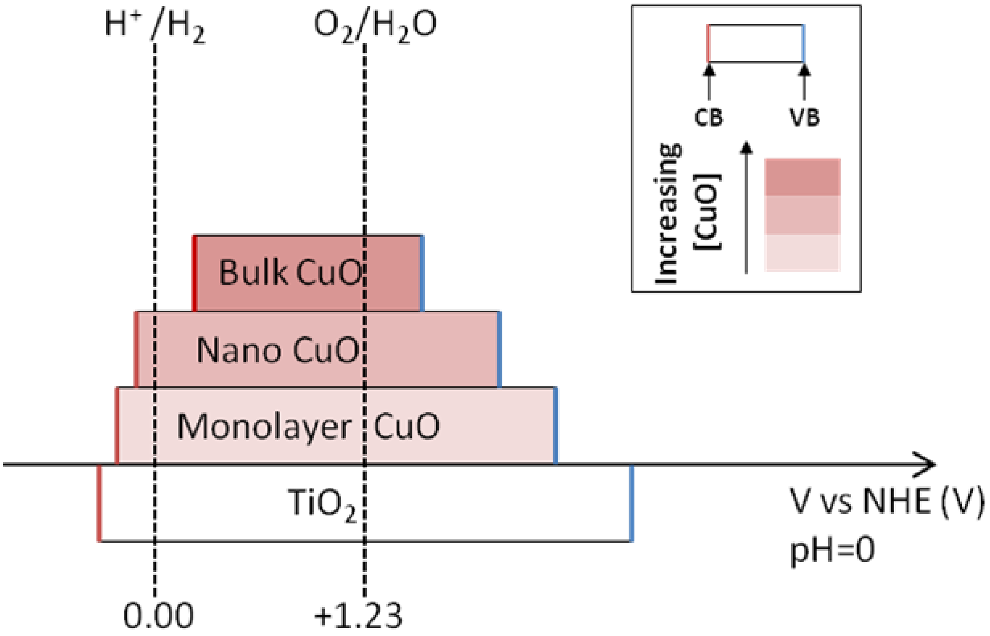

Figure 2.7: Comparison between band gaps of TiO_2 and CuO at different concentrations/particles size.

In a second group of papers dealing with the presence of CuO on TiO_2, a different view was proposed to explain how the system works [58,86,104]. Also in this case, it was considered that the CB potential of CuO is more positive than that of TiO_2, irrespective of the particle size, thus enabling an electron transfer from the latter to CuO. However, since the CB of isolated bulk CuO has a potential which does not allow to transfer an electron to the H^+/H_2 couple, researchers stated that, during the passage of electrons from TiO_2 to CuO, the Fermi level of the latter is raised, resulting into a more negative CB potential of CuO able to promote water (or H^+) reduction. The negative shift of CB potential of CuO was also confirmed by potential measurements.

Jeon et al. [87] investigated hydrogen production over Cu-TiO_2 photocatalysts containing Cu_xO species. As shown in XRD and XPS results, depending on the crystalline structure (anatase and rutile) obtained after different thermal treatments (500°C and 800°C), Cu_2O and CuO components dominate, respectively. The analysis showed that the Ti $2p_{3/2}$ bands in Cu-TiO_2 photocatalysts are shifted to binding energies lower than that of bare TiO_2, revealing the lower oxidation state (Ti^{3+}) of Ti; the shift is larger in the rutile structure, in which CuO species are predominant. The hydrogen generation from photoreforming of methanol is also greater over the rutile form than over the anatase one. The Cu-TiO_2 particles absorb radiation with wavelength from 200 to 800 nm, differently from bare TiO_2, which absorbs only below 380 nm.

Lalitha et al. [43] proposed a different mechanism in which Cu^{2+} is reduced to Cu^{1+} during the reaction, as confirmed by XPS measurements on the catalyst used. This view allows to explain why, using glycerol as sacrificial agent, the rate of hydrogen generation for the CuO-TiO_2 composite catalyst:

i) is 50% lower than that observed for a similar TiO_2 catalyst with the same content of copper but present as Cu_2O at the beginning of the process;
ii) increases during the photocatalytic run.

The presence of a second co-catalyst along with CuO on TiO_2 was reported by Wang et al. [49], who prepared a system containing also graphene. As shown in Figure 2.8, once introduced on the semiconductor, graphene not only accepts the photogenerated electrons coming from the CB of TiO_2 (as CuO does), but can also transfer them to H^+ and, due to its excellent electrical conductivity, can act as a conductive electron transport “highway”. The addition of graphene further improves the photocatalytic performances of CuO-TiO_2 system. The presence of two co-catalysts makes possible to obtain a specific hydrogen generation rate 20 times greater than that of pure TiO_2.

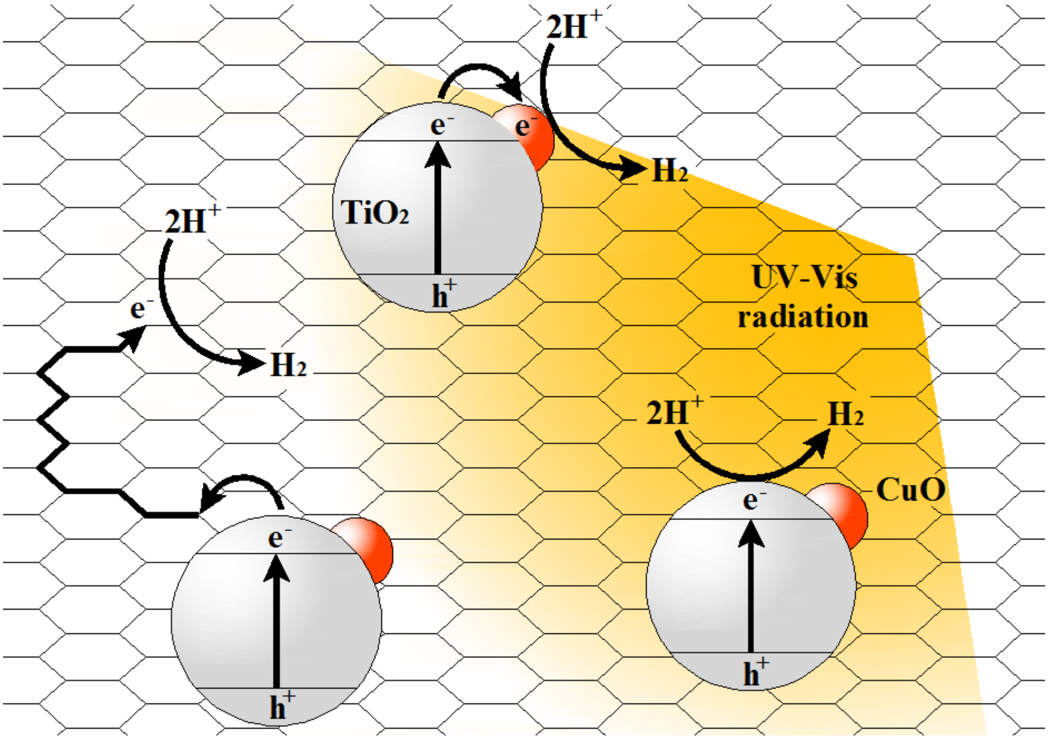

Figure 2.8: Illustration of the reaction mechanism of the CuO-TiO_2-GR composite catalyst under UV-Vis light irradiation [37].

Another example of use of a second co-catalyst along with CuO on TiO_2 is represented by a catalyst containing also carbon fibers (CF). The solid CuO-CF-TiO_2 (P25) shows a hydrogen generation rate which is 45 times that of TiO_2 (P25), and two times that of CuO-TiO_2 [48]. It can be assumed that the electrons in the CB of TiO_2 are transferred to that of CuO by two different ways. In fact, as a direct transfer route between the two CBs is operative due to the potentials difference, a second and indirect one, consisting in a first jump of the electrons to CF and a subsequent transport to CuO, is also active. According to this view, CF functions as electron acceptor and transporter, which enables lengthening of the lifetime of the photogenerated electrons.

Again, another example of co-catalyst that can be coupled with CuO-TiO_2 system is represented by a dye. Jin et al. [98] used eosin for this purpose and restricted the experiments to the use of visible light radiation (λ>400 nm). In the absence of the dye, no production of hydrogen was observed. This indicates that the semiconductor diode is not able to exploit the radiation used during the runs, whereas the dye does. The authors stated that, under visible light absorption, the dye transfers electrons to the CBs of TiO_2 and CuO (and again some photogenerated electrons move from TiO_2 to CuO). In agreement with what reported by others [86], during this transfer of electrons a shift of Fermi level and CB of CuO occurs, promoting thus a final reduction of protons (or water molecules).

Cu_2O is one of the few p-type semiconductors which are inexpensive, non-toxic, and readily available. Its low band gap (2.0 eV) permits the photocatalytic activity under visible light irradiation of the system prepared through the deposition of copper on TiO_2 nanotube arrays (TNA) [46]. Since the CB of Cu_2O is more negative than that of TiO_2, the excited electrons can be quickly transferred from Cu_2O nanoparticles to TNA, leaving the holes on the VB of Cu_2O and leading to an effective reduction of protons to H_2, as illustrated in Figure 2.9.

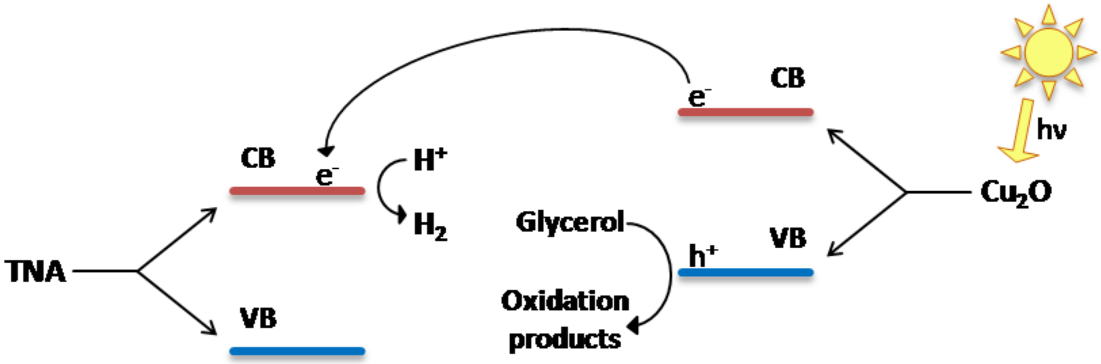

Figure 2.9: Mechanism of protons reduction in the Cu_2O-TNA system.

The photoactivity of a nanodiode with behavior intermediate between that of between that of p- and n-type semiconductors can be greatly enhanced if an Ohmic junction is formed, as in the case of Cu-Cu_2O core-shell nanoparticles assembled on TiO_2 nanotubes arrays [95]. Following the absorption of visible light by Cu_2O nanoparticle shell, the photogenerated electrons can be more efficiently transferred to TiO_2 through a copper layer. The role of the latter is (1) to ensure a low resistance to electron transfer, (2) to serve as an electron storage center which helps separate the charges on the catalyst, and (3) to contribute, by means of its plasmonic-excited core, to the photocatalytic properties of TNAs under visible light irradiation.

Cu(OH)$_2$

Dang et al. [56] found that during the fabrication of the catalyst, through a hydrothermal-precipitation process, the surface of TiO$_2$ nanotubes (TNTs) is covered by nano-Cu(OH)$_2$. The CB potential of Cu(OH)$_2$ is -0.222 V, more positive than that of the semiconductor (-0.260 V), for which a transfer of photoinduced electrons is permitted from the latter to the former. The excess of electrons gathered on Cu(OH)$_2$ causes the reduction of Cu(OH)$_2$ to metallic Cu. Both Cu(OH)$_2$ and metallic Cu favor the separation of photoinduced electron-hole pairs, thus enhancing the photocatalytic activity for hydrogen evolution. It is clear that the holes in the VBs of nanotubes are primarily scavenged by methanol. The following scheme may help to summarize all the reactions involved:

$$\mathrm{TNTs} \overset{h\nu}{\rightarrow} \mathrm{TNTs}(e^- + h^+) \qquad r_{2.22}$$

$$\mathrm{TNTs}(e^-) + \mathrm{Cu(OH)_2} \xrightarrow{\text{Electron transfer}} \mathrm{TNTs} + \mathrm{Cu(OH)_2}(e^-) \qquad r_{2.23}$$

$$\mathrm{(CuOH)_2} + 2e^- \rightarrow \mathrm{Cu} + 2\mathrm{OH}^- \qquad r_{2.24}$$

$$\mathrm{TNTs}(e^-) + \mathrm{Cu} \xrightarrow{\text{Electron transfer}} \mathrm{TNTs} + \mathrm{Cu}(e^-) \qquad r_{2.25}$$

$$\mathrm{(CuOH)_2}(2e^-) + 2\mathrm{H}^+ \rightarrow \mathrm{H_2} + \mathrm{(CuOH)_2} \qquad r_{2.26}$$

$$\mathrm{Cu}(2e^-) + 2\mathrm{H}^+ \rightarrow \mathrm{H_2} + \mathrm{Cu} \qquad r_{2.27}$$

$$\mathrm{TNTs}(6h^+) + \mathrm{CH_3OH} + \mathrm{H_2O} \rightarrow \mathrm{TNTs} + \mathrm{CO_2} + 6\mathrm{H}^+ \qquad r_{2.28}$$

A similar view was also proposed by Zhang et al. [69].

CuCr$_2$O$_4$ and CuFe$_2$O$_4$

Another example of diode with behavior intermediate between that of p- and n-type semiconductors is represented by the system CuCr$_2$O$_4$-TiO$_2$ [97]. The solid CuCr$_2$O$_4$ was reported to be able to absorb visible light irradiation due to its small band gap [105]. Under solar simulated radiation, mainly CuCr$_2$O$_4$ is activated generating the charge carriers. The photogenerated electrons are injected into the CB of TiO$_2$, where they can reduce water, whereas the holes react with oxalic acid (the sacrificial agent). A migration of the holes generated on CuCr$_2$O$_4$ into the VB of TiO$_2$ was also indicated by researchers, although no evidence of this transfer was revealed in the work. The mechanism proposed for $CuFe_2O_4$ is very similar to that reported for $CuCr_2O_4$ [63].

CuS

The photoactivity of CuS-TiO_2 system is 32 times greater than that of pure P25 TiO_2 and this was attributed by researchers [57] to the capability of CuS particles dispersed on the TiO_2 surface to prevent the recombination between photogenerated electrons and holes. The former are transferred from CB of TiO_2 to CuS particles and promptly reduce protons to hydrogen molecules.

$CuAlO_2$

A moderate activity of this species in hydrogen generation when using hole scavengers, such as sulfide and thiosulfate, was documented by Koriche et al. [106].

Brahimi et al. [82] reported on the results obtained when this semiconductor was used along with TiO_2. No incorporation of the copper salt on the surface of TiO_2 was carried out and the two solids were only suspended in the same solution. All the work done to characterize $CuAlO_2$ prepared by Brahimi et al. [82] indicates a narrow band gap (1.29 eV) of this solid, which surely enables the absorption of visible light irradiation. The results of their experiments show that, in the presence of TiO_2, there is a huge increase of photoactivity, which is six-fold greater than that measured on bare $CuAlO_2$. A mechanism similar to that proposed for Cu_2O-TiO_2 is also reported, in which the electrons move from the CB of p-type semiconductor to that of TiO_2, where they are used to reduce water molecules. The positive holes on $CuAlO_2$ solid react with sulfide ions. In other words, the presence of TiO_2 and the availability of its CB seem to have a great effect on the charge separation.

CuO-Al_2O_3-TiO_2

Miwa et al. [50] tested the capability of a CuO-Al_2O_3-TiO_2 nanocomposite material to generate hydrogen in the presence of methanol dissolved in water. The performance of the catalyst was better than those of the binary systems CuO-TiO_2 and Al_2O_3-TiO_2. According to the Miwa et al. [50], the role of the two oxides, CuO and Al_2O_3, is that of favoring an enhancement of the charge separation and thus increase in the efficiency of the system.

2.7 pH effect

Since proton reduction by the photogenerated electron is the fundamental reaction through which a hydrogen molecule is generated using photocatalytic systems, it can be considered that the rate of this reaction depends upon the proton concentration, that is the pH of the solution. This aspect is of particular importance since, in the case of photoreforming, the presence of a sacrificial organic species (i.e., pollutant) is required. In other words, since wastewaters can be used to feed the photocatalytic hydrogen generator, hopefully without any change of their specific pH, it is particularly important to understand how this variable influences the performance of the system. To this purpose, the papers considered for the present review were analyzed and the results are reported in Table 2.1, Column IV. From these data, it can be said that a certain attention to the effect of pH on hydrogen generation was paid by researchers, although in many cases neither explanations were given for the effect recorded nor indications were reported about the reasons for the choices adopted.

On the other hand, some attempts to understand the reasons for the effects observed were also recorded. For example, Wu et al. [107] explored a pH range of 2.0-12.0 and found that a weak basic pH (ca. 10) is more propitious to promote the hydrogen production rate than acidic or strong basic (>10) pH. They believed that the surface properties of the photocatalyst (i.e, the OH radical concentration and the surface charge density) and the shift of the band gap energy depend on the change in pH. They indicated also the acidic condition as detrimental for hydrogen generation, due to a lower stability of the copper species on the surface of TiO_2 particles.

Nada et al. [30] proposed a copper phthalocyanine photosensitized TiO_2-RuO_2-MV^{2+} system for hydrogen production from methanol, and recorded the highest hydrogen production rate under acidic conditions. According to their results, at low pH values more protons are adsorbed on the TiO_2 surface, which increases the possibility of proton reduction to H_2 by photogenerated electrons in the CB of TiO_2 (e^-_{CB}); moreover, under acidic conditions, MV^{2+} reduction by e^-_{CB} is identified as the rate controlling step. At high pH values, Ru^{4+} and Cu^{2+} precipitate as hydroxides.

Lanese et al. [41] reported that a reduction in proton concentration, at pH raising from 0 to 1.0, does not result in any appreciable decrease in system reactivity, whereas a significant decline is noted at pH=2.0. This behavior could be considered as the result of a change in the rate determining step. In other words, when proton concentration decreases, the rate of reaction of this species with free electrons decreases and this step limits the overall rate of hydrogen generation.

Xu et al. [93] attributed the decline of hydrogen generation rate to copper leaching from the photocatalyst, when the solution pH drops. According to their study, when the pH value is 1, 83.8% of copper from the CuO-TiO_2 photocatalyst will be released into the solution after 1 hour (54.0% and 2.2% for pH=3 and 5, respectively). Copper ions in solution weaken the capability to accept excited electrons from TiO_2, inducing deactivation of the catalyst for hydrogen production. Leaching of copper into the solution was also reported by others, such as Xu et al. [60]. They observed a small decline in Cu content, since the system pH decreased progressively because of the generation of CO_2 and HCOOH byproducts, causing Cu dissolution into the solution. Consequently, the efficiency of hydrogen production was reported to decline moderately with time.

Other researchers recorded the existence of an optimal pH value. Brahimi et al. [82] conducted experiments using a $CuAlO_2$-TiO_2 catalyst in the pH range of 5.5-14.0. They observed an enhancement in H_2 generation as pH was increased until a maximum value at pH≈11, beyond which a marked decrease was noted. Assuming that the electronic bands of $CuAlO_2$ are pH-insensitive, they concluded that a change in pH can substantially lead to the modification of the band positions of TiO_2 and, to be more precise, to their negative shift with increasing pH.

Jin et al. [98] explored a very wide pH range (1.0-14.0) and found that by adjusting the pH value from 14 to 1.0 (by addition of nitric acid) the rate of hydrogen production decreased to a minimum just at pH 1.0. At pH 14, no significant changes were noted before and after the reaction in the absorption spectra of the photocatalyst, whereas a small decline in absorption was recorded at pH 1.0.

3. Aim of the thesis

This study was devoted to a nano TiO_2-photocatalytic system based on UV photoreforming of organic sacrificial molecules by in situ photoreduction of cupric ions. As emerged from the literature review, increasing research efforts have been recently devoted by researchers to develop copper-based TiO_2 photocatalysts for hydrogen generation through photocatalytic reforming of organics.

The performances of the system studied were evaluated in terms of hydrogen generation at varying selected operating parameters. Partial goals of this investigation are reported hereinafter.

✓ Evaluation of the effect of adopting various oxygenated organic substrates as sacrificial organic agents. In particular, selected alcohols and carboxylic acids were employed in order to compare the role of the substrate structure on hydrogen production.

✓ Assessment of the role of the TiO_2 crystallographic phases (anatase, rutile and anatase/rutile) in hydrogen generation. The relationship between photocatalytic activity and physical-chemical properties of the catalyst was assessed by performing a thorough catalyst characterization including X-Ray diffraction, Dynamic Light Scattering, Thermogravimetry, Energy-dispersive X-ray Spectroscopy, FT-IR and Diffuse Reflectance UV Spectroscopies, Photolumincesce, High Resolution Transmission Electron Microscope, Field Emission Scanning Electron Microscopy analyses.

✓ Development of a suitable mathematical model capable of simulating hydrogen production over the same catalyst (nano-$Cu_{(s)}/TiO_2$) when glycerol or methanol were adopted as sacrificial agents.

Investigation on the presence of chloride ion in the aqueous matrix when formic acid was employed as sacrificial agent.

4. Materials and methods

4.1 Chemicals

All organic compounds used as sacrificial agents, TiO_2 Aeroxide P25, TiO_2 pure anatase phase, TiO_2 pure rutile phase, cupric sulfate pentahydrate, sodium chloride, chromotropic acid disodium salt dehydrate, perchloric acid and sodium hydroxide were purchased from Sigma Aldrich. Doubly glass-distilled water was used throughout this study. Sulfuric acid was purchased from Carlo Erba Reagents.

4.2 Hydrogen production device

Photocatalytic runs were performed in a batch cylindrical glass jacketed reactor (300 ml) with an outer diameter of 6.5 cm and a height of 40 cm wrapped with an aluminum foil. The optical path length was 1.10 cm

The reactor was thermostated at 25 °C and equipped with a magnetic stirrer. On the top of the reactor, an inlet allowed to feed reactants and nitrogen gas, and an outlet was used to collect liquid and gaseous samples at varying reaction times.

The reactor was endowed with a high-pressure mercury vapor lamp by Helios Italquartz (power input: 125 W), principally emitting at 305, 313, and 366 nm (manufacturer's data). The effective radiative powers of the lamp ($I_{\lambda_i}^0$) at 305 (determined through determined through hydrogen peroxide photolytic experiments [188]), 313 nm (determined by valerophenone actinometry [189]), and 366 nm (measured using a UV radiometer Delta Ohm HD 2102.1) are $2.56 \cdot 10^{-6}$, $2.70 \cdot 10^{-6}$ and $3.30 \cdot 10^{-6}$ $ein \cdot s^{-1}$, respectively. The lamp was located inside a glass cooling jacket in the center of the reactor and surrounded by the reacting solution. A schematic illustration of the reactor is provided in Figure 4.1.

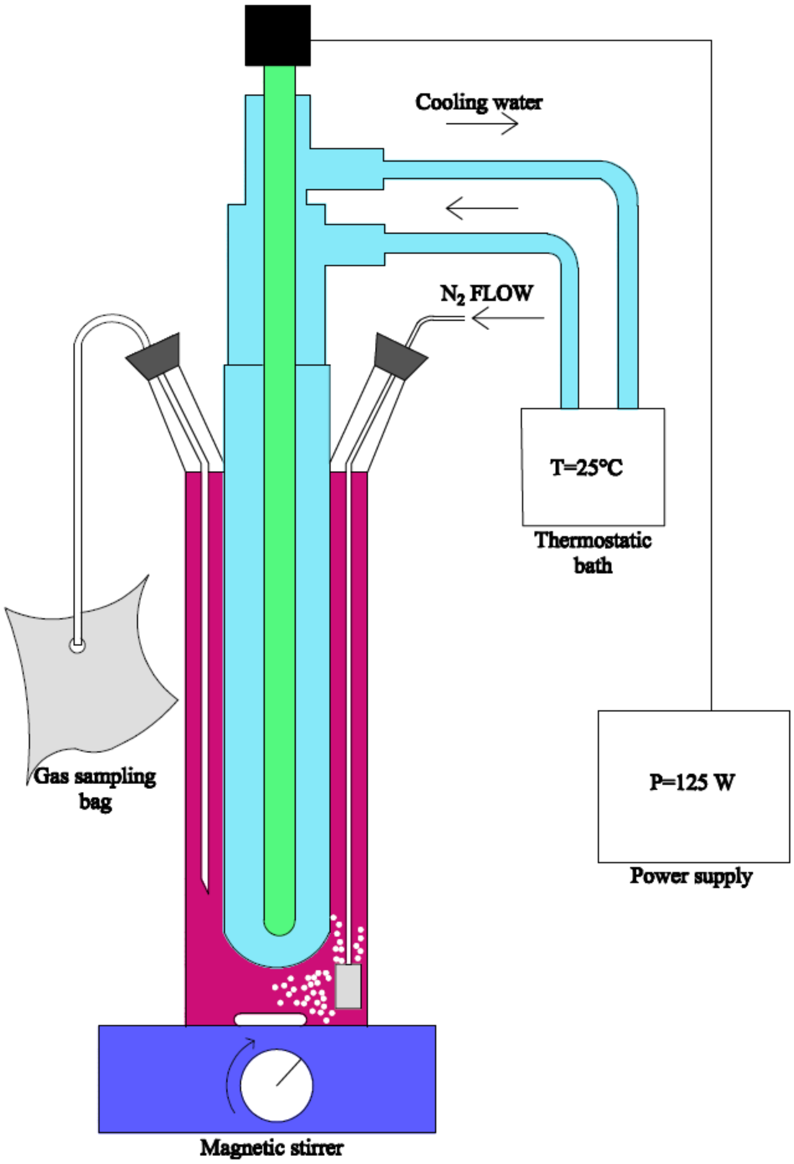

Figure 4.1: Batch annular reactor.

4.3 Photocatalytic experiments procedure

For each run a fixed amount of catalyst was initially suspended in an aqueous solution containing the sacrificial species chosen for the experiment.

In order to avoid the undesired reaction between dissolved oxygen and photogenerated electrons, before starting the photocatalytic experiment, a nitrogen stream was bubbled into the solution for 30 minutes. Moreover, throughout the photocatalytic runs, nitrogen was continuously fed at a flow rate of 0.3 L•min^{-1} in order to prevent the presence of air into the reactor. In selected experimental runs, a solution of sodium nitrite (1 M) was used for controlling the temperature (25 °C) and for cutting-off UVA radiation emitted by the lamp ($\lambda < 400$ nm) [108].

At different reaction times, gaseous samples were collected by means of Tedlar gas sampling bags and injected into the gas-chromatograph to record the rate of hydrogen generation. The liquid samples, collected at different reaction times, were quickly filtered on regenerated cellulose filters (pore diameter 0.20 μm, Scharlau) and the filtrates were used to measure total dissolved copper concentration and selected organic species concentration.

The measurements of transmitted radiant power were carried out on the external wall of the reactor through a digital radiometer (Delta Ohm HD 2102.1). In particular, the irradiances emerging from the reactor in the ranges 315-400 nm and 400-1100 nm were recorded.

4.4 Analytical methods

At different reaction times gaseous and liquid samples were collected by means of Tedlar gas sampling bags (1 liter) and glass syringe (10 ml). Gaseous samples were analyzed by a gas-chromatograph (Agilent 7820A) equipped with a HP-PLOT Molesieve 5A column (Agilent) and a TCD detector using argon as the carrier gas.

The concentration of cupric and cuprous ions in solution was measured by means of a colorimetric method using an analytical kit (Macherey-Nagel) based on oxalic acid bis-cyclohexylidene hydrazide (cuprizone). A UV/Vis spectrophotometer (Cary 100 UV-Vis Agilent) was employed for the measurements at a wavelength of 585 nm. The pH of the solution was monitored by means of an Orion 420p pH-meter (Thermo). The irradiances emerging from the reactor were measured by means of a UV-Vis radiometer (Delta Ohm HD 2102.1).

When formic acid was employed as sacrificial agent, its concentration was measured by means of HPLC analyses. For this purpose, the HPLC apparatus (Agilent 1100) was equipped with a UV–Vis detector (λ=210 nm) and a Alltech OA–1000 column, using a mobile phase of sulfuric acid $2.5 \cdot 10^{-3}$ mol/L, flowing at 0.8 mL/min.

On the other hand, when methanol was adopted as hole scavenger the concentration of formaldehyde was determined by the colorimetric method by Bricker and Vail [109], based on the use of chromotropic acid.

4.5 Recovery of the catalyst

At the end of the run, the suspension was allowed to settle overnight under inert atmosphere producing two distinct layers: aqueous solution on the top and Cu-modified TiO_2 particles deposited on the bottom. After removal of most part of the aqueous solution by decanting it, the remaining part was then evaporated by means of a gentle inert flow.

4.6 Catalysts characterization

4.6.1 Structural and morphological characterization

Structural and compositional characterization of the samples was performed by dynamic light scattering analysis (DLS), X-ray diffraction (XRD), Brunauer–Emmett–Teller (BET) N_2 adsorption analysis and high-resolution transmission electron microscopy (HR-TEM).

XRD measurements were performed using a PANalytical diffractometer with a nickel filter and Cu Kα radiation. BET analysis allowed determining the specific surface area (SBET), that was evaluated by generating seven-point isotherms at 77 K for N_2 adsorption (Autosorb-1, Quantachrome) using the char sample capable of providing a specific surface area equal to 5 m^2 in the sample cell.

Dynamic light scattering analyses (DLS) were performed through a Malvern Instruments Master Sizer 2000 granulometer operating with water as the dispersion solvent down to a minimum particle size of 0.02 μm.

Information on the overall surface morphology of the photocatalysts was provided by a field emission scanning electron microscopy (ESEM, Philips XL 30 ESEM-FEG), while more detailed information on crystal size and crystal structure were obtained using a JEM-2010F (JEOL) high-resolution transmission electron microscope (HR-TEM) with field emission gun at 200 kV. The samples were prepared for HR-TEM measurements by dispersing the obtained powders in acetone using an ultrasonicator (2510RDH, Bransonic) over 30 min and then fixed on a carbon coated copper grid (FCF400-Cu, FROMVAR).

4.6.2 Compositional characterization

Energy-dispersive X-ray spectroscopy (EDX) measurements for elemental mapping of titanium and copper were performed by a Fei Inspect Microscope, Column E-SEM W (Source: 200 V – 30 kV, filament: tungsten) equipped with an Everhart – Thornley detector (ETD). Further information was obtained through Fourier Transform Infrared (FT-IR) spectroscopy and thermogravimetric analysis (TG). FT-IR characterizations employed a Nexus spectrometer that recorded the absorbance spectra of the samples in 400–4000 cm−1 wavenumber range. For TG analysis, we used a thermogravimetric Netzsch TG209 apparatus, operating at a heating rate of 10 °C/min under a nitrogen atmosphere.

4.6.3 Optical and electronic characterization

Diffuse Reflectance UV–Vis (DRUV) measurements were performed to establish the optical band gap by using a Jasco spectrophotometer and $BaSO_4$ as a reference. The optical absorption was measured in the 190–850 nm wavelengths range.

Photoluminescence (PL) measurements in controlled ambient gas were used to compare the charge recombination efficiency of the TiO_2 supports and of the Cu-TiO_2 composites and to correlate them with the photocatalytic efficiencies. The PL experiments were carried out using an excitation source in the ultraviolet emission line of a He-Cd laser (325 nm wavelength, corresponding to a photon energy at about 3.82 eV). The PL light was focused on the input end of an optical fiber bundle coupled with a 320 mm focal length spectrometer. The spectral acquisition was provided by a Peltier-cooled CCD camera. The stabilization of nitrogen atmosphere in the test chamber was provided by a mass flow control system.

Electron Paramagnetic Resonance (EPR) spectroscopy experiments were carried out by means of X-band (9 GHz) Bruker Elexys E-500 spectrometer (Bruker, Rheinstetten, Germany), equipped with a super-high sensitivity probe head. Solid samples were transferred to flame-sealed glass capillaries which, in turn, were coaxially inserted in a standard 4 mm quartz sample tube. Measurements were performed at room temperature. The instrumental settings were as follows: sweep width, 1500 G; resolution, 1024 points; modulation frequency, 100 kHz; modulation amplitude, 1.0 G. 128 scans were accumulated to improve the signal-to-noise ratio.

Raman spectra were achieved using a Horiba XploRA Raman microscope system with a 100·objective (NA 1.4, Olympus). The laser source was a frequency doubled Nd:YAG-solid state laser (λ= 532 nm, 12 mW maximum laser power at the sample). The calibration of the system was performed against the Stokes Raman signal of pure Si at 520 cm^{-1} using a silicon wafer.

5. Results I

In-situ photodeposited Cu-TiO_2 catalyst for phoreforming of organics

5.1 Introduction

As previously discussed, systems based on titanium dioxide on which copper species were deposited or formed as a co-catalyst were recently proposed to be promising catalysts for photoreforming. Amongst the techniques so far adopted to include copper species on TiO_2 catalysts [37], only few examples of *in situ* photodeposition have so far been reported in the literature of TiO_2 doping with copper [62,67,110]. Moreover, it is important to stress that each of these studies focused on a specific sacrificial agent.

This investigation aimed at assessing the use of copper-TiO_2-based photocatalysts prepared by *in situ* photodeposition in photoreforming processes for hydrogen generation. In addition, many different oxygenated organic substrates were tested to evaluate and compare effects of substrate structure on hydrogen production.

5.2 Results

Figures 5.1a-d show data recorded during a typical photoreforming run for hydrogen generation using bare TiO_2-P25 and Cu-modified TiO_2-P25 catalysts and glycerol as sacrificial agent. The addition of cupric ions to the reacting system results into their rapid disappearance from the solution (data not shown) and a prompt increase (Fig. 5.1a, from point ① to ②) in hydrogen generation rate with respect to the value measured in presence of bare TiO_2-P25. At larger time hydrogen production rate decreases until it approaches a plateau (Fig. 5.1a, point ③). A contemporary decrease in both pH (Fig. 5.1b), which reduces from an initial value of 6.4 to 2.9, and irradiances (Figs. 5.1c,d) - measured on the external wall of the reactor - is observed after copper addition into the solution.

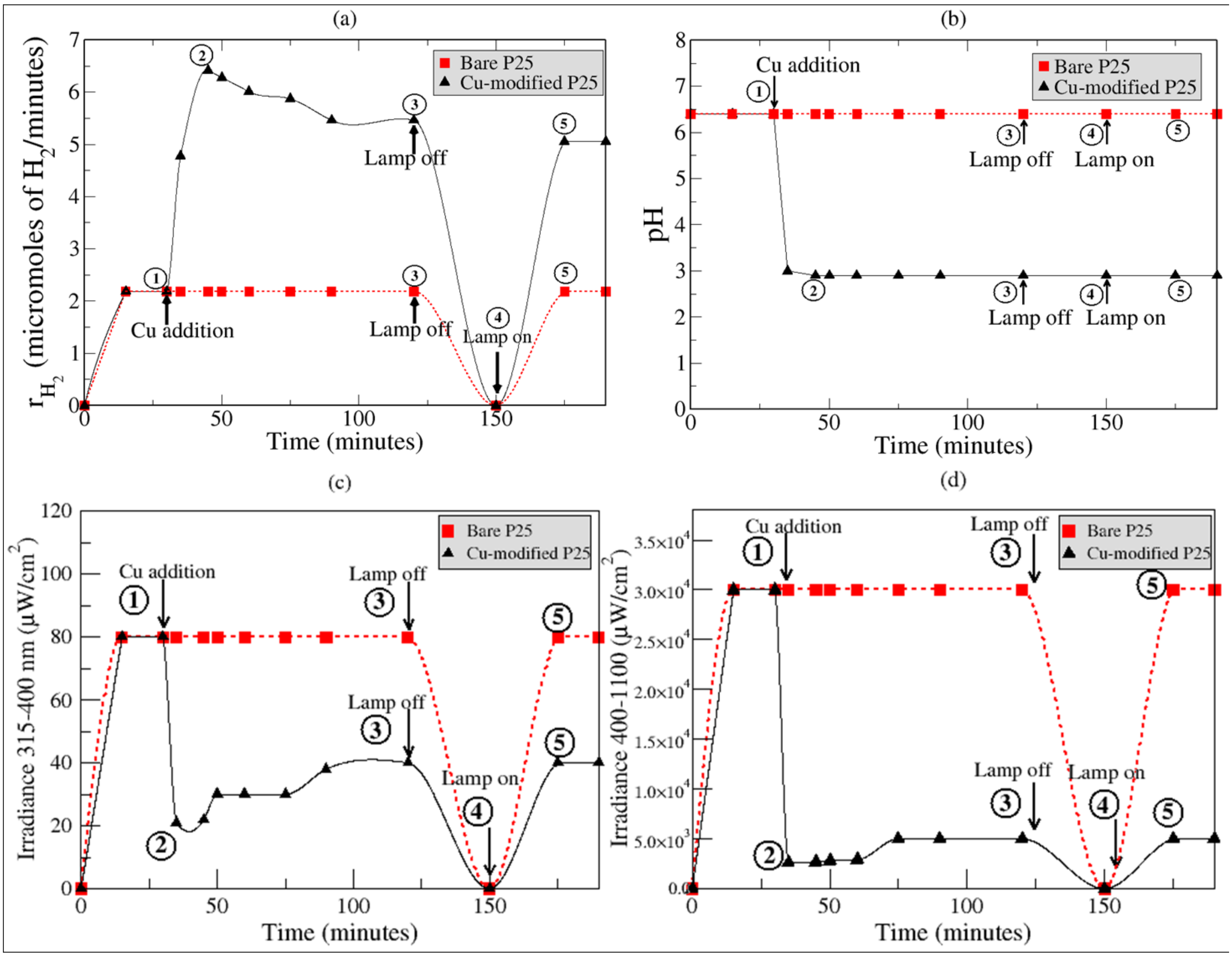

Figure 5.1: Hydrogen production rate (**a**), pH of the solution (**b**), irradiance between 315-400 nm (**c**) and 400-1100 nm (**d**) for bare TiO_2 (■) and Cu-modified TiO_2 (▲) during a typical photoreforming run under de-aerated conditions.

[$C_3H_8O_3$]$_o$=0.8 M; [Cu(II)]$_o$=0.8 mM; TiO_2-P25 load = 500 mg•L^{-1}; pH$_o$=6.4.

In particular, it is important to stress that the irradiance values recorded in both the UV and the visible range decrease within 30 minutes of reaction time, thus indicating a higher absorption capability of the resulting solid catalyst with respect to TiO_2-P25 catalyst initially charged into the reactor. A marked change in color of the liquid samples withdrawn from the reactor is recorded from white typical of TiO_2 particles to purple (for further information see the Appendix, Fig. A1), thus indicating that some chemical transformations occur during this interval. To achieve additional information about the system behavior, the lamp was switched off after 120 minutes of reaction and, after checking that hydrogen production was stopped, it was again switched on (point ④). The analyses of the gaseous samples collected after this procedure indicate that hydrogen production rate immediately achieves a value equal to that of previously observed plateau (point ⑤). No occurrence of any overshoot other than that recorded at the beginning of the photocatalytic run (① → ③) is observed, thus outlining that probably its presence is strictly related to the photodeposition of some copper species on TiO_2 particles. The run was repeated twice, demonstrating good reproducibility of the results (data not reported).

The investigations were successively extended to evaluate the effects of varying Cu-modified TiO_2-P25 catalyst load, keeping constant the Cu(II)/TiO_2 mass ratio (10 wt%). Figures 5.2a,b show the hydrogen generation rate corresponding to the plateau obtained at different catalyst loads along with the irradiance values. Consistently with heterogeneous catalytic processes, hydrogen generation rate increases almost linearly for low increments of catalyst load; further additions of TiO_2 amount to the reacting solution firstly result no more useful and successively appear detrimental for the process itself (Fig. 5.2a). Figure 5.2b shows that the irradiance values collected in the UV and the visible range sharply reduce increasing the TiO_2 load between 50 mg/L and 250 mg/L. On the other hand, the decreasing trend of irradiances in both ranges appears to slightly abate for further increases in catalyst load.

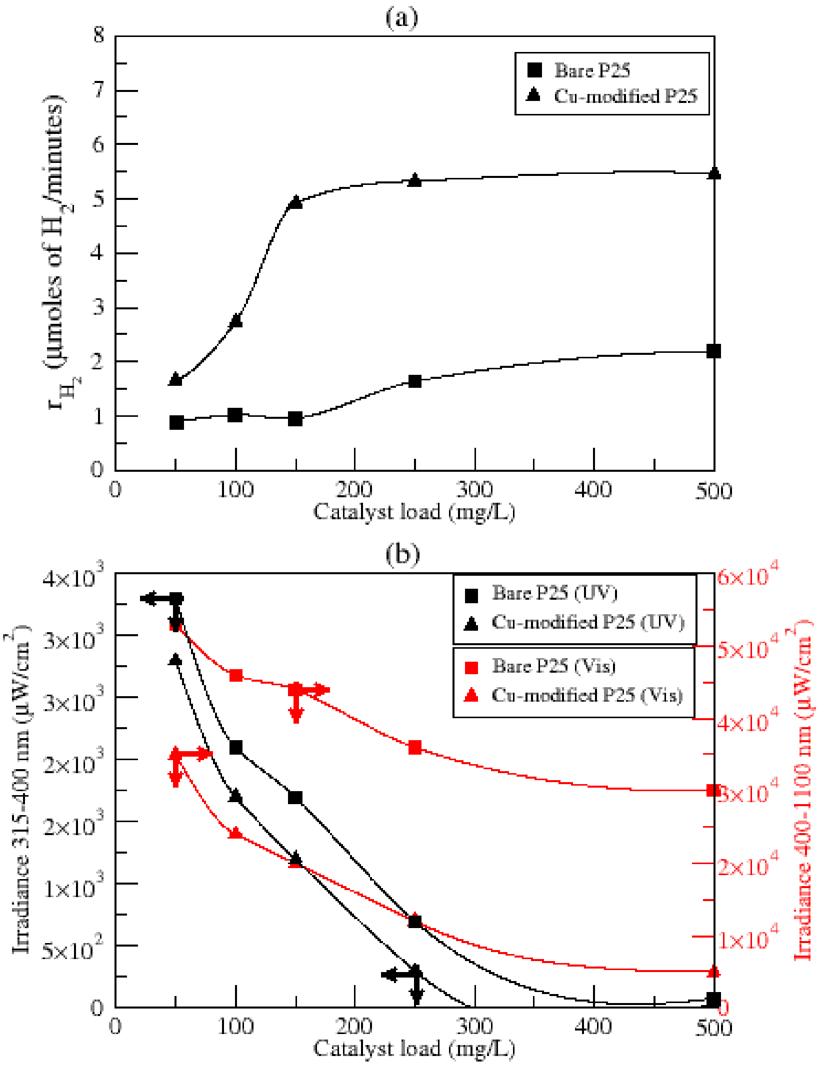

Figure 5.2: Effects of catalyst load: hydrogen production rate (**a**), irradiance between 315-400 nm and 400-1100 nm (**b**) for bare TiO_2-P25 (squares) and Cu-modified TiO_2-P25 (triangles). TiO_2-P25 load =50÷500 mg/L; $[C_3H_8O_3]_o$=0.8 M; pH_o=6.4.

An attempt to understand if this approach to hydrogen production through organic photoreforming can be of general use prompted us to investigate the system behavior using different sacrificial substrates. A large group of organic species was tested under the experimental conditions described for the run whose results are given in Fig. 5.1. Table 5.1 reports all the collected data for each run with a different chemical species: a behavior similar to that indicated in Fig. 5.1 is recorded in terms of hydrogen generation rate, irradiance, pH and cupric ion concentration against time (data not shown). As a general comment to the data reported, it is possible to state that the proposed system works as a catalyst for hydrogen generation, starting from a great many different organic species. Nevertheless, the observed rates varied from 5.50 μmol•min^{-1} for glycerol to 0.55 μmol•min^{-1} for benzyl and isopropyl alcohols and zero for acetic acid only. It is noteworthy to stress that, even if acetic acid, benzyl alchohols and isopropyl alcohols are used as sacrificial agent, a reduction of cupric ions is observed, although no hydrogen production is recorded (Table 5.1).

Sacrificial agent	**Cu^{2+} reduction**	**H_2 production**	**pH_o**	**pH_{final}**	**r_{H2} bare TiO_2-P25 (µmol•min^{-1})**	**r_{H2} Cu-TiO_2-P25 (µmol•min^{-1})**
Glycerol	Yes	Yes	6.40	2.90	2.18	5.50
Methanol	Yes	Yes	5.50	2.9	0.89	4.37
Formic acid	Yes	Yes	2.00	1.60	0.1	4.07
Sodium formate	Yes	Yes	8.20	9.70	1.23	3.69
Ethylene glycol	Yes	Yes	3.76	2.90	0.55	3.48
Propylene glycol	Yes	Yes	5.40	2.80	1.46	3.46
Glucose	Yes	Yes	5.40	2.80	0.34	2.50
Ethanol	Yes	Yes	5.40	2.90	1.50	2.00
Oxalic acid	Yes	Yes	0.10	0.45	0.10	0.96
Benzyl Alcohol	Yes	Yes	4.80	2.90	0.41	0.55
Isopropyl alcohol	Yes	Yes	5.50	2.80	0.14	0.55
Acetic acid	Yes	No	2.24	2.40	-	-

Table 5.1: Data collected by testing under defined experimental conditions ($[Cu(II)]_o$=0.8 mM; TiO_2 load = 500 mg•L^{-1}) a selected group of organics: hydrogen production and dissolved copper reduction capacities, starting and final pH of the reacting solution, hydrogen production rate in presence of bare TiO_2 (r_{H2} bare TiO_2-P25), hydrogen production rate in presence of Cu-modified TiO_2 (r_{H2} Cu-TiO_2-P25) before switching off the lamp (t=120 min).

5.3 Discussion

According to Tung [111], it is possible to explain the data reported in Fig. 5.1 by assuming that, upon irradiation of TiO_2 particles, the photogenerated charge carriers make possible in the very early stages of the process:

- the reduction of cupric ions to cuprous one or to zero-valent copper by photogenerated electrons ($r_{5.1}$), along with proton reduction to form hydrogen atom:

$$\mathrm{Cu(II)} + \mathrm{e}_{\mathrm{CB}}^{-} \rightarrow \mathrm{Cu(I)} + \mathrm{e}_{\mathrm{CB}}^{-} \rightarrow \mathrm{Cu(0)} \qquad r_{5.1}$$

- the oxidation of the sacrificial organic species by photogenerated positive holes ($r_{5.2}$):

$$\mathrm{S}_{\mathrm{ads}} + \mathrm{h}_{\mathrm{VB}}^{+} \rightarrow \mathrm{S}_{\mathrm{ox}} + \mathrm{H}^{+} \qquad r_{5.2}$$

Even though this view seems to be highly reasonable, it is necessary to go further into details of the process and define the oxidation state of copper species formed during the photocatalytic process.

Firstly, the increase in visible-light absorption during the first stage of the process is consistent with the reduction of cupric ions to cuprous oxide, which is almost insoluble in water and could precipitate even in acidic pH conditions [67,112]. Cuprous oxide, a p-type semiconductor, is reported to have a band gap of about 2.0-2.2 eV [113]: this value is smaller than TiO_2 (3.0-3.2 eV) and could properly justify the increase in absorption of the visible radiation.

Moreover, the precipitation of cuprous oxide can be partially responsible for the decrease in pH. To explain the decrement of pH, it is worth noticing that two proton ions are generated from the oxidation of the organic species (3), and two additional proton ions derive from the formation of Cu_2O (4) through the reaction between cupric ions and photogenerated electrons [114]:

$$-\mathrm{CH_2OH} + 2\mathrm{h}_{\mathrm{VB}}^{+} \rightarrow -\mathrm{CHO} + 2\mathrm{H}^{+} \qquad r_{5.3}$$

$$2\mathrm{Cu(II)} + \ 2e_{CB}^{-} + \mathrm{H_2O} \rightarrow \mathrm{Cu_2O} + \ +2\mathrm{H^+} \qquad r_{5.4}$$

Therefore, the moles of protons generated are twice as many as those of cupric ions reduced. This means that, for a starting cupric ion concentration equal to 0.8 mM such as in this study, a protons concentration of 1.6 mM arises from reactions 3 and 4. For a starting pH of 5.0, the initial concentration of proton ions may be neglected with respect to that due to the occurrence of the reactions $r_{5.3}$ and $r_{5.4}$. Accordingly, a final pH of about 2.8 (pH=-log(1.6·10^{-3})) is estimated, which agrees with values measured during the runs.

On these basis, a direct evidence for the presence of cuprous oxide in the system was investigated. Figure 5.3a shows the UV-visible absorption spectra for some selected samples recovered at the end of the photoreforming runs. In particular, the samples analyzed can be classified as reported below:

i. Cu-modified TiO_2-P25 recovered after a typical photoreforming run in presence of cupric ions and TiO_2-P25;
ii. Cu_2O-TiO_2-P25 resulting from a photoreforming run carried out by adding Cu_2O to a TiO_2-P25 suspension;
iii. TiO_2-P25 and Cu_2O composed of bare P25 titanium dioxide and pure cuprous oxide, respectively.

The sharp basal absorption edge located at about 416 nm in bare TiO_2-P25 is consistent with the pristine bandgap of P25 (3.2 eV) [115], whereas pure Cu_2O shows a broad absorption band in the visible spectral range, starting from about 430 nm.

Figure 3a indicates that Cu-modified TiO_2-P25 and Cu_2O-TiO_2-P25 have similar absorption spectra and both the samples absorb at higher wavelengths (λ>400 nm) with respect to bare TiO_2-P25 sample.

Moreover, from a careful investigation of the DRUV spectra in the wavelength range of 520-580 nm, where signals belonging to plasmon resonance of copper nanoparticles fall [116,20], a large absorption band may be observed for both the copper-based-titanium dioxide catalysts. These data clarify that in the first stage of the process, during which Cu-modified TiO_2-P25 forms, the light absorption behavior of the solid suspended in the reactor drastically change, assuming a relevant character in the visible range. The intensity measured in UV-visible spectra is also expressed as the value of the Kubelka–Munk function F(R).

Figure 5.3b shows the energy gap values calculated by linearization of Tauc plot of $(F(R)h\nu)^{1/2}$ versus photon energy ($h\nu$). The red shift of the absorption edge from 386 nm (for the TiO_2-P25) to 431 nm (for Cu_2O-TiO_2-P25) is consistent with an energy band gap of about 2.6 eV. However, the last value does not totally agree with that reported in the literature for Cu_2O (2.2 eV). The results collected raised some doubts about the nature of the species formed on TiO_2-P25 surface.

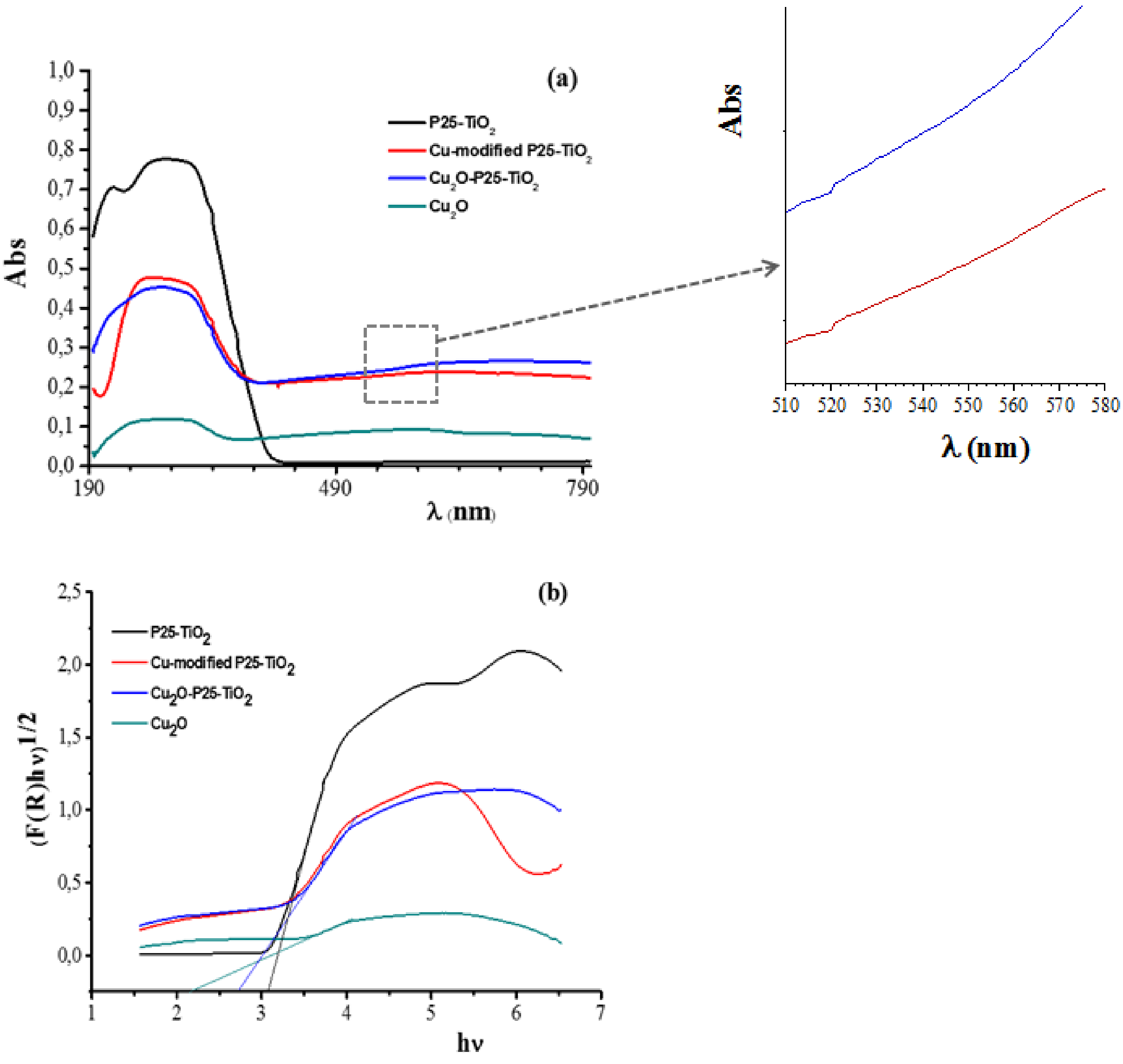

Figure 5.3: DRUV absorption spectra (panel a) and plots of $(F(R)h\nu)^{1/2}$ versus photon energy, $h\nu$, (panel b) for Cu-modified TiO_2-P25, Cu_2O- TiO_2-P25, TiO_2-P25 and Cu_2O.

To collect clearer indications on these species, Raman spectra (Fig. 5.4a), EPR analysis (Fig. 5.4b) and XRD patterns (Fig. 5.4c) were planned and carried out on some catalyst samples.

The Raman spectrum of Cu-modified TiO_2-P25 is characterized by an intense peak at 148 cm^{-1} and three short peaks at 400 cm^{-1}, 520 cm^{-1} and 640 cm^{-1}, which corresponds to the active modes of bare TiO_2-P25. Actually, the typical peak of Cu_2O corresponding to the second-order overtone at 219 cm^{-1} [117] is not observed in the spectrum of the catalyst formed *in situ*.

Figure 5.4b shows EPR spectra on Cu-modified TiO_2-P25 and Cu_2O- TiO_2-P25 samples. As a reference, the EPR spectrum of the TiO_2 Degussa P25 in presence of cupric ions before irradiation is reported, showing the typical signal of Cu(II)/TiO_2 system [118]. For both the catalysts no paramagnetic signals are detectable, thus clearly confirming the absence of Cu^{2+} species adsorbed on the TiO_2-P25 catalyst surface.

On the other hand, comparing to each other the XRD spectra shown in Fig. 5.4c, for the samples collected after the photocatalytic processes it is possible to distinguish the presence of two peaks at 2Θ values 43°3’ and 50°5’, which exactly match those of zero-valent copper, whereas no peaks due to Cu_2O are observed. Conversely, the peaks related to the occurrence of Cu_2O are present and no signals ascribed to zero-valent copper are found in the XRD spectrum of a sample obtained by adding Cu_2O to a P25 suspension without UV irradiation.

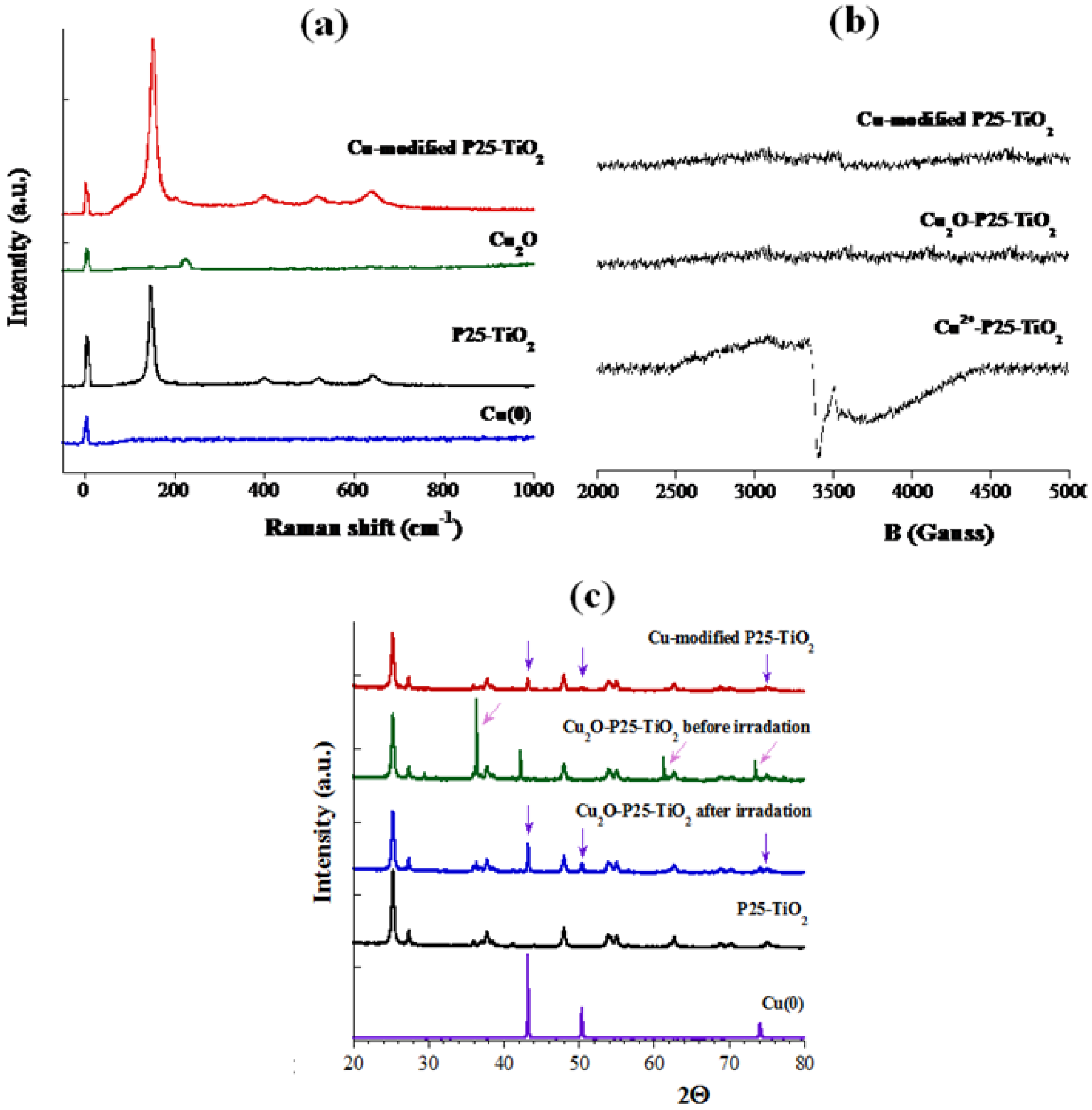

Figure 5.4: Raman spectra (panel a), EPR spectra (panel b) and XRD pattern (panel c) registered for Cu-modified TiO_2-P25, Cu_2O- TiO_2-P25 before and after irradiation, bare TiO_2-P25 and Cu(0) powders. In panel c, the purple arrows indicate the diffraction peaks corresponding to the Cu(0) species, while the pink arrows are related to the diffraction peaks of Cu_2O.

It is clear that Raman and XRD results do not support the formation of Cu_2O on TiO_2 surface, but only the presence of zero-valent copper particles. Therefore, a different explanation for the absorption in the visible range must be sought.

To this purpose, the crystallite size of zero-valent copper (D) was calculated using XRD data and the Scherrer's equation ($D = \frac{k\lambda}{\beta \cos \Theta}$) where k is a constant (0.94 for spherical particles), λ is the wavelength of the X-ray radiation (0.154 nm), ß is the line width at half maximum intensity of the peak, and Θ is the angle of diffraction (21°6'). The mean size of particles estimated from the Scherrer's formulas is close to 5 nm, thus indicating the formation of zero-valent copper nanoparticles in the first stage of the photocatalytic process.

The increase in hydrogen productivity of zero-valent nanocopper-loaded titania with respect to undoped commercial P25can be mainly ascribed to the existence of Schottky barriers at the metal copper-titania interfaces inhibiting the recombination of photogenerated electrons and holes [119,120].

Due to the disparity between zero-valent copper and TiO_2 work functions, photogenerated electrons move from titania to zero-valent copper as the latter is deposited on the former until the two Fermi levels are aligned, while photogenerated holes are concentrated on the TiO_2 side. This process enhances the efficiency of the photocatalytic process by preventing the recombination of electron-hole pairs.

On the other hand, zero-valent copper, whose presence was confirmed by XRD spectra (Fig. 5.4c), is also important for its contribution to the catalytic activity. Indeed, the metal deposited on TiO_2 plays an essential role as active site on which photogenerated electrons are temporary trapped and successively transferred to proton to generate hydrogen.

It is worth noticing that it is possible to explain the decrease in pH recorded during the runs even if the formation of zero-valent copper particles upon reduction of cupric ions is considered. Indeed, as reported in reaction $r_{5.1}$, in order to obtain two moles of zero-valent copper from two moles of cupric ions it is necessary to have four moles of electrons. As a result, reaction proves that the consumption of four positive holes is required, resulting in the generation of four hydrogen ions. Therefore, once more, for each reduced mole of cupric ion two moles of hydrogen ions form.

According to previous investigations [103,121], when participating to a photocatalytic process each organic substrate may behave either as a species "strongly adsorbed" on the catalyst surface or as a "weakly adsorbed" species. With reference to these situations, two mechanisms are generally reported [122,123] substantially different in the reaction through which the substrate oxidizes. Indeed, for "strongly adsorbed" compounds the oxidation proceeds essentially through a direct reaction of the organic species with surface positive holes (reaction $r_{5.2}$). On the other hand, as stated above, photogenerated electrons may be captured at the very beginning of the process by either cupric and cuprous ions ($r_{5.1}$), and successively by protons resulting into hydrogen generation ($r_{5.5}$):

$$\mathrm{H^+} + \mathrm{e^-_{CB}} \rightarrow \mathrm{H^\bullet} \qquad r_{5.5}$$

For "weakly adsorbed" species, the oxidation proceeds through the interaction between the organic compound dissolved in the solution and surface-bound hydroxyl radicals which form as a result of a trapping process of the holes on the surface of TiO2 ($r_{5.6}$ and $r_{5.7}$):

$$> TiOH + \mathrm{h^+_{VB}} \rightarrow \{> \mathrm{TiOH^\bullet}\}^+ \qquad r_{5.6}$$

$$\{> \mathrm{TiOH^\bullet}\}^+ + \mathrm{S} \rightarrow\, > \mathrm{TiOH} + \mathrm{S_{ox}} + \mathrm{H^+} \qquad r_{5.7}$$

Moreover, surface-bound hydroxyl radicals are also capable to react with photogenerated electrons giving rise to an overall fast recombination ($r_{5.8}$), which makes the occurrence of $r_{5.5}$ negligible:

$$\{> \mathrm{TiOH^\bullet}\}^+ + \mathrm{e^-_{CB}} \rightarrow\, > \mathrm{TiOH} \qquad r_{5.8}$$

Although no literature indications can be found on the behavior of the organic species adopted in the present study as probe molecules, it is reasonable to consider small molecules capable of strongly adsorbing on the TiO_2 surface. This is the case of molecules such as methanol, ethanol, formic acid, and those having more than one single functional group such as 1,2-ethandiol, glycerol, and glucose. On the other hand, it could be supposed that bulky species with a single OH group (e.g., isopropyl and benzyl alcohols) only weakly adsorb on the TiO_2 surface, thus $r_{5.6} - r_{5.8}$ are preferred. When acetic acid is used as sacrificial agent, no hydrogen production is observed. This apparently "*anomalous*" result may be explained on the basis of the photo-Kolbe mechanism [124]. This mechanism takes into account, as first step, the decarboxylation of the organic acid through hole oxidation, as indicated in $r_{5.9}$:

$$\mathrm{RCH_2COOH} + \mathrm{h^+_{VB}} \rightarrow \mathrm{RCH_2^\bullet} + \mathrm{CO_2} + \mathrm{H^+} \qquad r_{5.9}$$

After $r_{5.9}$, under deaerated conditions, carbon centered radicals react with photogenerated electron ($r_{5.10}$), thus preventing the formation of hydrogen [125,126], or give at a lower extent a cross termination ($r_{5.11}$):

$$\mathrm{RCH_2^\bullet} + \mathrm{e^-_{CB}} + \mathrm{H^+} \rightarrow \mathrm{RCH_3} \qquad r_{5.10}$$

$$2\mathrm{RCH_2^\bullet} \rightarrow \mathrm{RCH_2CH_2R} \qquad r_{5.11}$$

Summary

The photocatalytic generation of hydrogen from different oxygenated organic species (mostly alcohols and carboxylic acids) through the adoption of copper-modified TiO_2-P25 catalysts was studied. The photocatalysts were prepared *in situ* by means of a photodeposition procedure. Various measurements done during the experiments (i.e., intensity of radiation emerging from the reactor) and on the recovered photocatalyst (i.e., DRUV, XRD and Raman analysis) support the deposition on TiO_2 surface of Cu nanoparticles with particle size of about 5 nm. The photodeposition of Cu nanoparticles markedly enhances the photoefficiency for hydrogen generation with respect to bare titanium dioxide initially charged in the photoreactor.

Experimental results indicate that, for the most part of the organic species adopted as sacrificial agents, the hydrogen production rates were appreciably higher (e.g., 5.5 μmoles of H_2/minutes for glycerol) than that observed for bare P25 (e.g., 2.1 μmoles of H_2/minutes for glycerol). In presence of benzyl alcohol, 2-propanol and acetic acid, no additional formation of hydrogen is observed, although each analysis done during the experiments confirm the reduction of cupric ions to zero-valent copper.

To explain this behavior, a consistent mechanism was proposed. The mechanism is based on a different oxidation capability of the organic species related to their tendency to adsorb on the catalyst surface. When the species strongly adsorb, beneficial effects are observed in terms of an additional hydrogen generation with respect to bare titanium dioxide. Indeed, a negligible proton reduction occurs in the case of a weak adsorption by the organic species.

6. Results II

Effect of different crystalline phases

6.1 Introduction

Literature findings revealed that commercial TiO_2 samples exhibit contrasting photocatalytic activity for hydrogen production not clearly related to different crystallographic phases (anatase, rutile and anatase/rutile) and intrinsically related to several and different factors, such surface area, crystallinity, particle size, and morphology [140].

The relationship between photocatalytic activity and physical-chemical properties of the catalyst, e.g. surface morphology, crystal structure, particle size, surface defects and optical behavior, is crucial to properly design materials with increased hydrogen production efficiencies.

Structural and surface properties of TiO_2 supports can markedly influence dispersion and oxidation state of copper in Cu-modified TiO_2 materials [141]. This highlights the importance of analyzing and understanding the variables controlling Cu deposition onto TiO_2 surface. The role that TiO_2 surface properties (surface area, oxygen vacancies) play in determining morphology and distribution of Cu nanoparticles during *in-situ* photodeposition was therefore investigated.

To this purpose, the physical-chemical properties and the photoefficiencies for hydrogen production of three TiO_2 commercial samples - i.e. P25, pure anatase, and pure rutile - modified by *in situ* copper photodeposition were compared. In particular, the hydrogen production rates were compared and a physical-chemical characterization was performed through a combined approach of complementary techniques, including X-Ray diffraction (XRD), Dynamic Light Scattering (DLS), Thermogravimetry (TG), Energy-dispersive X-ray Spectroscopy (EDX), FT-IR and Diffuse Reflectance UV (DRUV) Spectroscopies, Photolumincesce (PL), High Resolution Transmission Electron Microscope (HR-TEM), Field Emission Scanning Electron Microscopy (FE-SEM).

6.2 Results

6.2.1 Photocatalytic runs

Figure 6.1 shows the hydrogen production rate measured during the photoreforming of two alcohols used as sacrificial agents (i.e., methanol and glycerol), employing different titanium oxides (P25, anatase and rutile), used as bare (up to 30 min) and after adding cupric ions to the reacting mixture. Several information can be inferred from the plot.

- P25 based catalysts showed in all cases a hydrogen production rate larger than those measured for anatase and rutile based catalysts.
- The addition of cupric ions to the mixture resulted into a marked enhancement of the rate of hydrogen production with respect to bare materials.
    - In presence of P25 based catalyst (with or without copper), a higher generation rate was recorded when glycerol was used as hole scavenger.
    - After the cupric sulfate addition, hydrogen generation rate in the presence of P25 undergoes a marked increase for both sacrificial agents (circles) with respect to anatase (triangles) or rutile (squares).
    - Under the adopted experimental conditions, the hydrogen rate productions approached, in all the cases, a plateau after 1 hour from the cupric ions additions.
    - All the photocatalysts were not active under visible light, i.e., for radiations with wavelength higher than 400 nm.

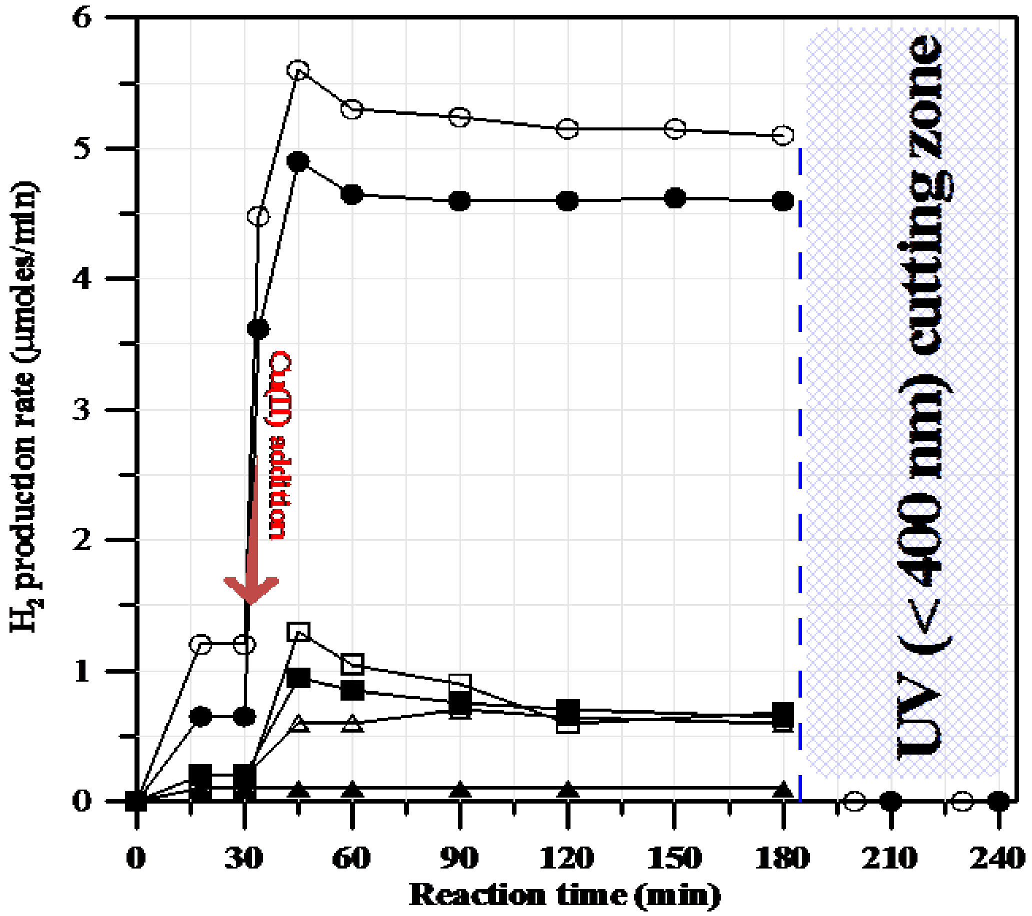

Figure 6.1: Effect of TiO_2 type on the hydrogen production rate. TiO_2 load: 500 mg/l, Cu/TiO_2 ratio: 10% w/w. Hole scavenger agent (10% v/v): (empty symbols) glycerol 0.82 M; (full symbols) methanol 2.47 M.

(○,●) P25-TiO_2 based catalyst; (□, ■) rutile-TiO_2 based catalyst; (△, ▲) anatase-TiO_2 based catalyst.

Figures 6.2a,b show respectively the profiles of copper dissolved normalized concentration and the pH of the mixture using methanol as hole scavenger.

The decrease in cupric ions concentration (Fig. 6.2a) and pH (Fig. 6.2b) were due to copper photodeposition over different titania supports, as previously assessed for P25 (see Chapter 5), according to the simultaneous occurrence of reactions of cupric ions with photogenerated electrons:

$$Cu(II) + 2\,e^- \longrightarrow Cu(0) \qquad r_{6.1}$$

and alcohol with positive holes:

$$R\text{-}OH + 2\,h^+ \longrightarrow R_{ox} + 2\,H^+ \qquad r_{6.2}$$

As it can be noticed, the largest rates of copper photodeposition (Fig. 6.2a) and pH decrease (Fig. 6.2b) are observed for P25 (circles), whereas the lowest are associated to anatase (triangles). A similar trend was observed using glycerol as sacrificial agent (data not shown). Moreover, a change of reaction rate for copper photodeposition was recorded within the first two minutes after lamp switching on for rutile and P25 based catalysts, and within four minutes for anatase. This result may be mainly ascribed to the requirement for the lamp to warm up and reach maximum light emission (dashed line).

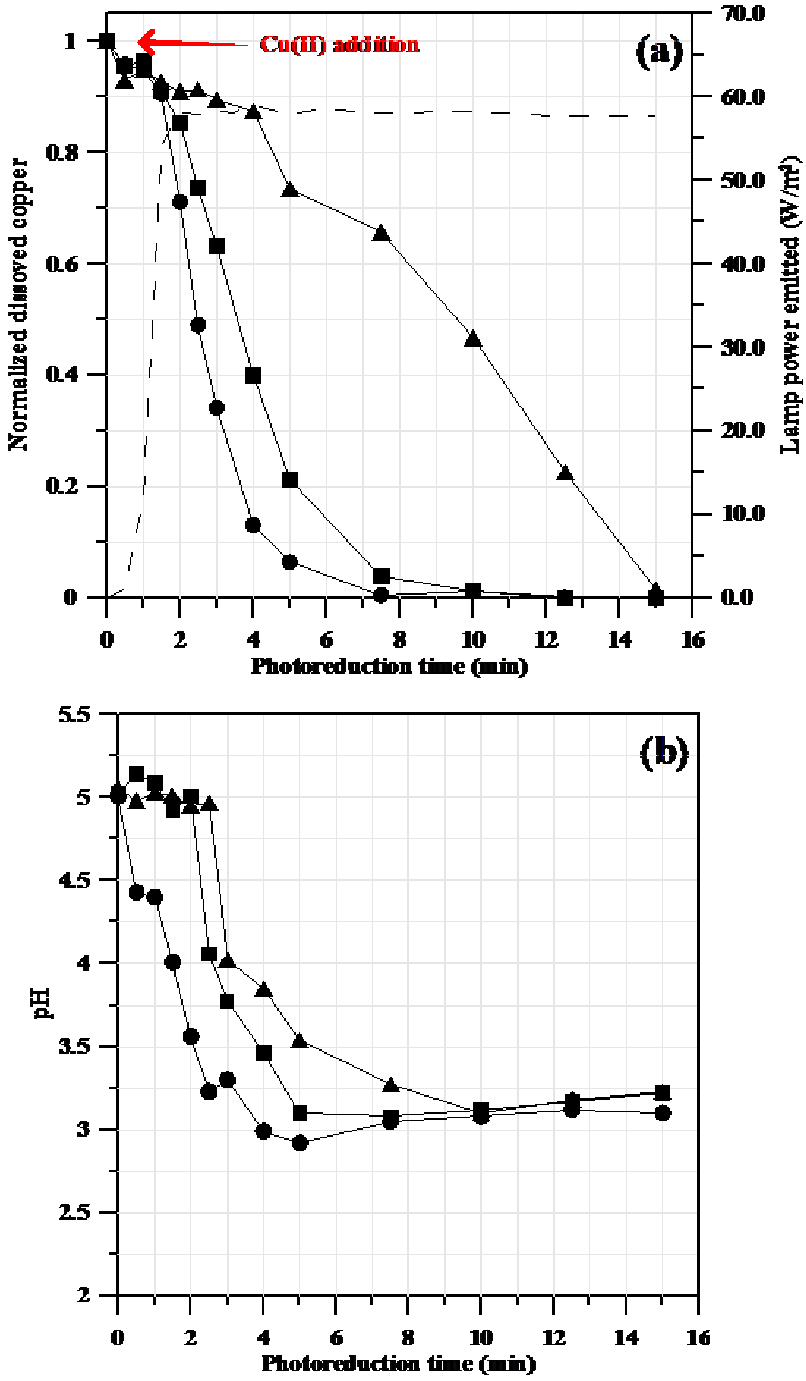

Figure 6.2: Dissolved copper photoreduction **(a)** and pH **(b)** profiles. TiO_2 load: 500 mg/l, Cu/TiO_2 ratio: 10% w/w. Hole scavenger agent: methanol 10% v/v.

(●) P25-TiO_2 based catalyst; (■) rutile-TiO_2 based catalyst; (▲) anatase-TiO_2 based catalyst; (--) lamp power emitted ($\lambda < 400$ nm).

6.2.2 Overall power transmission

The transmitted radiant powers of the suspension were measured in the wavelength range of 315-400 nm for TiO_2 containing suspensions before and after the cupric sulfate additions (Figure 6.3).

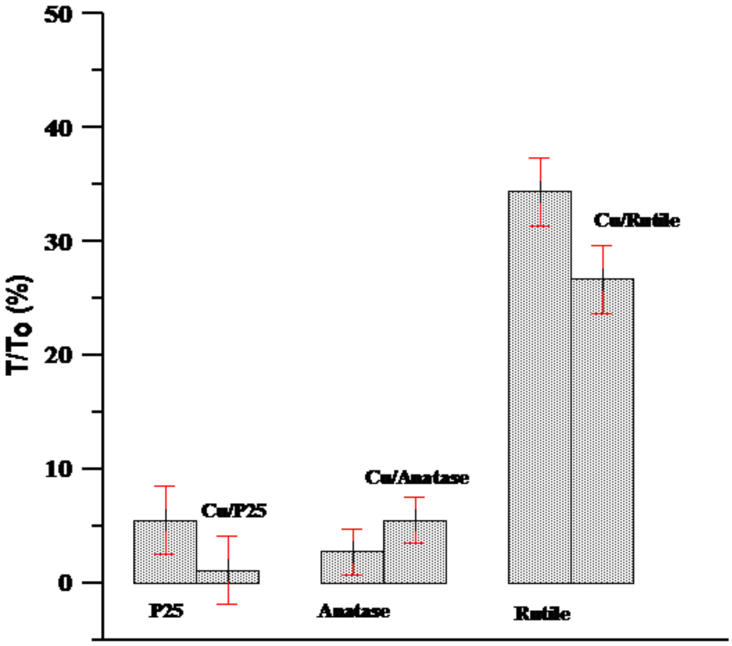

Figure 6.3: Radiant power transmitted by the aqueous suspension before the Cu(II) addition (pH ≈ 5) and after the Cu addition (pH ≈ 3.2). Wavelength range: 315-400 nm. TiO_2 load: 500 mg/l, Cu/TiO_2 ratio: 10% w/w. Hole scavenger agent: methanol or glycerol 10% v/v.

The mixtures containing undoped P25 (pH suspension ≈ 5.0) or Cu-doped P25 (pH suspension ≈ 3.2), showed the highest values of attenuation of the radiation transmitted (≈ 95%). Anatase containing suspensions exhibited a behavior similar to P25, in which anatase is the prevalent phase (anatase:rutile, ca 80:20). On the contrary, bare rutile suspensions were characterized by the smallest values of attenuation of radiant power transmitted (65%) with a small increase of the optical density for the Cu-doped rutile (73%). The pH of the aqueous suspension (5.0 and 3.2) seems to do not influence the optical properties of the investigated photocatalytic systems. The attenuation observed can be caused by light absorption and by physical processes of extinction of the particles such as scattering and reflection phenomena. The collected results matched with those previously reported in literature [142] according to which the specific absorption coefficient below wavelengths of 335 nm and the specific scattering coefficient for P25 are the largest among those estimated for different titanium dioxide particles.

6.2.3 Field emission scanning electron microscopy (FE-SEM)

The morphology, i.e. shape and size, of Cu-doped titania samples was investigated by FE-SEM (Figs. 6.4a-c). All the samples consisted of aggregated round-shaped nanoparticles. The crystallite sizes range between 50 – 110 nm for Cu/P25 and between 100 – 300 nm for Cu/anatase and Cu/rutile. The morphology of the photocatalysts did not change during the photocatalytic runs (data not shown).

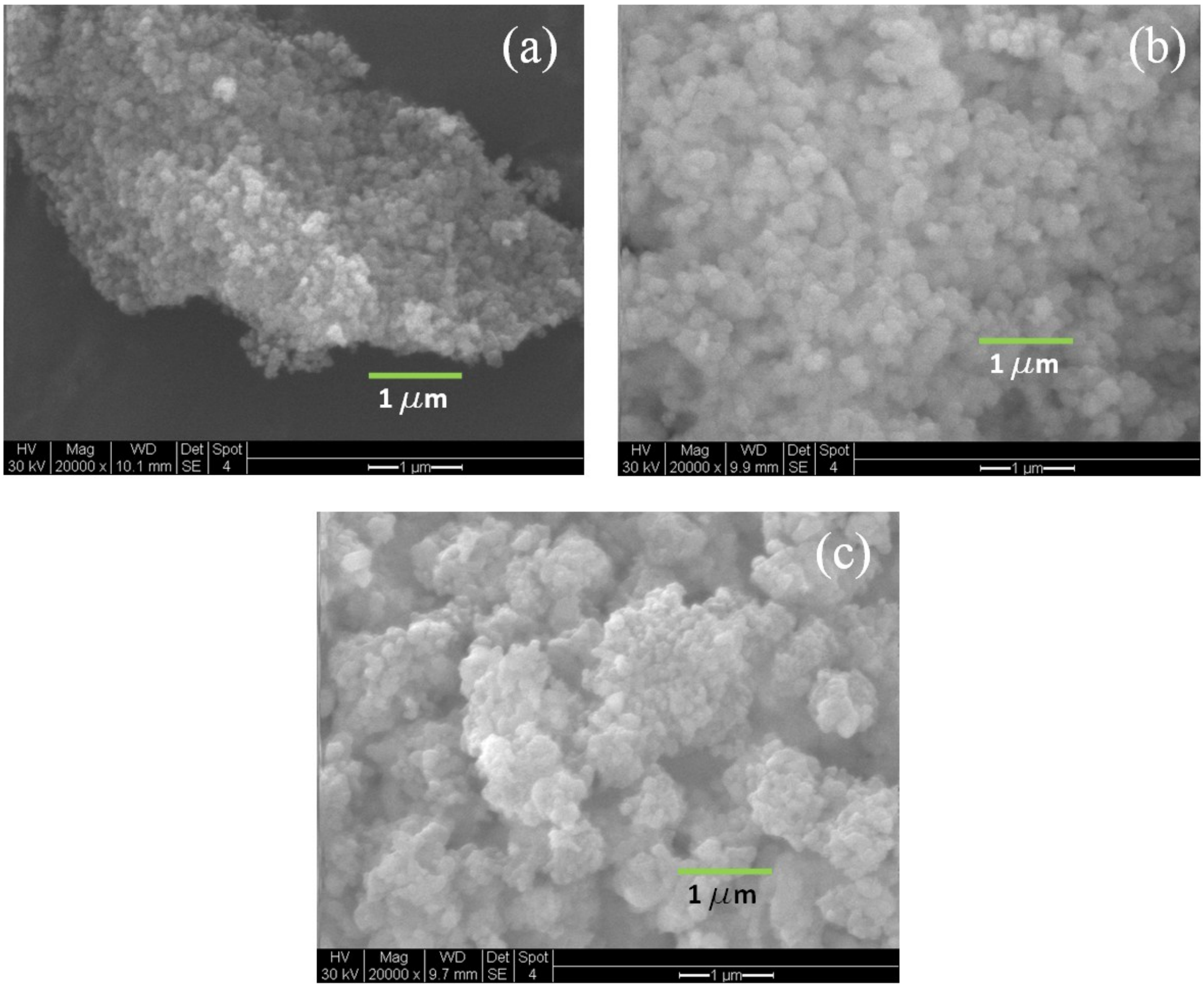

Figure 6.4: FE-SEM images of Cu/P25 (**a**), Cu/anatase (**b**), Cu/rutile (**c**).

6.2.4 Energy-dispersive X-ray spectroscopy (EDX)

The EDX analyses, performed on a selected area (2.4 mm x 2.2 mm) for the three different copper loaded photocatalysts (see Appendix, Fig. A2), shows peaks at 4.5 keV and 8.1 keV for titanium and copper and provides Cu/Ti ratios close to 10% by weight in all samples (% wt: 9.83, 10.53 and 11.4 for P25, anatase and rutile respectively), thus ensuring that they have similar Cu content.

6.2.5 High resolution transmission electron microscope (HR-TEM)

Figures 6.5a,b and 6.6 show HR-TEM images obtained for the copper doped commercial TiO_2. The images were taken at the same magnification to allow a direct comparison of the size distribution of titania and copper nanoparticles.

The presence of copper nanoparticles located at the edges of the TiO_2 particles, appearing as light grey spots in the HR-TEM images, was clearly evidenced in the photocatalysts. The average diameter of copper nanoparticles, estimated from HR-TEM analysis, was about 3.5 nm for Cu/P25 material and close to 10 nm for Cu/anatase and Cu/rutile samples.

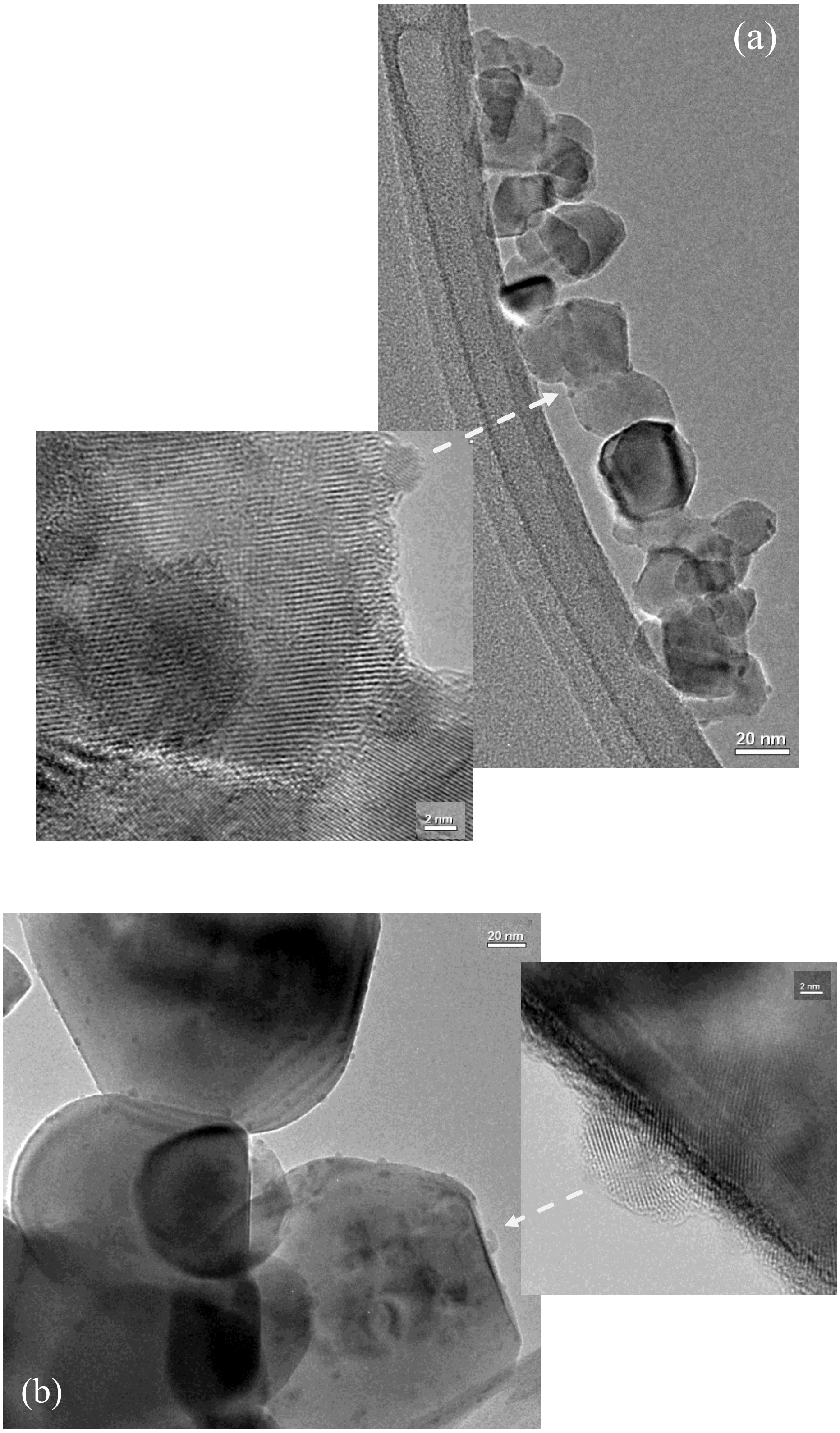

Figure 6.5: HR-TEM images of Cu/P25HR-TEM images of Cu/P25 (**a**), Cu/anatase (**b**).

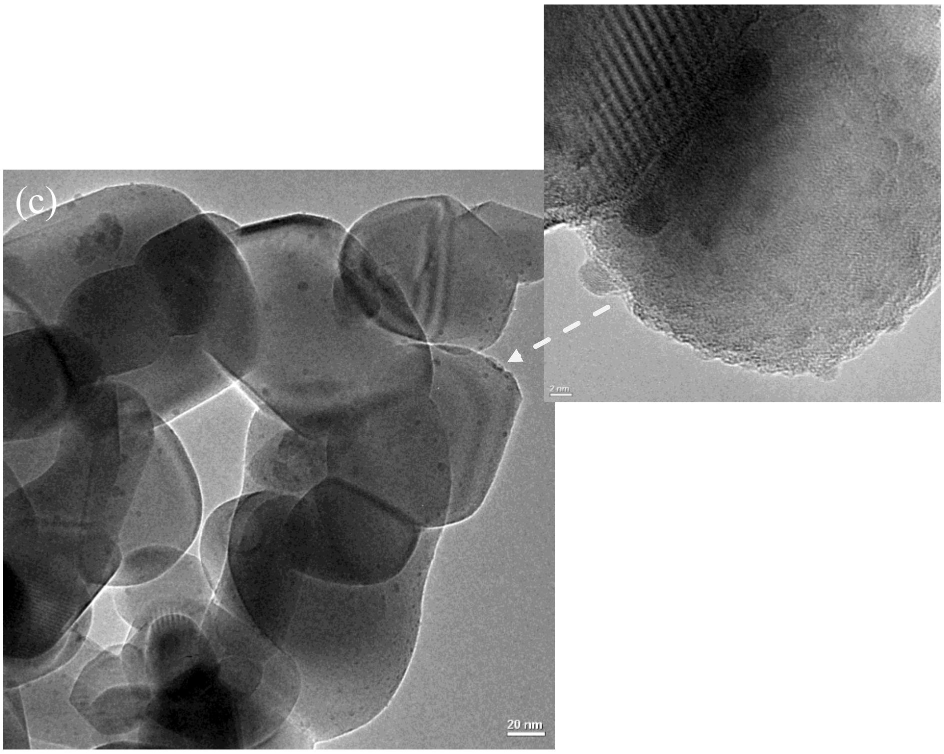

Figure 6.6: HR-TEM images of Cu/rutile.

6.2.6 Dynamic light scattering (DLS)

It is known that the particle sizes of photocatalytic materials affect the optical behavior of the mixture and consequently the radiant field inside the photoreactor and the photocatalytic efficiency of the process [143]. For this reason, DLS analysis was used to characterize the particle agglomerates size in the aqueous mixture containing different titania powders. The "in situ" distribution of the size as a function of the intensity is reported in Figure 6.7.

It is noteworthy to stress that the DLS analysis was carried out on bare titania only (not Cu/TiO_2) because the device cannot work under inert atmosphere in order to avoid the fast reoxidation of Cu-species reduced.

The hydrodynamic diameters of aggregates were 2.4 μm, 2.7 μm and 0.53 μm for bare P25, rutile and anatase respectively, thus indicating that, at pH = 5.5, P25 and pure rutile formed larger aggregates sizes which were of the same order of magnitude. The value collected for P25 sample was in perfect agreement with that reported by others [135] but it was quite different from that one (0.7 μm) reported by Cabrera *et al* [142]. However, it should be noted that in the latter case the samples were dried at 150 °C for 12 hrs and successively dispersed and sonicated in water for 1 hour before DLS measurement. On the other hand, the hydrodynamic sizes estimated in the present investigation were partially in accordance with those measured for the same bare TiO_2 but at a different pH (3.0) through electrophoretic light scattering spectrophotometry [144]. In particular, values of 0.473 μm, 0.467 μm and 1.18 μm were estimated for P25, anatase and rutile respectively.

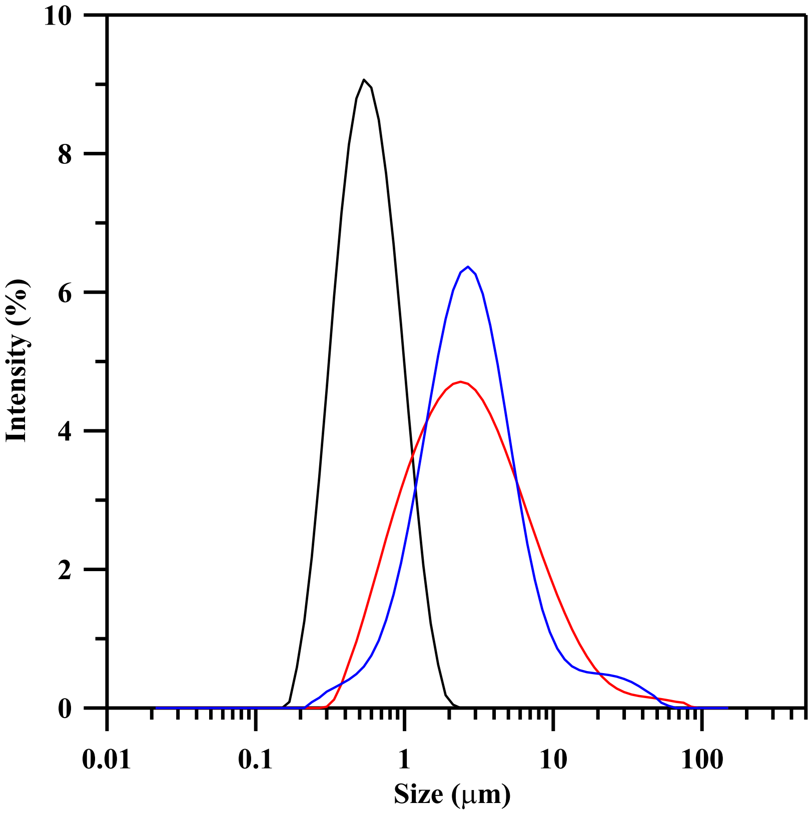

Figure 6.7: Laser granulometric analysis for bare TiO_2 at pH ≈ 5.0. anatase (black line), rutile (blue line); P25 (red line).

6.2.7 X-Ray Diffraction (XRD)

Figures 6.8a-c show XRD spectra for pristine and Cu-modified commercial TiO_2 nanostructures.

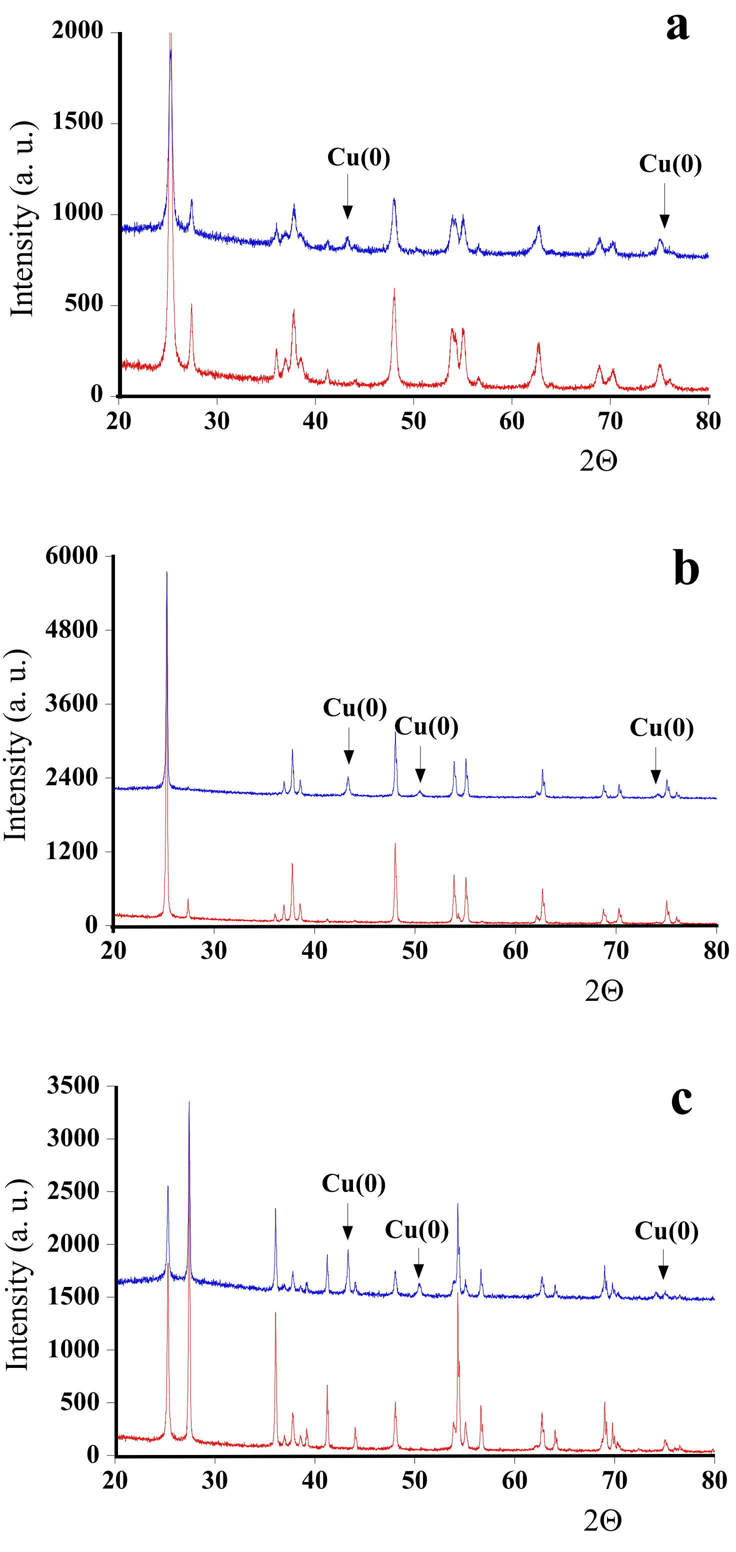

Figure 6.8: XRD patterns registered for bare (red) and Cu-loaded (blue) TiO_2: P25 (**a**), anatase (**b**) and rutile (**c**).

The XRD peaks corresponding to anatase and rutile phases were observed in the spectra of pristine powders as reported in Figures 6.8a-c, according to literature [178]. For pristine titania photocatalysts, the XRD peaks of P25 show lower intensity than anatase and rutile samples, indicating a lower crystalline grade for P25 with respect to anatase and rutile.

On the other hand, for the copper loaded photocatalysts (recuperated after the photocatalytic process), three peaks at 2Θ values of 43°3’, 50°5’ and 70° can be distinguished. As previously reported in Chapter 5, Section 5.3, these peaks exactly match those of zero-valent copper, whereas no peaks due to CuO and Cu_2O can be appreciated [130].

Also in this case, the crystallite size (D) of titania and zero-valent copper was calculated using XRD data and applying the Scherrer equation ($D = \frac{k\lambda}{\beta \cos \Theta}$), where k is a constant (0.94 for spherical particles), λ is the wavelength of the X-ray radiation (0.154 nm), β is the line width at half maximum intensity of the peak, and Θ is the angle of diffraction (21°6’). The average crystalline sizes of TiO_2 crystals were 9, 13 and 18 nm for P25, anatase and rutile samples respectively. Similar values were calculated in copper loaded photocatalysts. Also, the mean size of zero-valent copper nanoparticles formed in the first stage of the photocatalytic process, was close to 5 nm for P25, 10 nm for anatase and to 13 nm for rutile. Moreover, a decrease of relative intensities of peaks were observed related to the TiO_2 nature in the case of copper loaded titania. Cu/P25 presents a lower crystalline grade with respect to Cu/anatase and Cu/rutile materials.

6.2.8 Surface area determination

The BET surface area of the different TiO_2 and Cu/TiO_2 particles are reported in Table 6.1. For bare TiO_2 samples, the BET data are in agreement with the literature [145,146]. A small increase is observed in the case of rutile, while no significant changes were observed for P25 and anatase after zero-valent copper deposition.

6.2.9 FT-IR and Thermogravimetric (TG) analyses

FT-IR and TG results on the pristine TiO_2 samples are shown in Figures 6.9. FT-IR spectra (Figure 6.9a) show the typical OH band at 3350 cm^{-1} for all the three TiO_2 samples. The signal is more evident in the FT-IR spectrum of P25 material. Furthermore, TG curve of P25 (Figure 6.9b) shows a more pronounced weight loss, starting from 200°C, that results from chemically bound water (OH groups) [147]. These results clearly confirm that P25 presents a higher number of surface hydroxyl groups for catalyst mass with respect to anatase and rutile. A determination of hydroxyl surface density (OH/nm^2), was carried out through TG measurements, including an isothermal heating at 120 °C for 20 min, required to remove physically adsorbed water. The OH/nm^2 values for P25, anatase and rutile, reported in Table 6.1, were calculated based on the weight loss from 120 °C to 500 °C detected by following Eq. 6.1 [137]:

$$\# \frac{OH}{nm^2} = \alpha \frac{\left(\# \frac{OH}{nm^2}\right)_{T_2} \times SSA \times wt_{T_2} + \frac{(wt_{T_1} - wt_{T_2})}{\frac{MW_{H_2O}}{N_A}} \times 2}{SSA \times wt_{T_1}} \qquad \text{Eq. 6.1}$$

where wt_{T_1} is the sample weight at the corresponding temperature T_i, (120 °C), MW_{H_2O} the molecular weight of water, N_A Avogadro's constant, *SSA* the specific surface area and α is a calibration factor (equal to 0.625). For each bare TiO_2 sample (P25, anatase, rutile), it is assumed that at T_2= 500 °C the powder surface is free of OH surface groups; therefore, OH surface density (#OH/nm^2) at that temperature was neglected in Eq. 6.1 [137].

For Cu-modified samples, the FT-IR and TG spectra appear not quantitatively reliable, due to the presence of some organic traces of the sacrificial agent on the catalysts surface.

	P25	Cu/P25	Anatase	Cu/anatase	Rutile	Cu/rutile
S_{BET} (m^2/g)	50.1	48.5	9.5	12.2	21.6	18.9
HO surface density (OH/nm^2)	8.0	--	4.4	--	9.1	--

Table 6.1: Surface properties of pristine and Cu-modified TiO_2 photocatalysts.

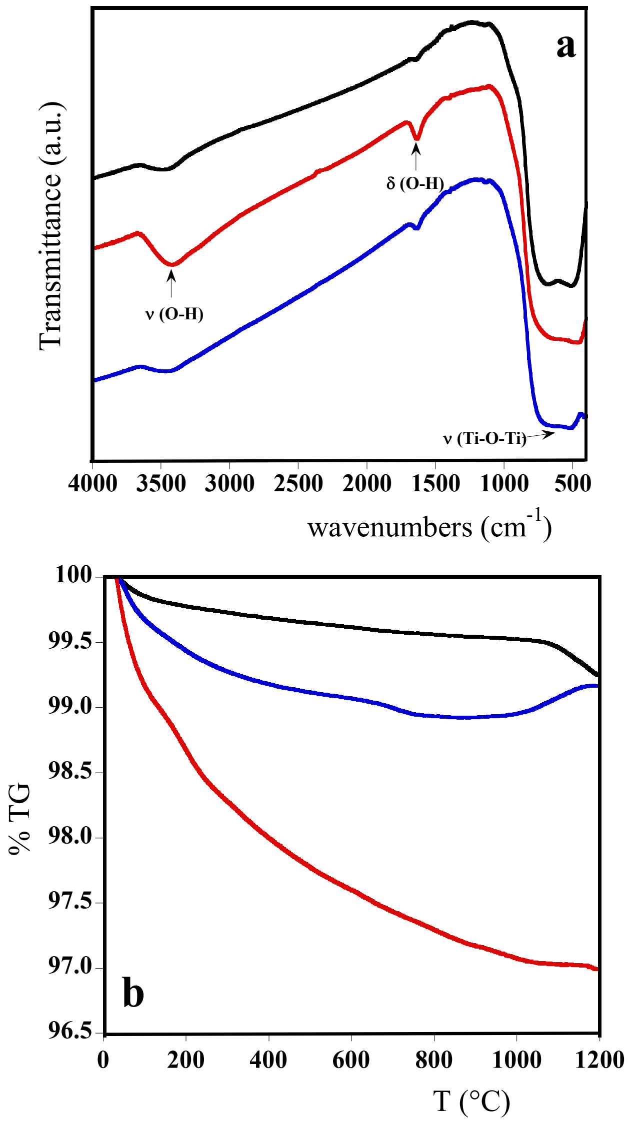

Figure 6.9: FT-IR (**a**) and TG (**b**) spectra registered for bare P25 (blue line), anatase (black line) and rutile (red line).

6.2.10 Diffuse-Reflectance UV (DRUV) spectroscopy

DRUV spectra are shown in Figure 6.10a. The measured intensity was expressed as the value of the Kubelka–Munk function F(R). The energy gap values were calculated by linearization of the plot of $(F(R)h\nu)^{1/2}$ against photon energy, as reported in Figure 6.10b for bare TiO_2 and in Figure 6.10c for copper-doped TiO_2. For the bare TiO_2 powders, the evaluated optical band gap is in the range 3.0-3.2 eV for the transition from the valence band (VB) to the conduction band (CB), in agreement with literature values [115,148].

Figure 6.10a indicates that Cu-doped TiO_2 photocatalysts are much less optically transparent than the bare TiO_2 ones in the visible range ($\lambda > 400$ nm). This effect is probably due to scattering phenomena and to local surface plasmon resonance of copper nanoparticles deposited on the surface of TiO_2, also associated to a decrease in the optical band-gap values (Fig. 6.10c). These data clarify that in the first stage of the process, during which Cu-modified TiO_2 is formed, the light absorption behavior of the solid suspended in the reactor drastically changes, assuming a relevant character in the visible range.

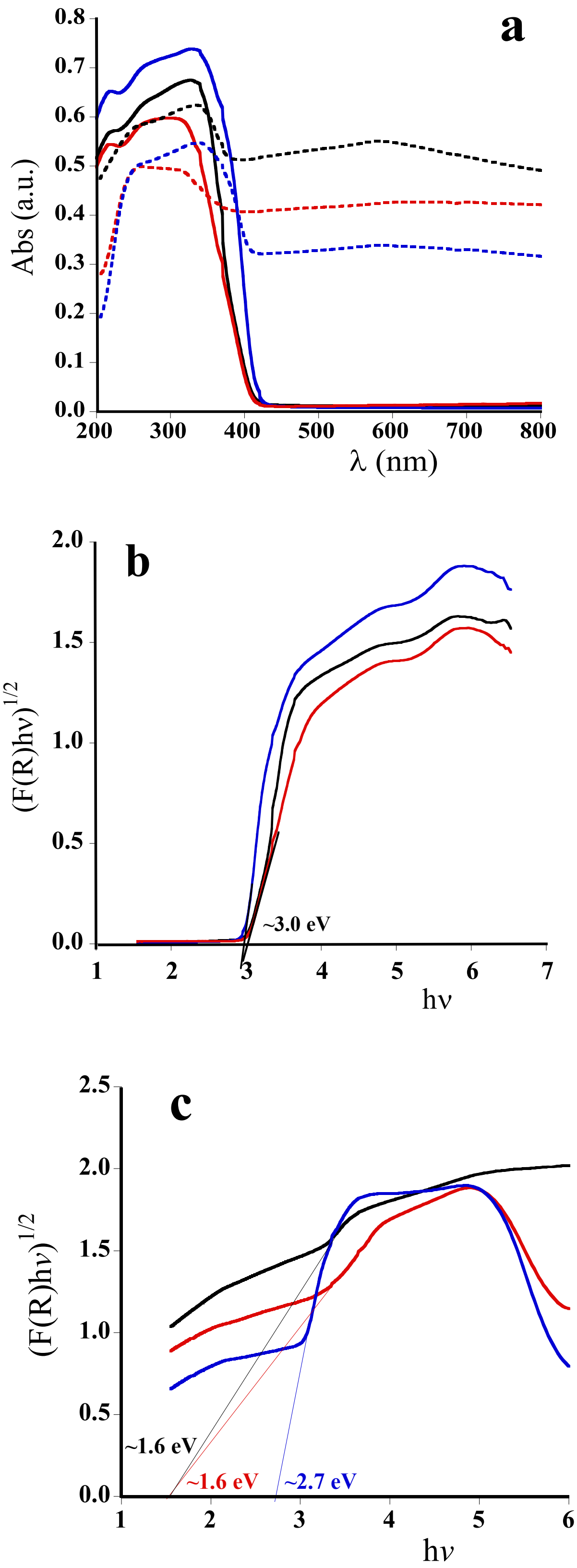

Figure 6.10: Diffuse Reflectance UV (DRUV) spectra (**a**) for bare (continuous curves) and Cu-modified (dashed curves) TiO_2 catalysts: anatase (black line), rutile (blue line) and P25 (red line).Plots of $(F(R)h\nu)^{1/2}$ versus photon energy for bare TiO_2 samples (**b**) and Cu/TiO_2 samples (**c**).

6.2.11 Photoluminescence

Photoluminescence (PL) spectroscopy was conducted to probe the radiative recombination efficiency of photogenerated charges in the TiO_2 nanoparticles and to evidence their eventual changes caused by the Cu doping. PL spectra acquired for bare commercial TiO_2 acquired in inert environment (dry N_2) are reported in Figure 6.11. As the PL intensity of TiO_2 strongly depends on the presence of oxygen adsorbates [149,150], all the spectra were acquired after stabilizing the PL intensity level by flowing N_2 in the test chamber for 30 minutes. The same integration time (10 s) was used for the three spectra.

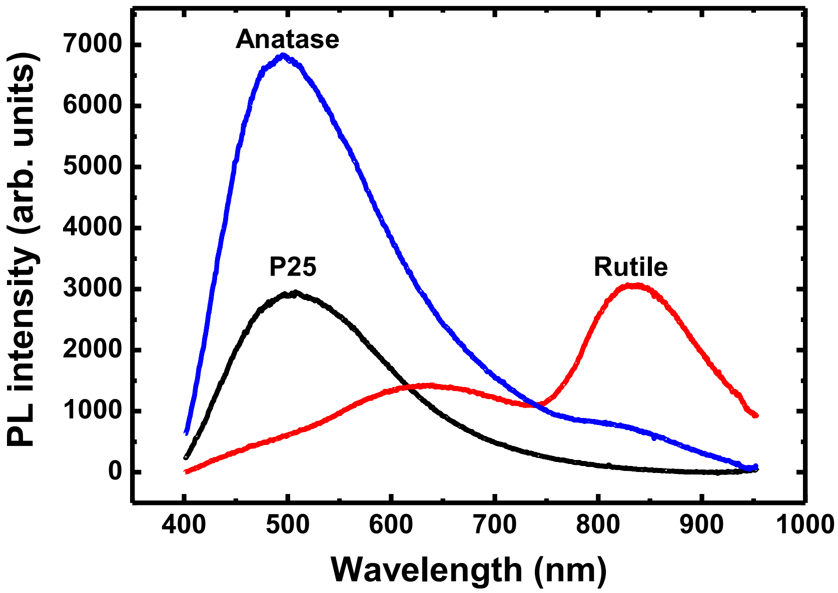

Figure 6.11: PL intensity spectra of the commercial TiO_2 samples under dry nitrogen atmosphere.

The well-known difference [150] in the PL spectra of the three polymorphs of TiO_2 is clearly evidenced in the experimental data. In fact, it is observed that the PL of rutile TiO_2 is peaked in the near infrared region, whereas P25 and anatase exhibit the same PL spectra (VIS) peaked at about 500 nm. Near-infrared rutile PL and visible anatase PL originate from different emission mechanisms and exhibit different quantum efficiencies. Hence a direct comparison between their intensities is little informative. Instead, the difference in PL intensity of P25 (black curve) and anatase (blue curve) is more significant. As observed in

Figure 6.11, P25 nanoparticles show a visible PL intensity less (by a factor of about 2.5) than the anatase nanoparticles one.

The PL spectra of Cu-doped TiO_2 samples are reported in Figures 6.12a-c. It is found that the presence of Cu does not modify the PL shape (i.e. the PL emission still originates from TiO_2), but leads to a significant quenching of the PL intensity. This effect is extremely relevant in the case of Cu/P25 as can be seen in Figure 6.12a, where the PL intensities are reported in log scale to evidence the extent of PL suppression induced by sample modification. The same effect is also relevant for anatase, even if to a lesser extent, and present in rutile.

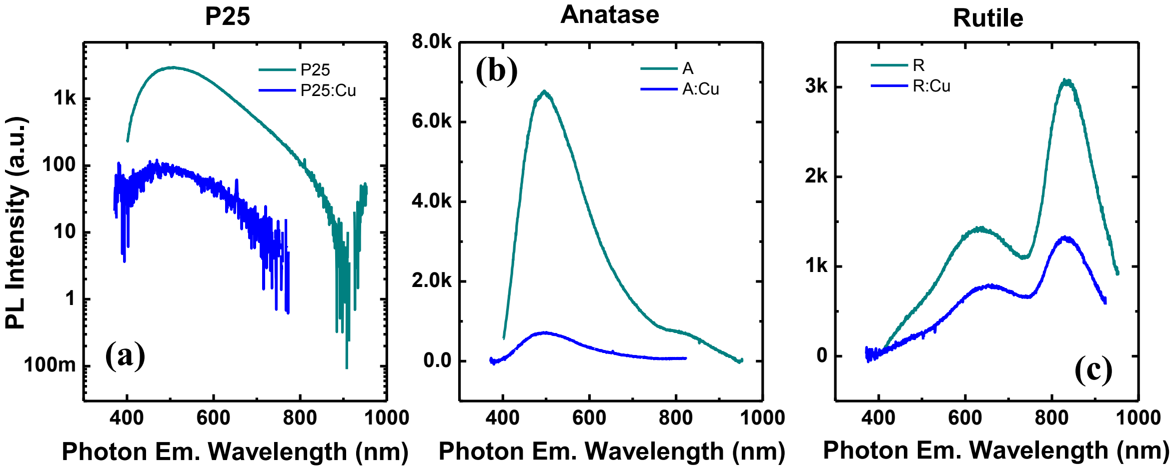

Figure 6.12: PL spectra of bare TiO_2 and Cu-doped TiO_2 photocatalysts, measured in dry nitrogen. (a): Bare P25 (grey curve) and Cu-doped P25 (blue curve). Notice the logarithmic scale. **(b)**: Bare anatase TiO_2 (grey curve) and Cu-doped anatase (blue curve). (c): Bare rutile TiO_2 (grey curve) and Cu-doped rutile (blue curve).

6.3 Discussion

The results reported in Figure 6.1 indicate that the photocatalytic efficiencies for hydrogen production significantly depend upon the crystal phase of the used TiO_2 particles. The largest production yield was measured for P25, whereas similar rates were observed for bare anatase and rutile. The same trend is observed after the Cu doping. As we discuss in the present section, different physical-chemical properties can be invoked to explain such differences, including electron-hole pairs recombination, surface/bulk defects, titanium dioxide and zero-valent copper particles size, TiO_2 specific surface area, hydroxyl surface density, and copper distribution on TiO_2 surfaces.

6.3.1 Undoped TiO_2 photocatalysts

The pristine titania materials showed poor photoactivity for hydrogen generation, although the activity of P25 is relatively higher than anatase and rutile. The low hydrogen productivity recorded for all bare titania is ascribable to fast electron/hole pair recombination. As regards the different reactivity of undoped materials, it is worth to observe that several investigations indicate P25 titania as more reactive than anatase and rutile alone [151-154].

The higher photocatalytic activity of P25, which consists of anatase and rutile crystallites, is mainly ascribed to a synergistic effect between the two crystalline phases [152]. More to the point, free charge carriers can spontaneously migrate from one phase to another, forming local built-in electric field in the transition region at the boundary between anatase and rutile crystallites that may enhance charge separation, hampering the mutual recombination between the mobile photogenerated charge carriers, increasing their lifetime and thus improving their reactivity towards chemicals [155].

The visible PL emission peaked at about 500 nm has been attributed to radiative recombination of free (conduction band) electrons with localized holes, trapped at O vacancy sites (F-centers) or Ti^{3+} sites adjacent to surface bridging O atoms [156,157]. Hence, this PL emission is supposed to depend on the spatial overlap between the quantum wave functions associated to free electrons and the involved defects (trapped holes). The analysis reported in Figs. 6.12 revealed that the intensity of this PL emission is lower for P25 sample, compared to the anatase sample. This suggests the occurrence of improved charge separation in P25, possibly caused by the above-mentioned charge transfer at anatase/rutile junctions. The absence of the near-infrared emission of rutile - ascribed to the recombination of trapped electrons and free holes [150] - in PL spectra of P25 may reveal electron transfer between the two phase, although controversial opinions on the direction of electron flow (rutile-to-anatase or *vice versa*) are reported in the literature review [155,158-161].

Specific surface area, particle size, crystal composition, and surface hydroxyl density also can be accounted for the higher photocatalytic activity of P25. The specific surface area correlates with the number of external chemicals that can be brought in contact with a given mass of photocatalyst, and thus correlates with the yield of a photocatalytic transformation.

The BET analyses (Table 6.1) indicated higher specific surface area for P25 catalyst with respect to anatase and rutile materials, thus accounting its larger efficiency in hydrogen production.

Concerning particle size, and FE-SEM (Fig. 6.5a,b and Fig. 6.6) indicated smaller mean size of TiO_2 particles for P25 with respect to anatase and rutile materials. It is known that for smaller sized particles, separation and transport of photo-generated charge carriers to the surface of titania are noticeably favored [162]. On the contrary, for larger sized titania particles, a higher likelihood of charge carriers trapping by bulk defects with consequent inhibition photocatalytic surface reactions occur.

The aggregation behavior of the dispersion of titania particles could also affect system reactivity. Figures 6.3 and 6.7 indicate that both P25 and rutile form aggregates of particles when suspended in water. These aggregates have similar size distributions, although they show different optical properties in terms of transmitted photon flux for the wavelength range of 315 - 400 nm. On the other hand, aqueous suspensions containing P25 or anatase exhibit similar transmittance values but different values of average hydrodynamic diameter of aggregates, that for anatase is one order of magnitude smaller than P25. The results indicate that the optical behavior of the investigated photocatalytic systems is very complex and cannot be directly related to the particle agglomerate sizes. Moreover, based on the results reported in Figure 6.1, it can be stated that neither the size of particle aggregates nor the macroscopic optical properties of the mixtures are related to the differences in the photocatalytic activity recorded for the investigated materials.

As regards hydroxyl surface density of titania photocatalysts, it is reported [163,164] that an increase in surface hydroxyl concentration is directly correlated to an increase in surface defects, such as surface oxygen vacancies and Ti^{3+} centers. Such surface defects can affect the separation of photogenerated charge carriers on the TiO_2 surface under UV irradiation, and therefore the activity of the material [165,166]. In particular, photogenerated holes can be trapped by hydroxyl groups generating surface defects with low electron density (oxygen vacancies), which react with the sacrificial agent (i.e, methanol or glycerol). On the other hand, photogenerated electrons can be trapped by Ti^{4+} sites leading to Ti^{3+} centers, which can reduce hydronium ion to proton. Protons combine with electrons to generate hydrogen gas.

Experimental results reported in the present work (FT-IR specta and TG curves) have confirmed a lower number of surface OH groups for catalyst mass in undoped anatase and rutile powders with respect to undoped P25, thus attesting the presence of a minor number of bulk/surface defects although such data do not match the higher catalytic activity of anatase compared to rutile (Table 6.1).

6.3.2 Copper-doped TiO_2 photocatalysts

As thoroughly motivated in Chapter 5, the recombination of photogenerated electrons and holes on the TiO_2 surface is strongly suppressed by the presence of metal-copper particles. This is confirmed by the low PL intensity of Cu/TiO_2 samples with respect to bare TiO_2 samples (Figs. 6.12a-c).

However, as reported in Figure 6.1, copper modified P25 photocatalyst exhibits an activity in terms of hydrogen production rate far higher than copper-modified anatase and rutile materials. The photoactivity difference could be related to several morphological/chemical/electronic properties of doped titania, such as (*i*) the different hydroxyl group density per unit mass of catalyst, (*ii*) the different size of titania particles and metal copper deposits, and (*iii*) the existence of the homojunction region in P25.

As discussed above, FT-IR and TG analyses (Figs. 6.9a,b) indicated a higher density of hydroxyl groups per unit weight of catalyst for P25 than anatase and rutile. These values, which were inferred from the data reported in Table 6.1, were 400, 42, and 148 ($10^9 \cdot$OH/ng of TiO_2) for P25, anatase, and rutile, respectively.

According to the literature findings, oxygen vacancies act as active sites for water dissociation, in the sense that water is adsorbed dissociatively in oxygen vacancies and via proton transfer to a neighbor bridging oxygen site thus generating hydroxyl groups on TiO_2 surface [167]. Therefore, the presence of a higher amount of hydroxyl groups on P25 surface, as shown by thermogravimentic and FT-IR results (Fig. 6.9), is an evidence of a higher number of oxygen vacancies of P25 material than anatase and rutile. Both experimental data and theoretical calculations show that metals are preferentially deposited over oxygen vacancies that act as nucleating centers on the TiO_2 surface [168].

The amount of hydroxyl groups on the photocatalyst surface can also affect the deposition of zero-valent copper particles during the photocatalytic process, with a impact on H_2-production activity of the modified photocatalyst.

In fact, hydroxyl groups can promote the physical adsorption on the photocatalyst surface of solvated cupric ions, which are readily reduced to zero-valent copper ions by reaction with surface photoelectrons [60,107,169].

As a consequence, it can be expected that the distribution of Cu nanoparticles should be more uniform in P25 than anatase and rutile due to the larger number of surface hydroxyl groups characterizing the P25 surface. On the contrary, the lower hydroxyl groups concentration calculated for anatase and rutile is expected to disfavor the uniform photodeposition of zero-valent copper particles and affects the size of metal copper deposits on the photocatalyst surface.

In addition, the occurrence of the homojunction region and the smaller primary size of particles for P25 than anatase and rutile samples increases the lifetime of free charge carriers, thus enhancing the concentration of photogenerated electrons on the surface of P25 during the photodeposition of copper. The higher electron surface density determine a more uniform photodeposition of zero-valent copper. Summarizing, the intrinsic P25 characteristic (i.e., charge separation and increased surface HO group density) are expected to both lead to a more uniform distribution of Cu nanoparticles scattered on a large portion of TiO_2 surface. Since copper content for the three photocatalysts is similar, a decrease in nanoparticle size of metal deposited on P25 to anatase and rutile should be expected. This prediction is indeed confirmed by XRD (Fig. 6.8) and HR-TEM (Fig. 6.6) analyses. Smaller Cu nanoparticles, results in an increased contact surface per unit volume of titania, thus increasing the probability of having effective traps for the photoelectrons [170-173].

The broader distribution of small Cu nanoparticles on vast portions of TiO_2 surfaces in P25 samples compared to rutile/anatase samples allows explaining the huge differences in PL emission measured for pure P25 versus the Cu-P25 samples (Fig. 6.12a).

In fact, the quenching associated to Cu presence, observed in all Cu-doped samples (See Figs. 6.12a-c) can be assigned to the reduced radiative recombination caused by charge transfer and the consequent electron depletion in TiO_2 close to the Cu boundary. As shown in Fig. 6.12a, the quenching is particularly remarkable for Cu-P25 samples. Our interpretation is that in this case, thanks to the largest Cu/TiO_2 surface contact and to the smaller size of both TiO_2 and Cu nanoparticles, the electron depletion affects fractions of TiO_2 nanoparticles volume greater than those depleted by Cu/anatase and Cu/rutile contact, strongly inhibiting the PL activity of TiO_2.

Instead, for larger nanoparticles of titania (Cu/anatase and Cu/rutile), photogenerated carriers can be formed far from the Cu/TiO_2 interface. In this case, the lifetime of photogenerated electrons, located in the bulk of TiO_2 and far from the boundary with Cu deposits, is not expected to be significantly affected by copper nanoparticles. Thus, the PL intensity of larger nanoparticles will be less affected by metal particles on the TiO_2 surface or, in other words, the Cu/TiO_2 interface-related PL quenching is stronger for P25 than anatase and rutile.

Concluding, both the improved photocatalytic activity of the Cu-P25 catalysts and the PL quenching can be traced back to the intrinsic characteristics of Cu deposition.

The difference in hydrogen production rate observed in presence of Cu/P25 when varying the nature of the alcohol (i.e., methanol, glycerol) is related to the higher (*i*) number of hydroxyl groups of the alcohol and (*ii*) number of hydrogen atoms in the α-position to the alcoholic group, (*iii*) polarity and (*iv*) hole scavenging ability of glycerol compared to methanol [154].

The small different activity between Cu/anatase and Cu/rutile may be ascribed to several factors, such as surface/bulk defects ratio, crystalline/amorphous phase ratio, type of the exposed facets of rutile and anatase samples [165], and nature of sacrificial agent [154]. Overall, Table 6.2 reports a list of features related to the best photoefficiency for H_2 generation shown by P25-based samples.

Undoped and copper-doped P25		
Properties	**Effect**	**Proof**
Homojunction at the rutile/anatase interphase	Reduction of e^-/h^+ pair recombination	Literature findings, PL analyses
Higher density of OH groups per unit weight of catalyst	Reduction of e^-/h^+ pair recombination, promotion of Cu^{2+} adsorption on the catalyst surface, more uniform distribution and smaller size of metal copper particles over the surface	Literature findings, HR-TEM, FT-IR and TG analyses
Smaller size of P25 particles and zero-valent copper deposits	Reduction of e^-/h^+ pair recombination, higher specific surface density	Literature findings, BET, PL, FE-SEM, HR-TEM and XRD analyses

Table 6.2: Summary of the electronic and morphological properties of undoped and copper doped P25.

6.4 Summary

The photoactivity for hydrogen generation of undoped commercial TiO_2 photocatalysts and zero-valent copper doped TiO_2 using methanol or glycerol as sacrificial species under UVA radiation was studied. Experimental results indicate that the polymorphic composition of the titania adopted has a marked influence on the photoactivity for both the groups of materials. The photocatalytic activity of undoped and copper-doped materials had the following order: P25 $\gg$ bare anatase $\cong$ bare rutile, which can be explained in terms of (*i*) relative photogenerated charge carrier concentration on the surface, (ii) titania and metal copper nanoparticles sizes, and (iii) amount of superficial hydroxyl groups. For undoped commercial materials, the higher photoreactivity of P25 TiO_2 compared to that of anatase and rutile is ascribed to a synergistic effect between the two crystallographic phases (anatase and rutile) forming a homojunction region, which reduces the natural tendency of charge carriers to recombine.

The introduction of zero-valent copper in these materials allows electron transfer from the TiO_2 conduction band to the metal, thus further reducing charge carriers recombination and promoting the photoreactivity. The best results related to the introduction of copper were observed in the case of P25, as in this case a more efficient use of the copper on the photocatalyst surface occurs. This may be explained by considering that the presence of hydroxyl groups affects copper distribution on the catalyst surface. The highest value of hydroxyl group concentration per unit mass was found in P25, whose HR-TEM images indicate a more uniform distribution of zero-valent copper than anatase and rutile.

7. Results III

Kinetic modeling of H_2 generation over nano-Cu/TiO_2 catalyst through photoreforming of alcohols

7.1 Introduction

In Chapter 5, hydrogen generation from different oxygenated compounds by adopting a nanocopper modified-TiO_2-P25 catalyst prepared by "in situ" deposition process was investigated. The best results were observed for organic species strongly adsorbed on the catalyst surface such as methanol, glycerol, and formic acid.

The development of a suitable mathematical model capable of simulating hydrogen production over the same catalyst (nano-$Cu_{(s)}/TiO_2$) when glycerol or methanol were adopted as sacrificial agents is herein presented.

7.2 Kinetic model

A simplified network of reactions was singled out by considering that, upon irradiation of $Cu_{(s)}/TiO_2$ catalyst nanoparticles, a couple of charge carriers is generated ($r_{7.1}$):

$$Cu_{(s)}/TiO_2 \xrightarrow{h\nu} e^- + h^+ \qquad (r_{7.1}) \qquad \text{reaction rate: } G = \frac{\Phi_{UV}}{V} I_{a,UV} + \frac{\Phi_{VIS}}{V} I_{a,VIS}$$

The rate of reaction $r_{7.1}$, which is a photochemical step, was accounted for by the products between quantum yields, in both the UVA (Φ_{UV}) and the visible range (Φ_{VIS}), and respective radiation powers absorbed by the catalyst suspension ($I_{a,UV}, I_{a,VIS}$) divided by the volume of irradiated solution (V = 0.280 L).

Charge carriers may recombine through radiative or non-radiative processes ($r_{7.2}$):

$$e^- + h^+ \xrightarrow{k_r} heat\ and\ light \qquad (r_{7.2}) \qquad \text{reaction rate: } k_r[h^+]\cdot[e^-]$$

As reported by others [127], reaction $r_{7.2}$ is regulated by a second-order kinetic law in which k_r is the electron/hole recombination reaction constant.

Otherwise, charge carriers can be scavenged. In particular, photogenerated holes can also react with the adsorbed sacrificial organic compound (S^*), which successively oxidizes on the catalyst surface ($r_{7.4}$–$r_{7.5}$), where reaction $r_{7.4}$ is the rate-determining step for substrate oxidation:

$$S + \therefore^* \rightleftarrows S^* \qquad (r_{7.3}) \qquad [S^*] = \frac{C_T \cdot K_{ads} \cdot [S]}{(1 + K_{ads} \cdot [S])}$$

$$S^* + h^+ \xrightarrow{k_{h^+}} S^{\bullet *} + H^+ \qquad (r_{7.4}) \qquad \text{reaction rate: } k_{h^+}[h^+][S^*]$$

$$S^{\bullet *} + H^+ \xrightarrow{h^+/fast} \therefore^* + S_{ox} + 2H^+ \qquad (r_{7.5})$$

As previously proposed [128], the direct reaction between positive holes and organic substrates is only possible if organics are strongly adsorbed on the catalyst surface. The adsorbed species concentration $[S^*]$ may be obtained by a Langmuir-type model for adsorption, as reported for the equilibrium $r_{6.3}$ in which K_{ads} (M^{-1}) is the adsorption equilibrium constant, and C_T (M) is the total concentration of active sites on the catalyst surface for a fixed catalyst load q ($g \cdot L^{-1}$). The term C_T was calculated through the formula $C_T = q \cdot N$, where N is the total moles of active sites per unit mass of catalyst ($mol \cdot g^{-1}$). Photogenerated electrons react with protons ($r_{7.6}$) arising from the organic oxidation ($r_{7.4}$–$r_{7.5}$):

$$H^+ + e^- \xrightarrow{fast} H^\bullet \xrightarrow{H^\bullet\ /fast} H_2 \qquad (r_{7.6})$$

In this regard, some literature indications [129] report that hydrogen molecules are formed from the reduction of protons adsorbed on the solid surface, without clear details on the kinetics governing reaction $r_{7.6}$. In the present work it was assumed that protons, arising from the organic oxidation on the catalyst surface ($r_{7.4}$), immediately reduce and form hydrogen gas ($r_{7.6}$).

On the basis of assumptions reported above, a mathematical model was developed based on a set of mass balance equations for the main species involved in the process ($eq_1 - eq_7$):

$$\frac{d[S]}{dt} = -k_{h^+}[S^*][h^+] \qquad eq_1$$

$$\frac{d[h^+]}{dt} = G - k_r[h^+][e^-] - 2k_{h^+}[S^*][h^+] \qquad eq_2$$

$$\frac{d[e^-]}{dt} = G - k_r[h^+][e^-] - 2k_{h^+}[S^*][h^+] \qquad eq_3$$

$$\frac{d[H_2]}{dt} = k_{h^+}[S^*][h^+] \qquad eq_4$$

where

$$G = G_{UV} + G_{VIS} \qquad eq_5$$

$$G_{UV} = \frac{\Phi_{UV}}{V} I_{a,UV} = \frac{\Phi_{UV}}{V} \sum_i I^0_{\lambda_i} \left(1 - e^{(-2.3 \cdot \mu \cdot \varepsilon_{UV} \cdot [TiO_2])}\right) \qquad eq_6$$

$$G_{VIS} = \frac{\Phi_{VIS}}{V} I_{a,VIS} = \frac{\Phi_{VIS}}{V} \sum_i I^0_{\lambda_i} \left(1 - \mathrm{e}^{(-2.3 \cdot \mu \cdot \varepsilon_{VIS} \cdot [TiO_2])}\right) \qquad eq_7$$

The terms $I^0_{\lambda_i}$, ε_{VIS}, ε_{UV} and μ are the power emitted by the lamp (see Chapter 4), the extinction coefficients of the photocatalyst in visible and UVA wavelengths (measured parameters), and the light-path length (1.10 cm) respectively.

The equations ($eq_1 - eq_7$) must be numerically integrated from the following initial conditions:

$$[S]_{t=0} = S_0,\ [h^+]_{t=0} = 0,\ [e^-]_{t=0} = 0, \text{ and } [H_2]_{t=0} = 0$$

in order to calculate the concentration of each species *versus* time, provided that a suitable value is available for each parameter included in the model proposed.

7.3 Results and discussion

Figures 7.1a,b show the results of two typical photorefoming runs on glycerol and methanol over bare TiO_2-P25 and $Cu_{(s)}/TiO_2$-P25 nanomaterial, respectively. These figures indicate a sharp increase in hydrogen generation rate during the deposition of metal copper on the semiconductor surface, followed by a lower-reactivity steady state. For all photocatalytic runs, after reaching steady state, the lamp was switched-off and shortly after switched-on again. The new switch-on time was assumed to be the zero-time to collect data for modeling (orange box).

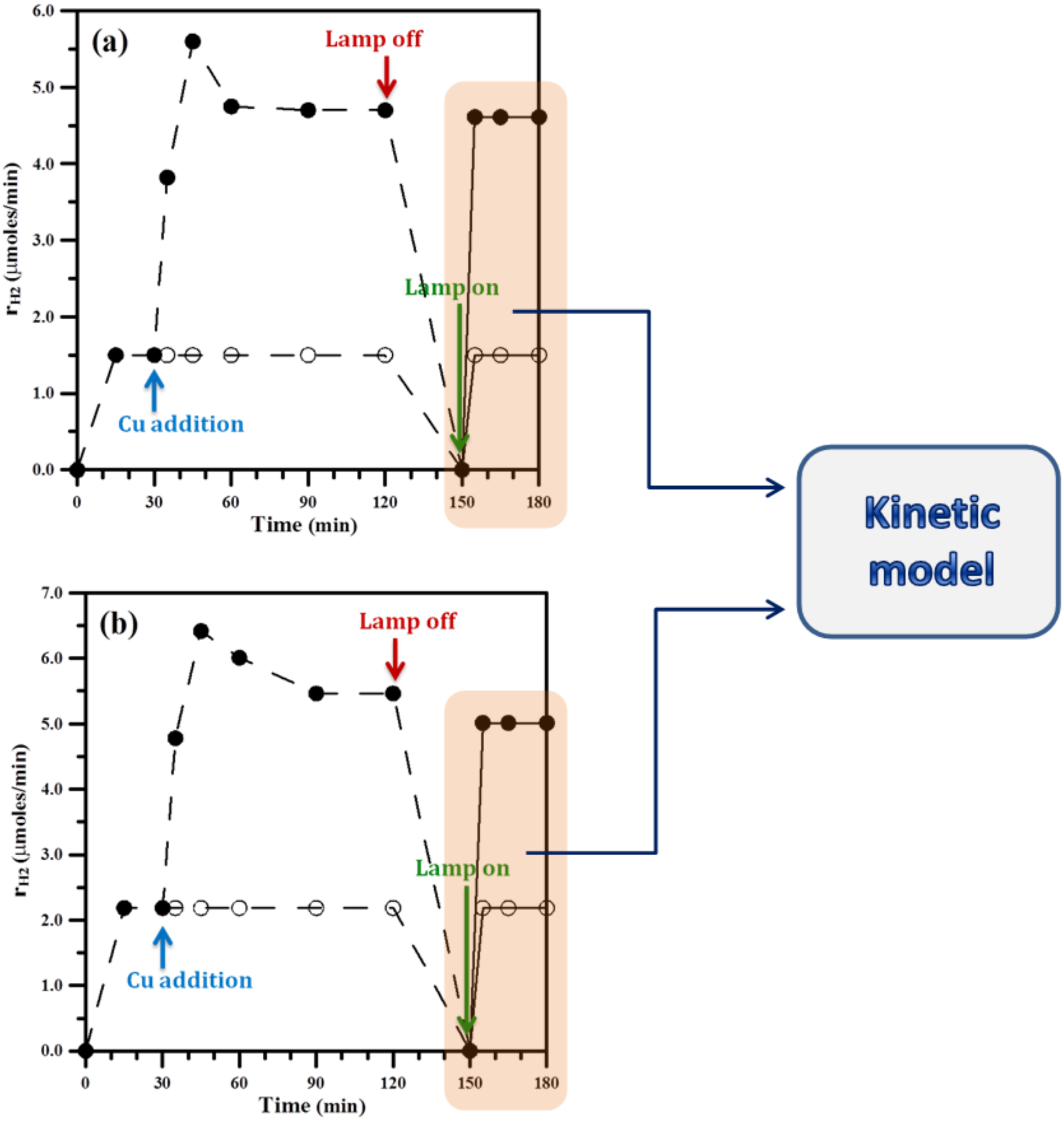

Figure 7.1: Hydrogen production rate for bare TiO_2-P25 (○) and $Cu_{(s)}/TiO_2$-P25 (●) during a typical photoreforming run under de-aerated conditions.

$[Cu(II)]_o$=0.24 mM. TiO_2 load = 150 mg·L^{-1}. Sacrificial agent: methanol (**a**), glycerol (**b**) $[CH_3OH]_o$=2.47 M. $[C_3H_8O_3]_o$=0.82 M.

According to the findings previously reported [130], a huge increase in radiation absorption in the visible range (λ > 400 nm) was recorded during the deposition of copper on the semiconductor. In order to understand if this phenomenon really contributes to charge carrier generation, some runs were repeated, both on glycerol and methanol, in presence of a filter (1 M sodium nitrite solution) capable of cutting-off UVA radiation emitted by the lamp (λ < 400 nm) [108]. The results of these runs (data not shown) indicated that the $Cu_{(s)}/TiO_2$-P25 system is not reactive under visible radiation only (λ > 400 nm).

The possibility of using the model proposed in the previous paragraph is conditioned by the availability of suitable values of kinetic parameters included in it ($\Phi_{UV}, \Phi_{Vis,}, k_r$,$k_{h^+}$ and K_{ads}). However, literature data are available only for some of the kinetic parameters needed. For example, some values for k_{h^+} and K_{ads} for glycerol [131,132] and methanol [132-134] using TiO_2 are reported.

For k_{h^+} parameter, a mean value of $1.4 \cdot 10^{10}$ $M^{-1} \cdot s^{-1}$ [132] was adopted as first attempt value for the modeling. On the other hand, comparing the values of K_{ads} reported for methanol, an one order of magnitude difference was found ($1.4 \cdot 10^{-2}$ $mg^{-1} \cdot L$ [134], $1.9 \cdot 10^{-3}$ $mg^{-1} \cdot L$ [133]). The difference could be ascribed to the different experimental conditions adopted such as pH, composition of the aqueous matrices and temperature. This observation raised some doubts on the reliability of K_{ads} literature values, and it was therefore decided not to use them for the present modeling investigation.

Therefore, in order to obtain values of the adsorption constants (K_{ads}) both for methanol and glycerol over $Cu_{(s)}/TiO_2$-P25, a Langmuir-Hinshelwood-type model expressing hydrogen generation rate was adopted:

$$r_{H_2} = \frac{k' \cdot K_{ads}[S]}{1 + K_{ads}[S]} \qquad eq_8$$

Starting from Langmuir-Hinshelwood equation (eq_8) and plotting the term $1/r_{H_2}$ against the reciprocal of the substrate concentration (Fig. 7.2), a linear trend was observed from which it was possible to derive the suitable values for K_{ads} for methanol and glycerol (Table 7.1).

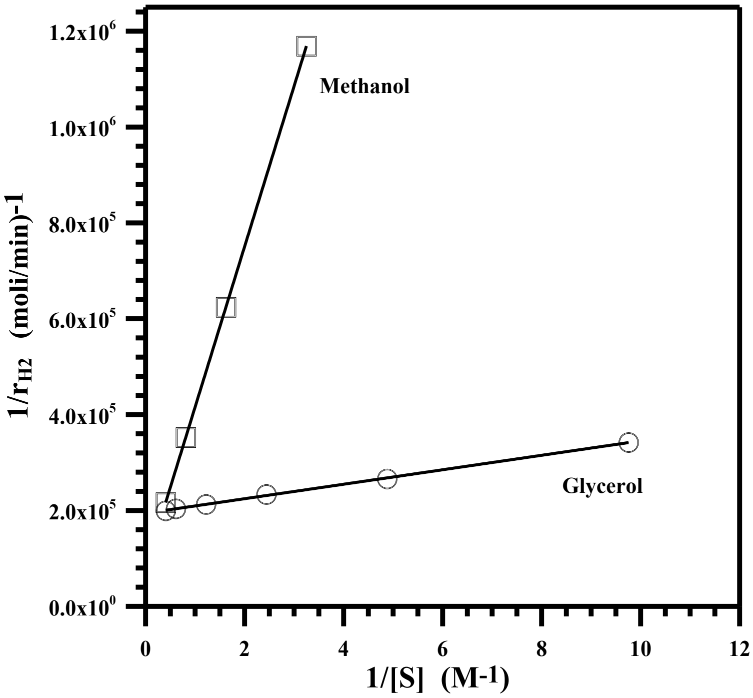

Figure 7.2: Effects of organic concentration both for methanol (□) and glycerol (○) on hydrogen production rate ($[C_3H_8O_3]_o$ = 0.10–2.47 M; $[CH_3OH]_o$ = 0.31–2.47 M; $[Cu(II)]_o$ = 0.24 mM; TiO_2-P25 load = 150 mg·L^{-1}).

K_{ads} for methanol (M^{-1})	K_{ads} for glycerol (M^{-1})	ε_{UV} ($M^{-1}\cdot s^{-1}$)
0.24	12.87	430

Table 7.1: Values of known kinetic parameters used in the model.

Following the indications given above on the runs in presence of the UVA cut-off chemical filter, it was considered that $\Phi_{VIS} = 0$, whereas no data were found for Φ_{UV} and k_r parameters for the catalyst used in the present investigation. The sole values found in the literature for these two parameters are related to bare TiO_2-P25 [127, 135,136], which could be adopted in the present modeling just as starting values for the optimization procedure. For the *N* parameter, that is the moles of active sites per unit mass of the catalyst, the value ($3.98 \cdot 10^{-4}$ mol·g^{-1}) was calculated from hydroxyl group surface density reported by Mueller *et al.* [137] for TiO_2-P25 and adopted as starting datum.

A more careful analysis of the model proposed indicated that the value of the extinction coefficient ε_{UV} for the catalyst investigated was required. Indeed, in the Lambert–Beer's-law-like equation (eq_9) the term ε_{UV} is used to account for the radiation power absorbed from the slurry ($I_{abs,UV}$):

$$I_{abs,UV} = \sum_i I^0_{\lambda_i} \left(1 - \mathrm{e}^{(-2.3 \cdot \mu \cdot \varepsilon_{UV} \cdot [TiO_2])}\right) \qquad eq_9$$

With the aim to derive a reliable value of ε_{UV}, data obtained for $I_{abs,UV}$ from the experimental measurements (see Chapter 4, Section 4.2) were inserted in equation *9*. An average value for ε_{UV} in the wavelength range 300-400 nm was thus calculated following this approach. In Table 7.1 the values adopted for some known parameters (K_{ads}, and ε_{UV}) are reported.

Once these values were adopted, the set of mass balance equations ($eq_1 - eq_4$) was solved by means of a proper numerical optimization procedures using the Matlab software. The procedures were initially applied to the analysis of data collected during methanol and glycerol photoreforming experiments carried out at different starting concentration of sacrificial agent and fixed catalyst load (150 mg·L^{-1}) (Table 7.2).

Run	Organic (S)	[S] (M)	$[TiO_2]$ ($mg\cdot L^{-1}$)	$[Cu(II)]_o$ (mM)
1a	Glycerol	0.102	150	0.24
2a	Glycerol	0.205	150	0.24
3a	Glycerol	0.41	150	0.24
4a	Glycerol	0.82	150	0.24
5a	Glycerol	1.64	150	0.24
6a	Glycerol	2.47	150	0.24
1b	Methanol	2.47	150	0.24
2b	Methanol	1.23	150	0.24
3b	Methanol	0.617	150	0.24

Table 7.2: Operating conditions of the experiments used in the optimization procedure.

Values for the unknown parameters (N, k_{h^+},k_r,and Φ_{UV}) were thus estimated by an iterative optimization procedure (Marquardt approach) that minimized the square of the differences between the differences between calculated and measured data for hydrogen generation rate and methanol consumption (objective function)[179]:

$$\phi = \sum_{l=1}^{m}\sum_{j=1}^{n}\sum_{i=1}^{h}\left(y_{i,j,l} - c_{ijl}\right)^2$$

in which the terms y and c are the calculated and experimental concentrations whereas m, n, and h are the number of experimental data recorded in each experiment, the number of the involved species and the number of the experiments used in the optimization procedure respectively.

To measure methanol consumption, the amount of formaldehyde formed at different reaction times was subtracted from methanol starting concentration. Unfortunately, poor results were obtained from this optimization since the capability of the model to simulate the system behavior appeared too weak by using the parameters adopted (data not shown). In order to overcome this limit, considering that the values of K_{ads} constants were obtained directly from the experimental data by using the Langmuir-Hinshelwood-type model, the possibility to adopt different initial values for k_{h^+} constants of methanol and glycerol was considered. Indeed, as reported above, a straight line was obtained by plotting the reciprocal of hydrogen generation rate against the reciprocal of substrate concentration, both for methanol and glycerol (eq_{10}):

$$\frac{1}{r_{H_2}} = \frac{1}{k'[S]} + \frac{K_{ads}}{k'} \qquad eq_{10}$$

Since $k' = k_{h^+}[h^+]\cdot N\cdot[TiO_2]$, the linear trend observed undoubtedly ruled out any dependence of $[h^+]$ upon $[S]$, at least in the range explored. In other words, considering that the mass balance on the photogenerated holes (eq_2) equals zero, for $[S]$ values producing $K_{ads}[S] \leq 1$ it was assumed that:

$$G \gg 2k_{h^+}\frac{C_T\cdot K_{ads}\cdot[S]}{(1 + K_{ads}\cdot[S])}\,[h^+] \qquad eq_{11}$$

As a result, equation *2* was equal to equation *12*:

$$\frac{d[h^+]}{dt} = G - k_r\cdot[h^+]\cdot[e^-] = 0 \qquad eq_{12}$$

which allowed to assess that $[h^+]$ is not dependent upon $[S]$. From equation *11* it became that the last result is obtained when equation *13* is true:

$$\Phi_{UV} \gg 4\left(\frac{C_T\cdot K_{ads}\cdot[S]}{1 + K_{ads}\cdot[S]}\right)^2 \frac{V}{I_{a,UV}}\frac{{k_{h^+}}^2}{k_r} \qquad eq_{13}$$

When the *N* value previously calculated for TiO_2-P25 [137] is used along with that for k_r given in the literature for the same oxide [127] and k_{h^+} found for methanol [132] respectively, depending on substrate concentration the right member in equation *13* was equal to the values reported in Table 7.3.

[S] (M)	$4\left(\frac{C_T\cdot K_{ads}\cdot[S]}{1+K_{ads}\cdot[S]}\right)^2\frac{V}{I_{a,UV}}\frac{{k_{h^+}}^2}{k_r}$ ($\mathrm{L\cdot ein^{-1}}$)
0.30	$1.69\cdot10^2$
0.61	$5.81\cdot10^2$
1.23	$1.86\cdot10^3$
2.47	$4.91\cdot10^3$

Table 7.3: Values obtained in equation eq_{13} at varying starting concentration of methanol.

Results reported in Table 7.3 required a meaningless value of Φ_{UV} for equation *13* to be satisfied. Therefore, values of k_{h^+} significantly lower than that previously reported [132] must be adopted for the reaction between organics and positive holes. However, the only additional indication found in literature on the reaction between an organic species and photogenerated holes was for benzyl alcohol [138]. The reaction resulted to be regulated by a kinetic constant more than five orders of magnitude lower than those reported for methanol and glycerol. In the absence of alternatives, this value was adopted as the starting one for k_{h^+} constant in the optimization procedure on data collected from methanol and glycerol photoreforming. Following this assumption, a new modeling attempt was performed resulting into a satisfactory simulation of the system behavior and producing best estimates for N, k_{h^+}, k_r, and Φ_{UV} unknown parameters with low associated uncertainties (Table 7.4). The low reported uncertainties indicated a high sensitivity of the model developed from the associated parameters.

k_r ($M^{-1} \cdot s^{-1}$)	Φ_{UV}	k_{h^+} for methanol ($M^{-1} \cdot s^{-1}$)	k_{h^+} for glycerol ($M^{-1} \cdot s^{-1}$)	N ($mol \cdot g^{-1}$)
$3.91 \cdot 10^6$ ± $3.85 \cdot 10^4$	0.19 ± $2.0 \cdot 10^{-3}$	$1.13 \cdot 10^4$ ± $5.63 \cdot 10^1$	$4.76 \cdot 10^3$ ± $1.19 \cdot 10^2$	$3.69 \cdot 10^{-4}$ ± $1.0 \cdot 10^{-5}$

Table 7.4: Best estimated values of unknown kinetic parameters (k_r, Φ_{UV}, k_{h^+}, and N) for $Cu_{(s)}/TiO_2$-P25 catalyst.

Figures 7.3 and 7.4a,b show a comparison between predicted and experimental data for photoreforming of methanol and glycerol respectively.

The following remarks derived from these data:

- the best estimated value of the rate constant for electron-hole recombination (k_r) on nanocopper-TiO_2 is about four orders of magnitude lower than that reported in the literature for bare TiO_2 ($3.0 \cdot 10^{10}$ M^{-1} s^{-1} [127]) thus confirming the electron trapping role of zero-valent copper nanoparticles and the consequent improvement in photocatalytic activity [130];
- a primary quantum yield higher than that found in the literature for TiO_2 for similar wavelengths range [135,136] was estimated for the catalyst adopted showing a more efficient use of absorbed energy;
- the values obtained for K_{ads} constants for methanol and glycerol on nanocopper TiO_2 photocatalyst are several orders of magnitude lower than those reported for the same species on TiO_2-P25;
- the value estimated for N is quite similar to those previously calculated for TiO_2-P25 ($2.74 \cdot 10^{-4}$ $mol \cdot g^{-1}$ [139] and $3.98 \cdot 10^{-4}$ $mol \cdot g^{-1}$ [137]) suggesting that copper deposition may only negligibly modify the surface of semiconductor used.

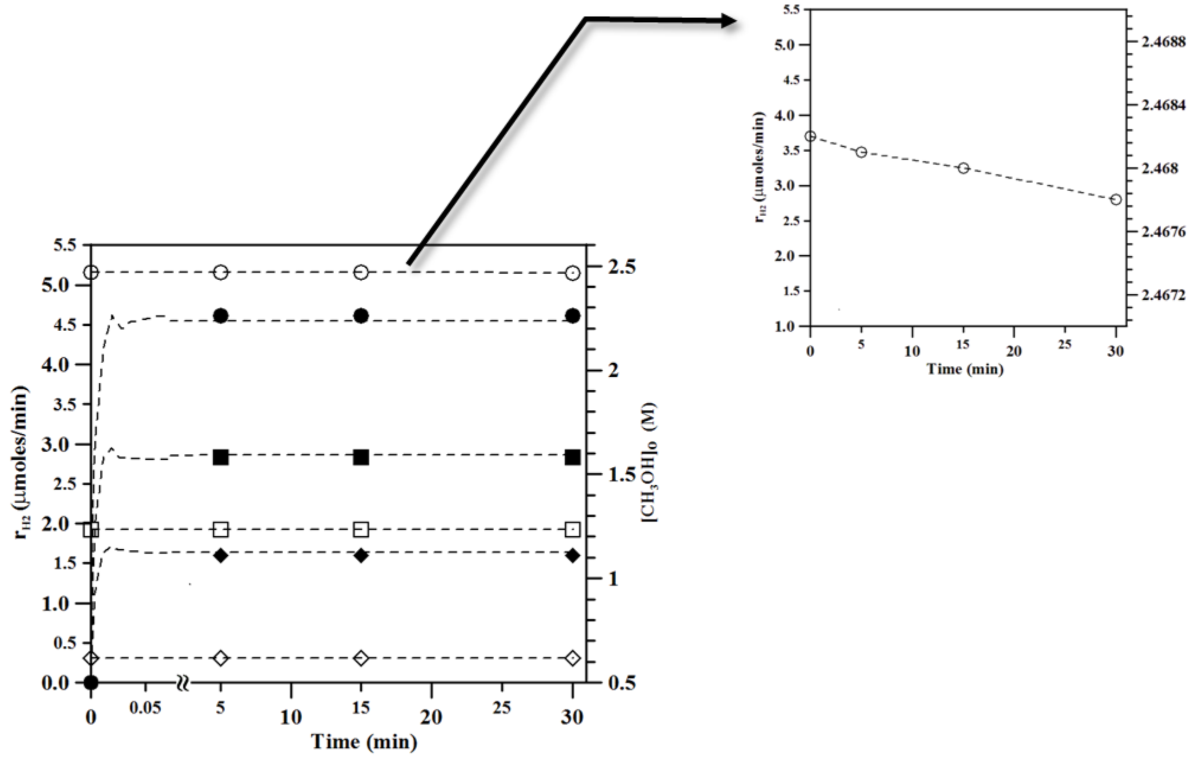

Figure 7.3: Comparison between experimental (symbols) and calculated values (dashed lines) using methanol as sacrificial agent. $[Cu(II)]_o$= 0.24 mM, TiO_2-P25 load = 150 mg·L^{-1}.
Full symbols: hydrogen production rates; empty symbols: methanol concentrations.
$[CH_3OH]_o$ = 2.47 M (●, ○), 1.23 M (■, □), 0.617 M (◆, ◇).

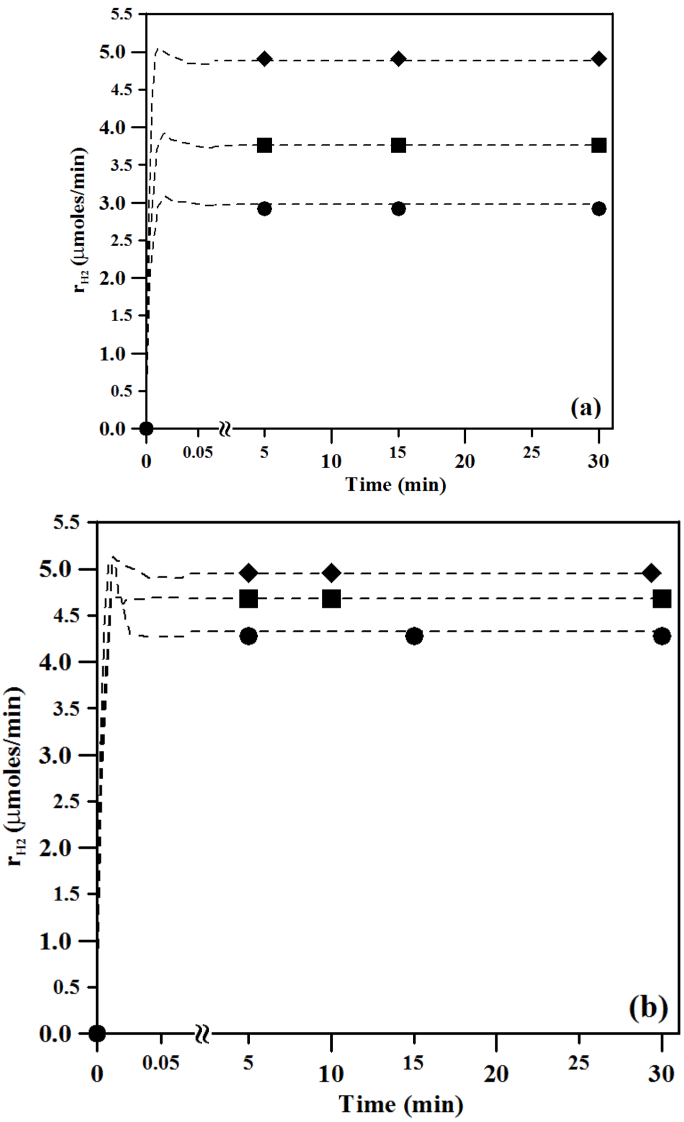

Figure 7.4: Comparison between experimental (symbols) and calculated hydrogen production rates (dashed lines) using glycerol as sacrificial agent. $[Cu(II)]_o$= 0.24 mM, TiO_2-P25 load = 150 mg·L^{-1}.

(**a**) $[C_3H_8O_3]_o$ = 0.102 M (●), 0.205 M (■), 1.64 M (◆).

(**b**) $[C_3H_8O_3]_o$ = 0.410 M (●), 0.820 M (■), 2.47 M (◆).

The model was validated by predicting the results of an additional set of glycerol and methanol photoreforming runs without any further adjustment of the kinetic parameters estimated (simulation mode). For this simulation procedure, data from experiments carried out at various starting concentrations of (*i*) sacrificial agent, (*ii*) cupric ion, and (*iii*) TiO_2-P25 load were selected. The comparison between experimental and theoretical results highlights the ability of the model to successfully predict the hydrogen generation rates and methanol consumption (Figs. 7.5 and 7.6).

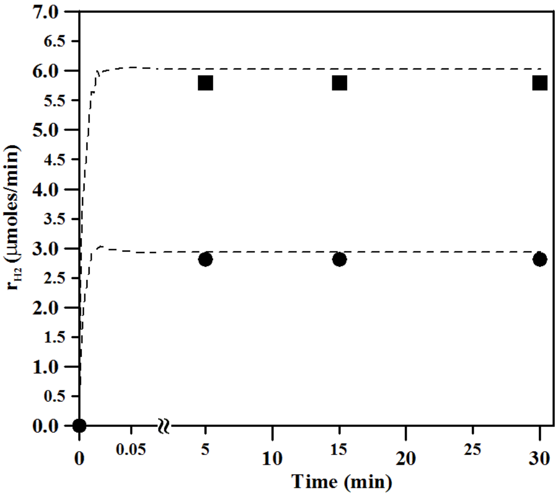

Figure 7.5: Comparison between experimental (symbols) and calculated hydrogen production rates (dashed lines) using glycerol as sacrificial agent: simulation mode.

(●): $[C_3H_8O_3]_o = 0.82$ M, $[Cu(II)]_o = 0.16$ mM, TiO_2-P25 load = 100 mg·L^{-1}.

(■): $[C_3H_8O_3]_o = 0.82$ M, $[Cu(II)]_o = 0.30$ mM, TiO_2-P25 load = 190 mg·L^{-1}.

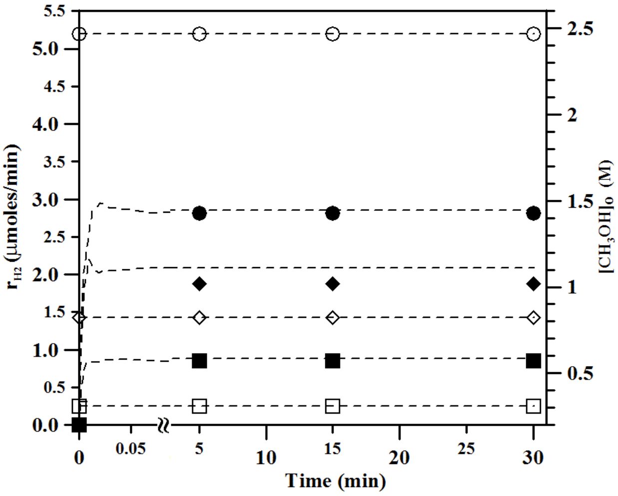

Figure 7.6: Comparison between experimental (symbols) and calculated hydrogen production rates (dashed lines) using methanol as sacrificial agent: simulation mode.

Full symbols: hydrogen production rates; empty symbols: methanol concentrations.

(●, ○): $[CH_3OH]_o = 2.47$ M, $[Cu(II)]_o = 0.16$ mM, TiO_2-P25 load = 100 mg·L^{-1}.

(■, □): $[CH_3OH]_o = 0.31$ M, $[Cu(II)]_o = 0.24$ mM, TiO_2-P25 load = 150 mg·L^{-1}.

(◆, ◇): $[CH_3OH]_o = 0.82$ M, $[Cu(II)]_o = 0.24$ mM, TiO_2-P25 load = 150 mg·L^{-1}.

7.4 Summary

Methanol and glycerol were separately employed in photocatalytic reforming for hydrogen production on metal-copper modified TiO_2 nanoparticles prepared “in situ” starting from an aqueous suspension containing cupric ions and TiO_2.

Starting from the mass balance equations for the main species involved in the photocatalytic process, a kinetic model was developed with the aim of simulating photocatalytic hydrogen generation. The model analyzed data collected during the experimental campaign at various substrate (methanol and glycerol) concentrations and catalyst loads.

As a result, the best values of unknown parameters were estimated, such as (*i*) the rate of hole-capture and (*ii*) the adsorption equilibrium constants for both methanol and glycerol, (*iii*) the primary quantum yield and (*iv*) the rate constant for electron-hole recombination on the nanocopper modified-TiO_2. From the values found for these parameters it can be stated that:

(1) a decrease in the recombination reaction occurs for the catalyst adopted, thus indicating the fundamental role played by copper nanoparticles on TiO_2 surface in trapping photogenerated electrons and therefore improving hydrogen generation;

(2) the photocatalytic system adopted is characterized by a more efficient use of the energy absorbed;

(3) the value estimated in this study for equilibrium adsorption constant of glycerol is more than one order of magnitude higher than that calculated for methanol. Both the estimated constants are orders of magnitude lower than those reported in the literature for the same species on bare TiO_2-P25;

(4) copper deposition on the semiconductor surface negligibly modifies its surface.

8. Results IV

Photoreforming of formic acid in the presence of Cl^-, Cu(II), and TiO_2 suspended particles

8.1 Introduction

The possibility of employing sacrificial organic agents contained in wastewaters for photocatalytic hydrogen production suggests the need of considering the simultaneous presence of other species in aqueous solution, such as inorganic ions (i.e., Cl^-, SO_4^{2-}, NO_3^-, etc.). As an example, several industrial branches, such as petroleum, agro-food and leather sectors, generate highly saline wastewaters with significant organic content. The presence inorganic ions may have a significant effect on the overall photoefficiency for hydrogen generation.

It is precisely in this context that a promising Cu-TiO_2 photocatalytic system based on solar reforming of formic acid in presence of chloride ion was investigated. As demonstrated in the previous chapters, the use of copper species helps enhance the efficiency of hydrogen generation in TiO_2-based photoreforming processes, thus opening the exploitation of such systems to industrial scale. Moreover, this system is of large interest as formic acid is a common waste product generated during the manufacture and use of other chemicals, such as acetic acid, biomass materials, and dyes.

Such investigation was stimulated by literature indications [41,174] on the tendency of zero-valent copper to undergo a photocorrosive process, at very low pH (0.0–2.0), in presence of chloride ions and under UV–solar simulated radiation. As reported by Eisel et al. [174], the photo-oxidation of zero-valent copper in presence of chloride ions ($r_{8.1}$–$r_{8.2}$) results into hydrogen generation through proton reduction ($r_{8.3}$):

$$\mathrm{Cl^-}_{\mathrm{ads}} + \mathrm{H^+}_{\mathrm{aq}} \xrightarrow{\mathrm{h\nu,Cu^0}} \mathrm{Cl^\bullet}_{\mathrm{ads}} + \mathrm{H^\bullet}_{\mathrm{aq,ads}} \qquad r_{8.1}$$

$$\mathrm{Cl^\bullet}_{\mathrm{ads}} + \mathrm{Cu^0} \rightarrow \mathrm{CuCl}_{\mathrm{aq,ads}} \qquad r_{8.2}$$

$$\mathrm{H^\bullet}_{\mathrm{aq,ads}} + \mathrm{H^\bullet}_{\mathrm{aq,ads}} \rightarrow \mathrm{H}_{2(g)} \qquad r_{8.3}$$

In addition, in this system hydrogen can be produced also by photolysis of cuprous complexes formed in the solution ($r_{8.4}$–$r_{8.8}$) [175]:

$$\mathrm{Cu^{1+}} + 2\mathrm{Cl^-} \rightleftarrows \mathrm{CuCl_2}^- \qquad r_{8.4}$$

$$\mathrm{Cu^{1+}} + 3\mathrm{Cl^-} \rightleftarrows \mathrm{CuCl_3}^{2-} \qquad r_{8.5}$$

$$\mathrm{CuCl_2}^- + \mathrm{H^+} \xrightarrow{\mathrm{h\nu}} \mathrm{Cu^{2+}} + 2\mathrm{Cl^-} + \mathrm{e^-}_{\mathrm{s}} \qquad r_{8.6}$$

$$\mathrm{CuCl_3}^{2-} + \mathrm{H^+} \xrightarrow{\mathrm{h\nu}} \mathrm{Cu^{2+}} + 3\mathrm{Cl^-} + \mathrm{e^-}_{\mathrm{s}} \qquad r_{8.7}$$

$$H^+ + \mathrm{e^-}_{\mathrm{s}} \rightarrow \frac{1}{2}\mathrm{H_{2(g)}} \qquad r_{8.8}$$

A continuous production of hydrogen could be thus imagined coupling the last system (Figure 8.1, Subsystem 2) with another one (Figure 8.1, Subsystem 1). The resulting complete system allows the photocatalytic reduction of cupric ions to zero-valent copper in presence of solid TiO_2 – and the oxidation of an organic species, such as formic acid, used as sacrificial agent – followed by a copper reoxidation with a simultaneous hydrogen generation [41].

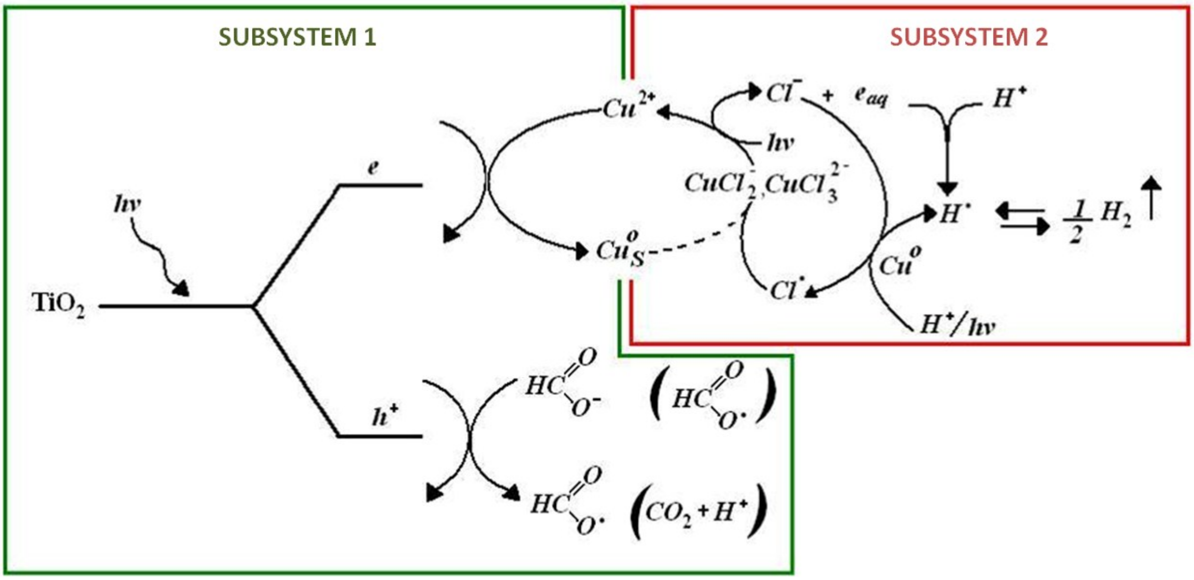

Figure 8.1: Schematic illustration of the complete system for hydrogen generation through nano-TiO_2 photocatalytic reforming of formic acid in presence of copper species and chloride ions.

The complete system makes possible, at least in principle, the generation of hydrogen through the photoreforming of an organic species which could also be contained in wastewaters.

Although Lanese et al. [41] presented the possibility to generate hydrogen through the complete system as proof of concept, the data collected so far indicate that hydrogen production cannot only be attributed to a simple combination of Subsystems 1 and 2. In fact, hydrogen generation was observed for prolonged reaction times only for particular initial values of some experimental variables, such as the following: formic acid concentration, chloride ion concentration, total dissolved copper concentration, starting oxidation state of copper (zero-valent or cupric ions) and TiO_2 load. For all the experimental conditions tested in which initially zero-valent copper was used starting from the complete system, no hydrogen production was recorded during the run, although its formation only due to Subsystem 2 was surely observed (for this uncertainty a dotted line is adopted to indicate this pathway in Figure 8.1). On the other hand, the formation of hydrogen was observed in some runs starting from copper initially present as cupric ions and TiO_2 load not higher than 100 mg/L. However, Lanese et al. [41] did not performed detailed investigations to clearly identify for these variables the concentration range which can guarantee the best performances of the complete system. In particular, no indications were reported on the system reactivity over a wide concentration range neither of formic acid, chloride or total cupric ions (separately or simultaneously added to the reacting system), nor of pH of the solution.

The present investigation aimed at fulfilling this lack of information in order to provide the best conditions which maximize the hydrogen generation rate, which is proportional to the maximum efficiency of hydrogen production.

8.2 Results and discussion

In Figure 8.2 is shown an example of the results collected during a typical photocatalytic run starting from a suspension containing cupric ions (5.0 mM), chloride ions (10^3 mM), formic acid (10^3 mM) and TiO_2 anatase (10^2 mg/L). The hydrogen production rate increases until a value of about 8 μmol/min is reached and slightly reduces after the first hour of reaction time, whereas the total dissolved copper concentration keeps approximately constant throughout the experiment. The idea that the trend observed is due to a decrease of formic acid concentration could not be demonstrated, since no appreciable decreasing of formic acid concentration was detected by HPLC analyses (data not shown).

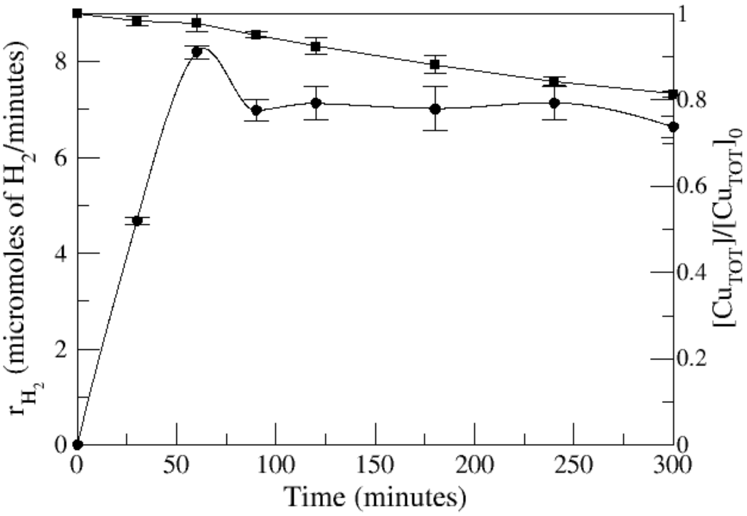

Figure 8.2: Hydrogen production rate (●) and dissolved copper normalized concentration (■) at pH=1.0 (with $HClO_4$), $[HCOOH]_0=10^3$ mM, $[Cu(II)]_0=5.0$ mM, $[NaCl]_0=10^3$ mM, TiO_2 anatase load=10^2 mg/L.

8.3 Effect of formic acid concentration

As reported in Figures 8.3a–b, the effect of changing the initial formic acid concentration towards the hydrogen production rate and Cu(II) consumption was investigated between 10 mM and $5.0 \cdot 10^3$ mM. It is evident that, keeping constant initial cupric ion and chloride concentrations, TiO_2 anatase load and pH, the higher the formic acid concentration, the higher the maximum hydrogen production rate observed. The values of hydrogen production rate vary from 0.7 to 8.3 µmol/min, at least until formic acid concentration is equal to 10^3 mM.

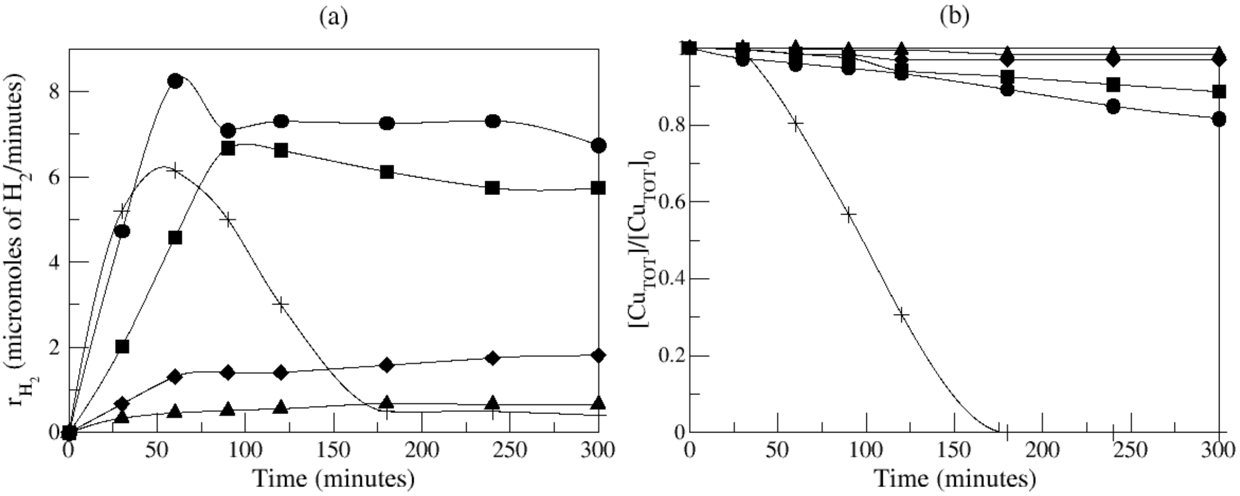

Figure 8.3: Effect of formic acid concentration: hydrogen production rate (**a**) and dissolved copper normalized concentration (**b**) at pH=1.0 (with $HClO_4$), $[Cu(II)]_0$=5.0 mM, $[NaCl]_0$=10^3 mM, TiO_2 anatase load=10^2 mg/L, $[HCOOH]_0$ (mM): (+) $5.0 \cdot 10^3$, (●) 10^3, (■) $5.0 \cdot 10^2$, (◆) 10^2, (▲) 10.

Since hydrogen production proceeds through an initial reduction of cupric ions ($r_{8.9}$), made possible by a contemporary oxidation of formic acid ($r_{8.10}$), a monotonic increase of hydrogen generation rate is clearly expected for higher concentrations of formic acid according to the results previously reported [41]:

$$\mathrm{Cu(II)} \xrightarrow{e^-_{CB}} \mathrm{Cu(I)} \xrightarrow{e^-_{CB}} \mathrm{Cu(0)} \qquad r_{8.9}$$

$$\mathrm{HCOOH} \xrightarrow{h^+_{VB}} CO_2^{\bullet -} + 2H^+ \qquad r_{8.10}$$

As previously reported, the concentration of the organic species influences the rate of cupric ion reduction during the sacrificial photocatalytic process [176]. It can be thus supposed that reduced copper species, i.e. cuprous ones formed through reaction r_9, in presence of chlorides and under UV irradiation immediately reoxidize ($r_{8.6} - r_{8.7}$), therefore ejecting electrons ($e^-{}_s$) in the solution and allowing a prompt reduction of protons ($r_{8.8}$).

Only a moderate reduction, if any, of total dissolved copper and low hydrogen generation rates were recorded during the runs with the lowest initial formic acid concentration (Figure 8.3, full diamonds and triangles). For a starting formic acid concentration of 10^3 mM, a reduction in dissolved copper of about 20% was recorded within a reaction time of 300 minutes (Figure 8.3, full circles).

It is worth considering that the formation of hydrogen proceeds through two consecutive steps: a first one ($r_{8.9}$) in which a preventive reduction of cupric ions to cuprous ones occurs with a contemporary formic acid oxidation ($r_{8.10}$), and a second one consisting in the photolysis of some chloride complexes of cuprous ions ($r_{8.6} - r_{8.7}$). It can be thus hypothesized that any increase in initial concentration of formic acid may result into a faster reduction of cupric ions. The results collected indicate that, for formic acid concentrations up to 10^3 mM, the rate determining step is represented by cupric ion reduction. It is therefore enough to accelerate the determining step to have a faster hydrogen generation for formic acid concentrations between 10 mM and 10^3 mM.

At the highest formic acid concentration tested, equal to $5.0 \cdot 10^3$mM (Figure 8.3, cross symbols), dissolved copper was completely reduced after 180 minutes of reaction, casting doubt on the catalytic role of copper. In other words, it seems that the complete system (Figure 8.1) is characterized by a certain tendency of zero-valent copper to precipitate and be not capable of undergoing further reoxidations; therefore, zero-valent copper can be deemed completely unreactive for increasing reaction times. It could be reasonably considered that, under the adopted conditions (formic acid concentration equal to $5.0 \cdot 10^3$mM), the photocatalytic reduction rate of cuprous ions is by far higher than the reoxidation rate of zero-valent copper ($r_{8.1} - r_{8.2}$), provided that this reoxidation occurs. Alternatively, it should be taken into account the possibility that the complete system (Figure 8.1) inhibits zero-valent copper oxidation together with hydrogen formation. An attempt to throw light on this specific point was made by investigating hydrogen generation in the system zero-valent copper/formic acid/chlorides/nano-TiO_2/UV irradiation at pH=1.0. The data indicate values of hydrogen generation as lower as those recorded in the system formic acid/chlorides/nano-TiO_2/solar UV radiation at pH=1.0, without any significant accumulation of dissolved copper as Cu(I) or Cu(II) ions. This result clearly indicates that a photoxidation of zero-valent copper in presence of chloride ions, formic acid and nano-TiO_2 does not occur at all.

8.4 Effect of chloride ion concentration

The effect of changing the initial chloride ion concentration was investigated in the range 10^2–$2.0 \cdot 10^3$ mM (Figures 8.4a–b).

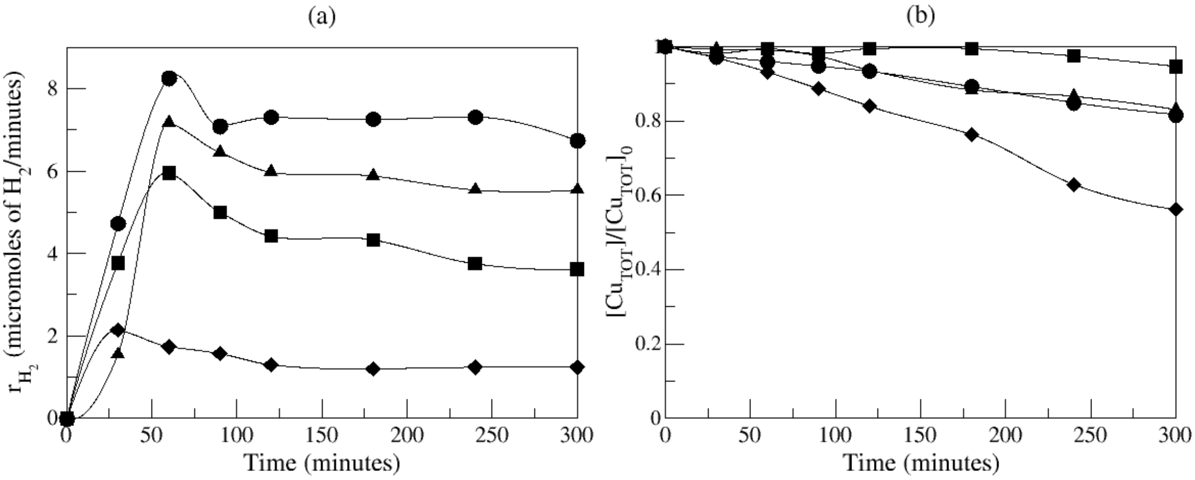

Figure 8.4: Effect of chloride ion concentration. Hydrogen production rate (**a**) and dissolved copper normalized concentration (**b**) at pH=1.0 (with $HClO_4$), $[Cu(II)]_0$=5.0 mM, $[HCOOH]_0=10^3$ mM, TiO_2 anatase load=10^2 mg/L, $[NaCl]_0$ (mM): (▲) $2.0 \cdot 10^3$ mM, (●) 10^3 mM, (■) $5.0 \cdot 10^2$ mM, (◆) 10^2 mM.

For fixed formic acid concentration, any increase in addition of chloride ions to the reacting solution results into a higher hydrogen generation rate (the maximum value recorded is 8.3 µmol/min for a chloride ion concentration of 10^3 mM). However, it is interesting to stress that, contrary to what observed in the runs with variable formic acid concentration, for the lowest value of chloride ion tested (10^2 mM) a significant reduction of total dissolved copper was recorded, along with the precipitation of a reddish–brown solid on TiO_2.

These results may be explained by supposing that, if chloride ion concentration is reduced, Cu(I) reoxidation through chloride complexes photolysis $(r_{8.6} - r_{8.7})$ is slowed down and becomes the rate determining step. As a consequence of this behavior, the rate of hydrogen generation decreases too.

On the other hand, a reduction in hydrogen production rate was observed for further increases in chloride ion concentration from 10^3 mM up to $2.0 \cdot 10^3$ mM (Figure 8.4, full triangles). It is known that at rising chloride ion content both Cu(I) and Cu(II) may form different complexed species, such as $CuCl_2^-$ and $CuCl_3^{2-}$ (for cuprous ions) [177] or $CuCl^+$, $CuCl_2$ and $CuCl_3^-$ (for cupric ions) [178]. The formation of Cu(II)–chloride complexes results into the occurrence of a shielding effect which reduces the radiation absorption by Cu(I)–chloride complexes. Indeed, both cuprous and cupric complexes are capable of absorbing in the same radiation range of the lamp used (305–366 nm) with comparable extinction coefficients, although those belonging to Cu(I) complexes type are slightly higher (Figure 8.5).

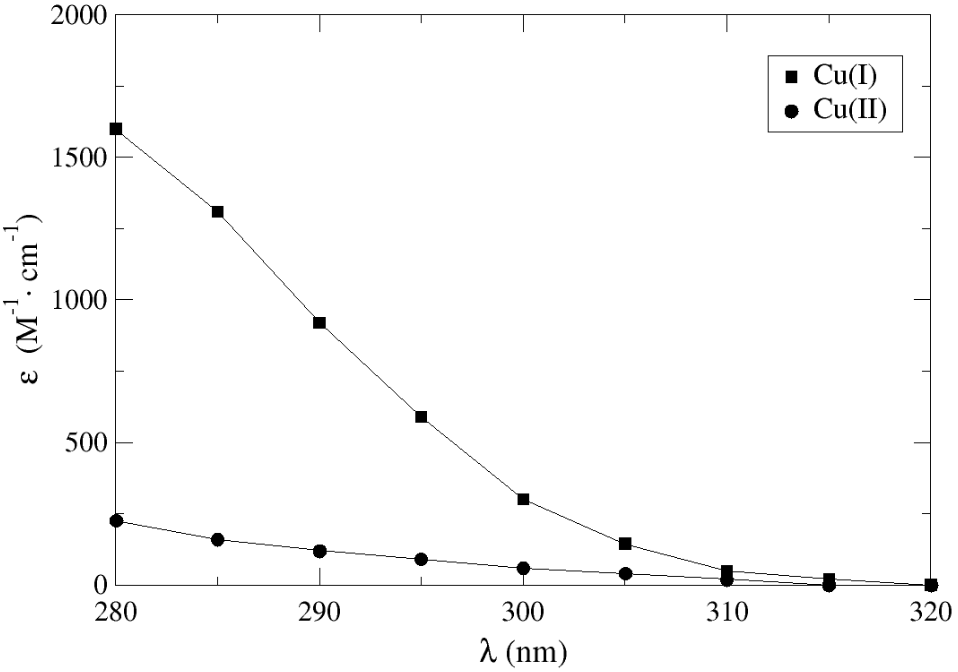

Figure 8.5: UV spectra of Cu(I) and Cu(II) chloride complexes (data source: Davis et al., 1978 [177]).

For higher chloride ion concentrations, an increase in concentration of all chloride complexes occurs, causing two opposite effects: (i) a rise in concentration of cuprous-chloride complexes ($CuCl_2^-$ and $CuCl_3^{2-}$), which absorb and photolyze at wavelengths higher than 290 nm [177]; (ii) an increase in concentration of cupric–chloride complexes ($CuCl^+$, $CuCl_2$ and $CuCl_3^-$) and, consequently, of their shielding effect. It can be considered that the shielding effect prevails for chloride concentrations higher than 10^3 mM, with a consequent reduction in hydrogen generation rate. However, only the availability of a suitable kinetic model could help to completely throw light on this issue.

So as to determine the nature of the precipitate, a sample recovered at the end of a run at pH=1 washed accordingly with the procedure reported in the experimental was submitted to a XRD measurement (Fig 8.6). Two peaks at 2Θ equal to 43°3' and 50°5' which can be ascribed to zero-valent copper were observed. Therefore, it can be concluded that the solid recovered is represented by zero-valent copper.

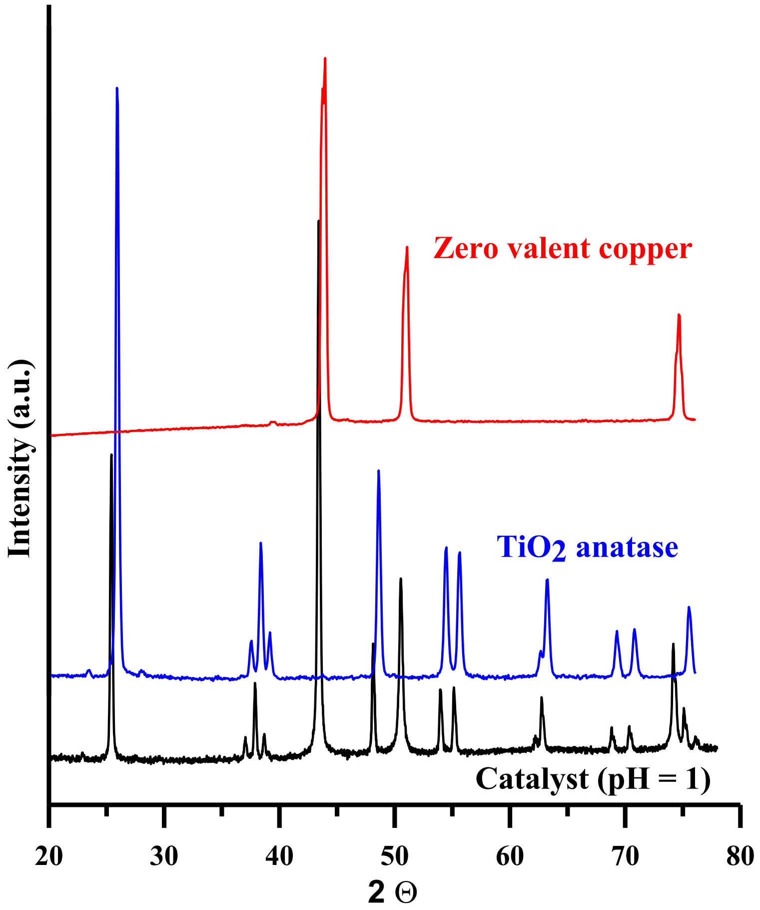

Figure 8.6: XRD patterns registered for a solid sample recovered at the end of a photocatalytic run at pH=1, bare TiO_2 (anatase) and Cu(0) powders.

8.5 Effect of cupric ion concentration

The influence of initial cupric ion concentration on hydrogen production rate and dissolved copper concentration is reported in Figure 8.7. Distinct behaviors were recorded when initial cupric ion concentration changes from 2.5 mM to 5.0, 10.0 and 20.0 mM (Figures 8.7a–b).

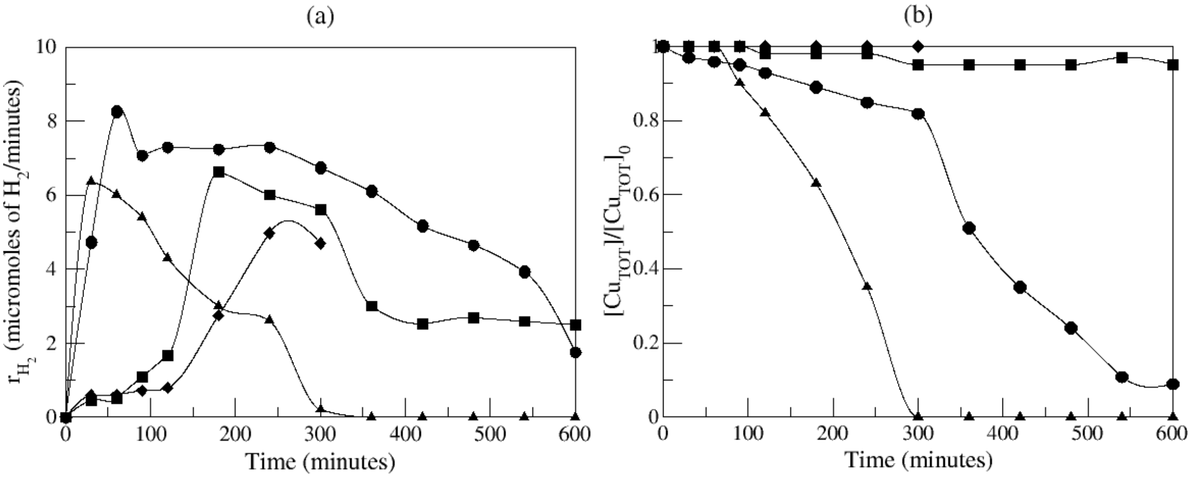

Figure 8.7: Effect of cupric ion concentration. Hydrogen production rate (**a**) and dissolved copper normalized concentration (**b**) at pH=1.0 (with $HClO_4$), $[HCOOH]_0=10^3$ mM, $[NaCl]_0=10^3$ mM, TiO_2 anatase load=10^2 mg/L, $[Cu(II)]_0$ (mM): (▲) 2.5, (●) 5.0, (■) 10, (◆) 20.

A delayed hydrogen production and a lower decrease in dissolved copper were observed at rising initial cupric ion concentration from 5.0 to 20 mM. A complete reduction of cupric ions and a reddish solid precipitation within 300 minutes of reaction were recorded only for the run starting from a cupric ion concentration of 2.5 mM. XRD measurements have demonstrated that the solid is represented by zero-valent copper (data not shown).

To explain these observations it has to be considered that at increasing cupric ion concentration between 5.0 and 20 mM, the shielding effect due to the formation of Cu(II)–chloride complexes becomes more significant and lowers the rate of hydrogen production. When cupric ion concentration is hugely reduced through the reaction between cupric ions and photoelectrons ($r_{8.9}$) (with a significant increase in concentration of Cu(I) in the form of Cu(I)–chloride complexes), the rate of hydrogen production reaches a maximum value (Figure 8.7).

For initial cupric ion concentration equal to 2.5 mM, the less important shielding effect promotes a faster hydrogen production, but also a rapid photocatalytic reduction of Cu(I) to zero-valent copper ($r_{8.9}$) which does not reoxidize. Indeed, in this case the maximum value of hydrogen production rate is lower with respect to that recorded starting from a cupric ion concentration of 5.0 mM.

A more careful examination of these data indicates that different quantities of hydrogen are produced per moles of precipitated copper ($P_{H_2}/\ P_{Cu(0)}$, Table 8.1) for reaction times of 300 and 600 minutes respectively, depending on the initial concentration of cupric ion adopted. The best results, consisting in highest values of $P_{H_2}/\ P_{Cu(0)}$, were recorded in the run with a starting cupric ion concentration of 5.0 mM for both reaction times. The results collected indicate that a complete precipitation of dissolved copper happens at about 600 minutes of reaction. This demonstrates a certain tendency of the catalytic system to deactivate, as already observed in the run starting from a cupric ion concentration of 2.5 mM. In other words, it is clear that, even for different reaction times depending on the initial cupric ion concentration and still in presence of significant quantities of formic acid, the system becomes no more capable of producing hydrogen. This deactivation of the system can be considered as a consequence of the complete precipitation of zero-valent copper.

$[Cu(II)]_0$ mM	$P_{H_2}/\ P_{Cu(0)}$ 300 min	$P_{H_2}/\ P_{Cu(0)}$ 600 min
2.5	1.8	1.8
5.0	3.8	3.5
10	2.7	1.8
20	1.7	–

Table 8.1: Effect of cupric ion concentration: correlation between micromoles of H_2 generated (P_{H_2}) and micromoles of Cu(0) precipitated ($P_{Cu(0)}$) after 300 and 600 minutes of reaction at pH=1.0, T=25 °C, $[HCOOH]_0=10^3$ mM, $[NaCl]_0=10^3$ mM, TiO_2 load=10^2 mg/L.

8.6 Effect of pH of the solution

Since a dependence of hydrogen generation rate on protons concentration (and pH) may be assumed, the best results could be expected under low pH condition. Indeed, proton reduction is a fundamental reaction through which the process develops. However, in most of the researches appeared in literature on copper–based TiO_2 photocatalysts for hydrogen generation, the best performances are reported for basic or strong basic condition [82,98,107]. The prevailing explanation seems to rely on the detrimental effect that acidic conditions exert on the catalyst stability, with a continuous copper leaching into the solution [60,93].

To assess the effect on the system reactivity of pH in the solution, two additional photocatalytic runs were performed at pH 2.5 and 4.0 respectively, for both chloride ion and formic acid initial concentrations equal to 10^3 mM, cupric ion concentration at 5.0 mM and TiO_2 load equal to 10^2 mg/L. The results collected during these runs are shown in Figure 8.8a-b.

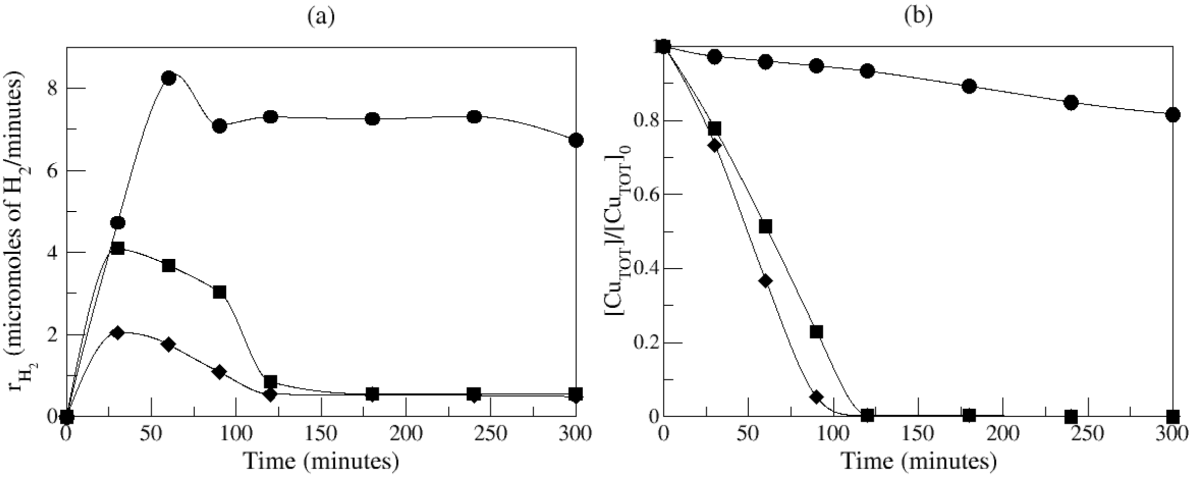

Figure 8.8: Effect of pH. Hydrogen production rate (**a**) and dissolved copper normalized concentration (**b**), $[Cu(II)]_0$=5.0 mM, $[HCOOH]_0=10^3$ mM, $[NaCl]_0=10^3$ mM, TiO_2 anatase load=10^2 mg/L, pH: ● 1.0, ■ 2.5, ◆ 4.0.

It is interesting to observe that both at pH 2.5 and 4.0 hydrogen production appears to be depressed and reaches zero after about 120 minutes of reaction. For the same reaction time total dissolved copper reduces to zero and a black solid is formed on TiO_2 nano-particles.

Also in this case, an attempt to characterize the nature of copper deposited on TiO_2 nanoparticles was made. The solid sample was firstly washed as reported in the experimental and then submitted to X-ray diffraction analysis. XRD spectrum (Figure 8.9) shows two peaks at 2Θ equal to 43°3' and 50°5', clearly indicating the presence of zero-valent copper.

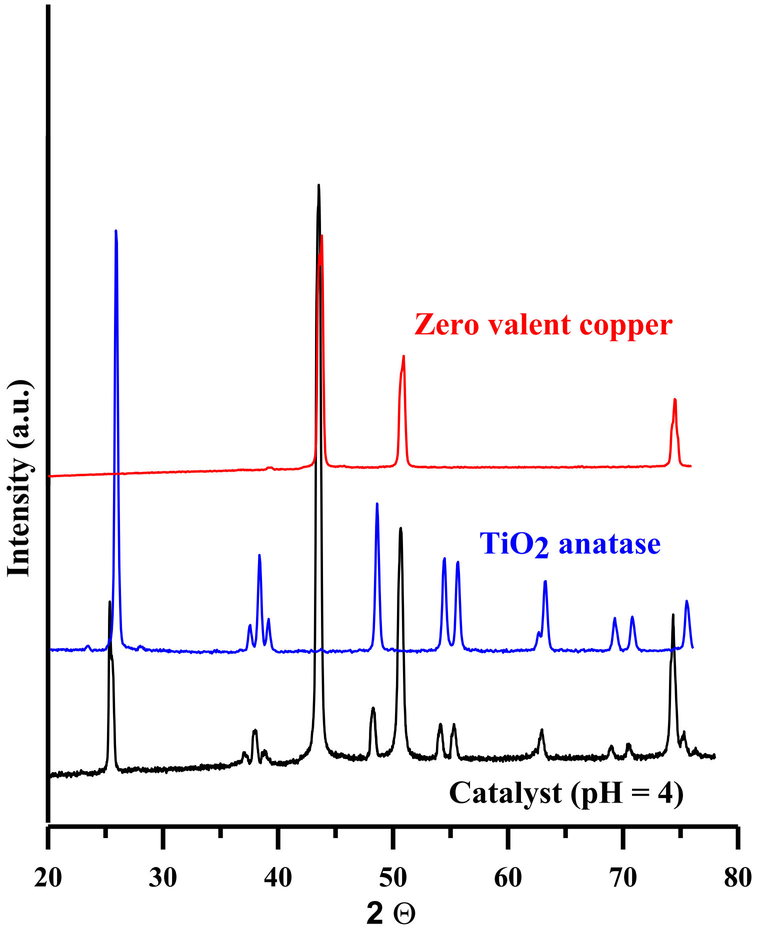

Figure 8.9: XRD patterns registered for a solid sample recovered at the end of a photocatalytic run at pH=4, bare TiO_2 (anatase) and Cu(0) powders.

The above–reported results may be explained considering that in both runs a significantly lower protons concentration is present with respect to the case of pH=1.0, with a consequent reduction in the rates of solvated electrons ($e^{-}{}_{s}$) capture by protons and hydrogen generation. In these conditions, a higher availability of solvated electrons may be expected in solution with a consequent enhancement in Cu(I) and Cu(II) reduction. In other words, copper is continuously separated from the solution through a reduction of dissolved copper species until the system becomes completely unreactive. The behavior of the system investigated may be depicted by means of the scheme illustrated in Figure 8.10.

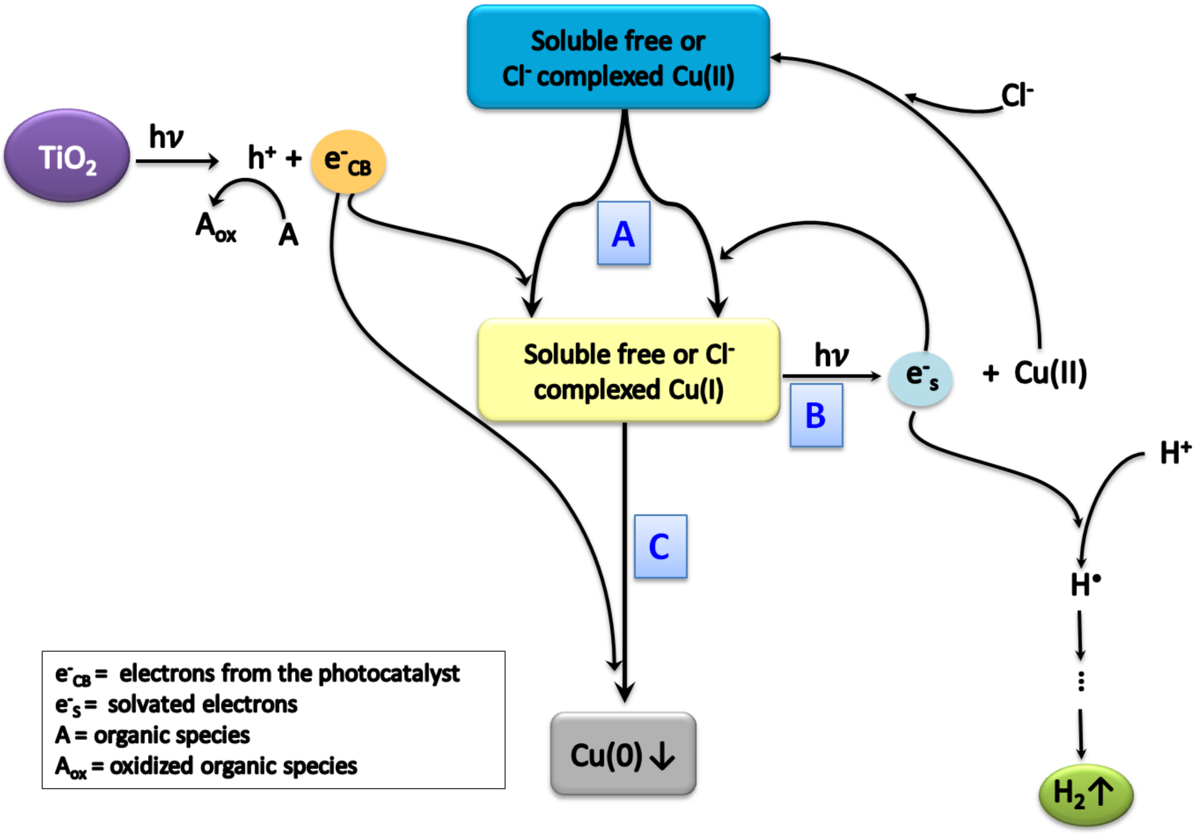

Figure 8.10: Schematic illustration of the reaction mechanism for the investigated system.

Hydrogen formation in a system containing copper in the initial form of cupric ions is strictly connected to the reduction of cupric ions to cuprous ones (Step A, Figure 8.10) and the photolysis of Cu(I)–chloride complexes (Step B, Figure 8.10). In fact, during the photolytic process electrons ($e^{-}{}_{s}$) are ejected into the solution and protons promptly react with them but not with the photogenerated ones ($e^{-}{}_{CB}$). Chloride complexes provide an important reservoir of Cu(I) in solution; therefore, in the presence of low Cl^- concentrations, Cu(I) more easily reduces to Cu(0) which precipitates (Step C, Figure 8.10). When pH is increased, the low proton concentration makes available a higher concentration of solvated electrons which reduce both Cu(II) and Cu(I) and lead to the deposition of a black solid, formed by zero-valent copper (Step C, Figure 8.10).

8.7 Summary

The present investigation proposes a new process for hydrogen generation through the system cupric ions/formic acid/chloride ions/nano-TiO_2/UV radiation. The efficiency of the process in terms of hydrogen production was studied at varying the initial concentrations of formic acid, chloride and cupric ion and pH.

Hydrogen generation revealed similar dependences on formic acid and chloride ion concentrations. The rate of hydrogen production increases up to a formic acid concentration of 10^3 mM. On the other hand, a huge decrease in the maximum value of hydrogen production rate was observed for a formic acid concentration equal to $5.0 \cdot 10^3$ mM, with a contemporary precipitation of zero-valent copper. With regard to chloride ions in solution, an increase in hydrogen generation rate was recorded up to a chloride concentration of 10^3 mM, with a clear decrease for higher concentrations.

Hydrogen production is also strongly dependent on cupric ion concentration. Initial increases in cupric ion concentration resulted in a reduction of hydrogen generation rate. An early loss of reactivity of the system was recorded during the run at the lowest value of cupric ion tested (2.5 mM), with a complete precipitation of cupric ions as zero-valent copper within a reaction time of 300 minutes. A similar behavior was observed for higher starting concentration of cupric ion, but at longer reaction times. No re-oxidation of zero-valent copper was observed in the complete system during the present investigation.

The increase in pH of the solution from 1.0 to 2.5 to 4.0 resulted in a decrease in hydrogen generation rate and the precipitation of zero-valent copper.

A consistent reaction mechanism able to predict the system behavior under different operating conditions was proposed.

9. Conclusions

Hydrogen is considered as an important green energy carrier for the future, due to its high energy content and the absence of greenhouse gas emissions from its combustion.

At present hydrogen production is mainly based on techniques involving fossil fuels with resulting production of toxic gases. An appealing alternative exploits the possibility to produce hydrogen by photocatalytic processes based on solar energy and water or organic species contained in industrial or urban wastewaters. Such processes have the merit to allow simultaneous water decontamination and energy production starting from a fully renewable energy source, the solar radiation.

An intense scientific activity was recorded, mainly during the last years, in the field of photocatalytic reforming of organics to generate hydrogen over copper-based TiO_2 photocatalysts. Researchers pointed out the capability of the incorporated copper species, alone or in cooperation with the second co-catalyst, to (1) effectively separate the electron-hole pairs, thus reducing the occurrence of the recombination reaction, and (2) extend the light absorption to the visible range of the solar spectrum.

The photocatalytic generation of hydrogen from different oxygenated organic species (mostly alcohols and carboxylic acids) through the adoption of copper-modified TiO_2 catalysts was therefore investigated in this study. Photocatalysts were prepared *in situ* by means of a photodeposition procedure. A thorough catalyst characterization supported the deposition on TiO_2 surface of zero-valent copper nanoparticles, which markedly enhances the photoefficiency for hydrogen generation with respect to bare titanium dioxide catalysts.

Depending on the organic species adopted as sacrificial agents, remarkable differences in hydrogen production were recorded. To explain this behavior, a mechanism based on a different oxidation capability of the organics related to their tendency to adsorb on the catalyst surface was proposed. When the species strongly adsorb (i.e, methanol, glycerol and formic acid) beneficial effects are observed in terms of an additional hydrogen generation with respect to bare titanium dioxide. Indeed, a negligible proton reduction occurs in the case of a weak adsorption by the organic species.

The effect of adopting different crystallographic phases of TiO_2 (anatase, rutile and anatase/rutile) on hydrogen generation was also investigated. In particular, the photoactivity for hydrogen generation of undoped commercial TiO_2 photocatalysts and zero-valent copper doped TiO_2 using methanol or glycerol as sacrificial species was studied. Experimental results indicate that the polymorphic composition of the titania adopted has a marked influence on the photoactivity for both the groups of materials. The photocatalytic activity of undoped and copper-doped materials had the following order: P25 ≫ bare anatase ≅ bare rutile, which can be explained in terms of (*i*) relative photogenerated charge carrier concentration on the surface, (ii) titania and metal copper nanoparticles sizes, and (iii) amount of superficial hydroxyl groups. Such theory was supported by a thorough catalyst including X-Ray diffraction, Dynamic Light Scattering, Thermogravimetry, Energy-dispersive X-ray Spectroscopy, FT-IR and Diffuse Reflectance UV Spectroscopies, Photolumincesce, High Resolution Transmission Electron Microscope, Field Emission Scanning Electron Microscopy analyses.

Starting from the mass balance equations for the main species involved in the photocatalytic process, a kinetic model was developed with the aim of simulating hydrogen generation by photoreforming of selected organics over metal-copper modified TiO_2 nanoparticles prepared *in situ*. The model analyzed data collected during the experimental campaign at various substrate (methanol and glycerol) concentrations and catalyst loads.

As a result, the best values of unknown parameters were estimated, such as (*i*) the rate of hole-capture and (*ii*) the adsorption equilibrium constants for both methanol and glycerol, (*iii*) the primary quantum yield and (*iv*) the rate constant for electron-hole recombination on the nanocopper modified-TiO_2. From the values found for these parameters it can be stated that a decrease in the recombination reaction occurs for the catalyst adopted with respect to bare TiO_2, thus indicating the fundamental role played by copper nanoparticles on TiO_2 surface in trapping photogenerated electrons and therefore improving hydrogen generation.

The simultaneous presence in the aqueous matrix of an inorganic ion, that is chloride, was also investigated when formic acid was adopted as sacrificial agent. The efficiency of the process in terms of hydrogen production was studied at varying the initial concentrations of formic acid, chloride and cupric ion and pH. Hydrogen generation revealed similar dependences on formic acid and chloride ion concentrations. For such variables, maximum values were assessed beyond which a decrease in photoefficiency for hydrogen production was recorded. An optimum range of values for the starting cupric ion concentration was also assessed. Moreover, the increase in pH of the solution resulted in a decrease in hydrogen generation rate and the precipitation of zero-valent copper. A consistent reaction mechanism able to predict the system behavior under different operating conditions was proposed.

This work opens the way to the development of new competitive processes able to use waste organic streams for hydrogen generation through low-cost photocatalytic system based on solar energy.

Appendix

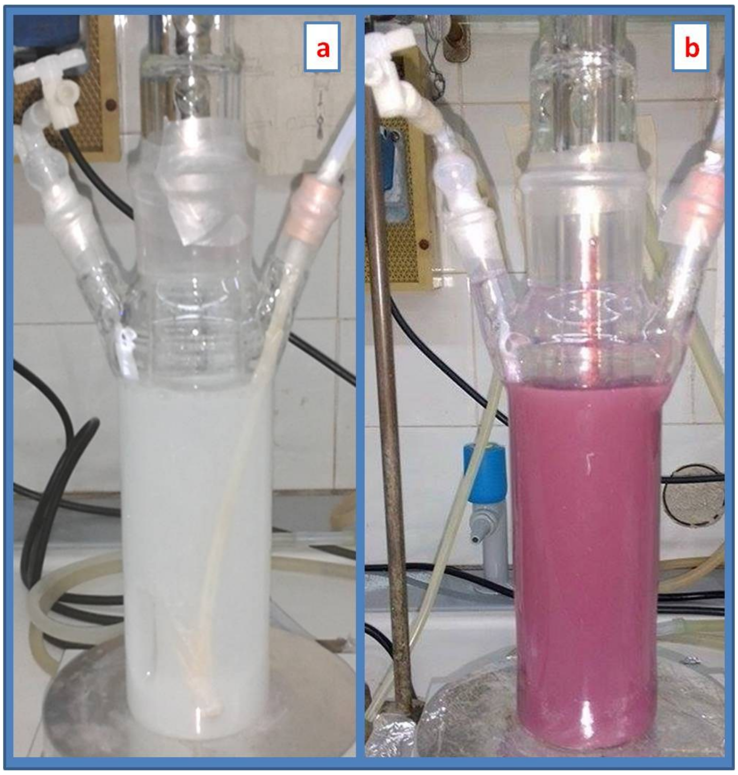

Figure A1: (a) Appearance of the reacting solution ($[C_3H_8O_3]_o$=0.8 M; TiO_2-P25 load = 500 mg•L^{-1}; pH_o=6.4) at zero time in absence of copper. (b) Aspect of the same reacting solution after 120 min of photocatalytic treatment under de-aerated conditions in presence of copper ($[Cu(II)]_o$=0.8 mM).

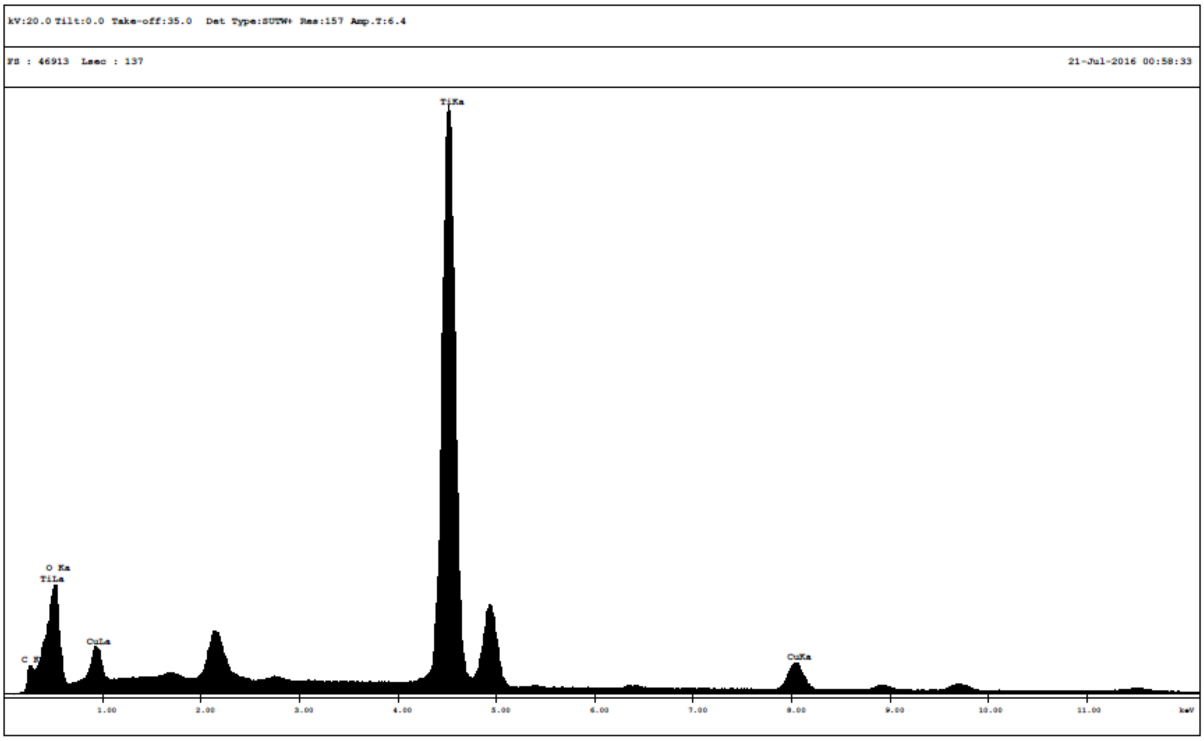

Figure A2: EDX spectrum of TiO_2-P25 and Cu catalyst samples.

References

[1] Muradov NZ, Veziroğlu TN. Green path from fossil-based to hydrogen economy: An overview of carbon-neutral technologies. International Journal of Hydrogen Energy 33 (2008) 6804–39.

[2] Ni M, Leung MKH, Sumathy K, Leung DYC. Potential of renewable hydrogen production for energy supply in Hong Kong. International Journal of Hydrogen Energy 31 (2006) 1401–12.

[3] Kalamaras CM, Efstathiou AM. Hydrogen Production Technologies: Current State and Future Developments. Conference Papers in Energy 2013 (2013) 1–9.

[4] Maeda K. Photocatalytic water splitting using semiconductor particles: History and recent developments. Journal of Photochemistry and Photobiology C: Photochemistry Reviews 12 (2011) 237–68.

[5] Ullmann's Encyclopedia of Industrial Chemistry, 2016. Wiley-VCH Verlag, Weinheim, Germany.

[6] Kothari R Buddhi D Sawhney RL. Comparison of environmental and economic aspects of various hydrogen production methods. Renewable and Sustainable Energy Reviews 12 (2008) 553–563.

[7] Holladay JD, Hu J, King DL, Wang Y. An overview of hydrogen production technologies. Catalysis Today 139 (2009) 244–260.

[8] Molino A, Chianese S, Musmarra D. Biomass gasification technology: The state of the art overview. Journal of Energy Chemistry 25 (2016) 20–25.

[9] Steinfeld A. Solar thermochemical production of hydrogen - a review. Solar Energy 78 (2005) 603–615.

[10] Wang Z, Roberts ZZ, Naterer GF, Gabriel KS. Comparison of thermochemical, electrolytic, photoelectrolytic and photochemical solar-to-hydrogen production technologies. International Journal of Hydrogen Energy 37 (2012) 16287–16301.

[11] Ahmad H, Kamarudin SK, Minggu LJ, Kassim M. Hydrogen from photo-catalytic water splitting process: A review. Renewable and Sustainable Energy Reviews 43 (2015) 599–610.

[12] Puga AV. Photocatalytic production of hydrogen from biomass-derived feedstocks. Coordination Chemistry Reviews 315 (2016) 1–66.

[13] Ni M, Leung MKH, Leung DYC, Sumathy K. A review and recent developments in photocatalytic water-splitting using TiO_2 for hydrogen production. Renewable and Sustainable Energy Reviews 11 (2007) 401–25.

[14] Abe R. Recent progress on photocatalytic and photoelectrochemical water splitting under visible light irradiation. Journal of Photochemistry and Photobiology C: Photochemistry Reviews 11 (2010) 179 –209.

[15] Puga, AV. Photocatalytic production of hydrogen from biomass-derived feedstocks. Coordination Chemistry Reviews 315 (2016) 1–66.

[16] Colmenares JC, Luque R. Heterogeneous photocatalytic nanomaterials: Prospects and challenges in selective transformations of biomass-derived compounds. Chemical Society Reviews 43 (2014) 765–778.

[17] Lianos P. Production of electricity and hydrogen by photocatalytic degradation of organic wastes in a photoelectrochemical cell: the concept of the Photofuelcell: a review of a re-emerging research field. Journal of Hazardous Materials 185 (2011) 575–90.

[18] Chen X, Shen S, Guo L, Mao SS. Semiconductor-based Photocatalytic Hydrogen Generation. Chemical Reviews 110 (2010) 6503–70.

[19] Abe R, Sayama K, Sugihara H. Development of New Photocatalytic Water Splitting into H_2 and O_2 using Two Different Semiconductor Photocatalysts and a Shuttle Redox Mediator IO_3^-/I^-. Journal of Phisical Chemistry B 109 (2005) 16052-61.

[20] Linic S, Christopher P, Ingram DB. Plasmonic-metal nanostructures for efficient conversion of solar to chemical energy. Nature Materials 10 (2011) 911-21.

[21] Walsh A, Yan Y, Huda MN, Al-Jassim MM, Wei SH. Band Edge Electronic Structure of $BiVO_4$: Elucidating the Role of the Bi s and V d Orbitals. Chemistry of Materials 21 (2009) 547–51.

[22] Zhang X, Chen YL, Liu RS, Tsai DP. Plasmonic photocatalysis. Reports On Progress In Physics 76 (2013) 046401.

[23] Kotoulas I, Schizodimou A, Kyriacou G. Electrochemical Reduction of Formic Acid on a Copper-Tin-Lead Cathode. The Open Electrochemistry Journal 5 (2013) 8–12.

[24] Grätzel M. Photoelectrochemical Cells. Nature 414 (2001) 338–44.

[25] Gomathisankar P, Hachisuka K, Katsumata H, Suzuki T, Funasaka K, Kaneco S. Enhanced photocatalytic hydrogen production from aqueous methanol solution using ZnO with simultaneous photodeposition of Cu. International Journal of Hydrogen Energy 38 (2013) 11840–6.

[26] Kaneko M, Okura I. Photocatalysis: Science and technology. Kodansha Cooperation Ltd.; 2002.

[27] Grimes CA, Varghese OK, Ranjan S. Solar Light, Water, Hydrogen: The Solar Generation of Hydrogen by Water Photoelectrolysis. New York: Springer; 2008.

[28] Bamwenda GR, Tsubota S, Nakamura T, Haruta M. Photoassisted hydrogen production from a water-ethanol solution: a comparison of activities of Au-TiO_2 and Pt-TiO_2. Journal of Photochemistry and Photobiology A 89 (1995) 177–89.

[29] Kondarides DI, Daskalaki VM, Patsoura A, Verykios XE, Hydrogen Production by Photo-Induced Reforming of Biomass Components and Derivatives at Ambient Conditions, Catalysis Letters 122 (2008) 26–32.

[30] Nada AA, Hamed HA, Barakat MH, Mohamed NR, Veziroglu TN. Enhancement of photocatalytic hydrogen production rate using photosensitized TiO_2/RuO_2-MV^{2+}. International Journal of Hydrogen Energy 33 (2008) 3264–69.

[31] Khan SUM, Al-Shahry M, Ingler WB. Efficient Photochemical Water Splitting by a Chemically Modified n-TiO_2. Science 297 (2002) 2243–5.

[32] Dholam R, Patel N, Adami M, Miotello A. Hydrogen production by photocatalytic water-splitting using Cr- or Fe-doped TiO_2 composite thin films photocatalyst. International Journal of Hydrogen Energy 34 (2009) 5337–46.

[33] Choi SK, Yang HS, Kim JH, Park H. Organic dye-sensitized TiO_2 as a versatile photocatalyst for solar hydrogen and environmental remediation. Applied Catalysis B: Environmental 121–2 (2012) 206–13.

[34] Chen Y, Mou Z, Yin S, Huang H, Yang P, Wang X. Graphene enhanced photocatalytic hydrogen evolution performance of dye-sensitized TiO_2 under visible light irradiation. Materials Letters 107 (2013) 31–4.

[35] Kait CF, Nurlaela E, Dutta BK. Solar Hydrogen from Glycerol-Water Mixture. Recent advances in environment, energy, ecosystems and development. Proceedings of the 2013 International Conference on Environment, Energy, Ecosystems and Development (2013) 48–52.

[36] Holman JS, Stone P. Chemistry, Second Edition, Nelson Thornes, Cheltenham, 2001.

[37] Clarizia L, Spasiano D, Di Somma I, Marotta R, Andreozzi R, Dionysiou DD. Copper modified-TiO_2 catalysts for hydrogen generation through photoreforming of organics. A short review. International Journal of Hydrogen Energy 39 (2014) 16812–16831.

[38] Sahu M, Biswas P. Single-step processing of copper-doped titania nanomaterials in a flame aerosol reactor. Nanoscale Research Letters 6 (2011) 441.

[39] Choudhury B, Dey M, Choudhury A. Defect generation, d-d transition, and band gap reduction in Cu-doped TiO_2 nanoparticles. International Nano Letters 3 (2013) 25–32.

[40] Zhang J, Zhu H, Zheng S, Pan F, Wang T. TiO_2 Film/Cu_2O microgrid heterojunction with photocatalytic activity under solar light irradiation. ACS Applied Materials & Interfaces 1 (2009) 2111–2114.

[41] Lanese V, Spasiano D, Marotta R, Di Somma I, Lisi L, Cimino S et al. Hydrogen production by photoreforming of formic acid in aqueous copper/TiO_2 suspensions under UV-simulated solar radiation at room temperature. International Journal of Hydrogen Energy 38 (2013) 9644–54.

[42] Xu S, Ng J, Du AJ, Liu J, Sun DD. Highly efficient TiO_2 nanotube photocatalyst for simultaneous hydrogen production and copper removal from water. International Journal of Hydrogen Energy 36 (2011) 6538–45.

[43] Lalitha K, Sadanandam G, Kumari VD, Subrahmanyam M, Sreedhar B, Hebalkar NY. Highly Stabilized and Finely Dispersed Cu_2O/TiO_2: A Promising Visible Sensitive Photocatalyst for Continuous Production of Hydrogen from Glycerol:Water Mixtures. The Journal of Physical Chemistry C 114 (2010) 22181–9.

[44] Chen CS, You JH, Lin JH, Chen YY. Effect of highly dispersed active sites of Cu/TiO_2 catalyst on CO oxidation. Catalysis Communications 9 (2008) 2381–5.

[45] Jung M, Ng YH, Jiang Y, Scott J, Amal R. Active Cu species in Cu/TiO_2 for photocatalytic hydrogen evolution. Chemeca 2013 (41st : 2013 : Brisbane, Qld.). Chemeca 2013: Challenging Tomorrow. Barton, ACT: Engineers Australia (2013) 214–7.

[46] Zhang S, Peng B, Yang S, Fang Y, Peng F. The influence of the electrodeposition potential on the morphology of Cu_2O/TiO_2 nanotube arrays and their visible-light-driven photocatalytic activity for hydrogen evolution. International Journal Of Hydrogen Energy 38 (2013) 13866–71.

[47] Heciak A, Morawski AW, Grzmil B, Mozia S. Cu-modified TiO_2 photocatalysts for decomposition of acetic acid with simultaneous formation of C1–C3 hydrocarbons and hydrogen. Applied Catalysis B: Environmental 140–1 (2013) 108– 114.

[48] Yu Z, Meng J, Li Y, Li Y. Efficient photocatalytic hydrogen production from water over a CuO and carbon fiber comodified TiO_2 nanocomposite photocatalyst. International Journal Of Hydrogen Energy 38 (2013) 16649–55.

[49] Wang B, Sun Q, Liu S, Li Y. Synergetic catalysis of CuO and graphene additives on TiO_2 for photocatalytic water splitting. International Journal Of Hydrogen Energy 38 (2013) 7232–40.

[50] Miwa T, Kaneco S, Katsumata H, Suzuki T, Ohta K, Verma SC et al. Photocatalytic hydrogen production from aqueous methanol solution with $CuO/Al_2O_3/TiO_2$ nanocomposite. International Journal of Hydrogen Energy 35 (2010) 6554– 60.

[51] Yu J, Hai Y, Jaroniec M. Photocatalytic hydrogen production over CuO-modified titania. Journal of Colloid and Interface Science 357 (2011) 223–228.

[52] Khemthong P, Photai P, Grisdanurak N. Structural properties of CuO/TiO_2 nanorod in relation to their catalytic activity for simultaneous hydrogen production under solar light. International Journal of Hydrogen Energy 38 (2013) 15992–6001.

[53] Chang FW, Ou TC, Roselin LS, Chen WS, Lai SC, Wu HM. Production of hydrogen by partial oxidation of methanol over bimetallic Au–Cu/TiO_2–Fe_2O_3 catalysts. Journal of Molecular Catalysis A: Chemical 313 (2009) 55–64.

[54] Yoong LS, Chong FK, Dutta BK. Development of copper-doped TiO_2 photocatalyst for hydrogen production under visible light. Energy 34 (2009) 1652–61.

[55] Chen WT, Jovic V, Sun-Waterhouse D, Idriss H, Waterhouse GIN. The role of CuO in promoting photocatalytic hydrogen production over TiO_2. International Journal of Hydrogen Energy 38 (2013) 15036–15048.

[56] Dang H, Dong X, Dong Y, Zhang Y, Hampshire S. TiO_2 nanotubes coupled with nano-$Cu(OH)_2$ for highly efficient photocatalytic hydrogen production. International Journal of Hydrogen Energy 38 (2013) 2126–35.

[57] Wang Q, An N, Bai Y, Hang H, Li J, Lu X et al. High photocatalytic hydrogen production from methanol aqueous solution using the photocatalysts CuS/TiO_2. International Journal Of Hydrogen Energy 38 (2013) 10739–45.

[58] Lee SS, Bai H, Liu Z, Sun DD. Novel-structured electrospun TiO_2/CuO composite nanofibers for high efficient photocatalytic cogeneration of clean water and energy from dye wastewater. Water Research 47 (2013) 4059–73.

[59] Lee SS, Bai H, Liu Z, Sun DD. Optimization and an insightful properties—Activity study of electrospun TiO_2/CuO composite nanofibers for efficient photocatalytic H_2 generation. Applied Catalysis B: Environmental 140–141 (2013) 68–81.

[60] Xu S, Ng J, Zhang X, Bai H, Sun DD. Fabrication and comparison of highly efficient Cu incorporated TiO_2 photocatalyst for hydrogen generation from water. International Journal of Hydrogen Energy 35 (2010) 5254–61.

[61] Sreethawong T, Yoshikawa S. Comparative investigation on photocatalytic hydrogen evolution over Cu-, Pd-, and Au-loaded mesoporous TiO_2 photocatalysts. Catalysis Communications 6 (2005) 661–8.

[62] Montini T, Gombac V, Sordelli L, Delgado JJ, Chen X, Adami G et al. Nanostructured Cu/TiO_2 Photocatalysts for H_2 Production from Ethanol and Glycerol Aqueous Solutions. ChemCatChem 3 (2011) 574–7.

[63] Kezzim A, Nasrallah N, Abdi A, Trari M. Visible light induced hydrogen on the novel hetero-system $CuFe_2O_4$/TiO_2. Energy Conversion and Management 52 (2011) 2800–6.

[64] Gombac V, Sordelli L, Montini T, Delgado JJ, Adamski A, Adami G et al. CuO_x-TiO_2 Photocatalysts for H_2 Production from Ethanol and Glycerol Solutions. The Journal of Physical Chemistry 114 (2010) 3916–25.

[65] Ampelli C, Passalacqua R, Genovese C, Perathoner S, Centi G, Montini T et al. Solar Energy and Biowaste Conversion into H_2 on CuO_x/TiO_2 Nanocomposites. Chemical Engineering Transactions 35 (2013) 583–8.

[66] Choi HJ, Kang M. Hydrogen production from methanol/water decomposition in a liquid photosystem using the anatase structure of Cu loaded TiO_2. International Journal of Hydrogen Energy 32 (2007) 3841–8.

[67] Li Z, Liu J, Wang D, Gao Y, Shen J. $Cu_2O/Cu/TiO_2$ nanotube Ohmic heterojunction arrays with enhanced photocatalytic hydrogen production activity. International Journal of Hydrogen Energy 37 (2012) 6431–7.

[68] Wu NL, Lee MS. Enhanced TiO_2 photocatalysis by Cu in hydrogen production from aqueous methanol solution. International Journal of Hydrogen Energy 2004;29:1601–5

[69] Zhang S, Wang H, Yeung M, Fang Y, Yu H, Peng F. $Cu(OH)_2$-modified TiO_2 nanotube arrays for efficient photocatalytic hydrogen production. International Journal Of Hydrogen Energy 38 (2013) 7241–5.

[70] Wang C, Hu Q, Huang J, Zhu C, Deng Z, Shi H et al. Enhanced hydrogen production by water splitting using Cu-doped TiO_2 film with preferred (0 0 1) orientation. Applied Surface Science 292 (2013) 161–4.

[71] Bolton J. Solar Photoproduction of Hydrogen: a Review. Solar Energy 57 (1996) 37–50.

[72] Abe R, Sayama K, Arakawa H. Efficient hydrogen evolution from aqueous mixture of I^- and acetonitrile using a merocyanine dye-sensitized Pt/TiO_2 photocatalyst under visible light irradiation. Chemical Physics Letters 362 (2002) 441–4.

[73] Konta R, Ishii T, Kato H, Kudo A. Photocatalytic Activities of Noble Metal Ion Doped SrTiO3 under Visible Light Irradiation. The Journal of Physical Chemistry B 108 (2004) 8992–5.

[74] Astuti Y, Palomares E, Haque SA, Durrant JR. Triplet State Photosensitization of Nanocrystalline Metal Oxide Electrodes by Zinc-Substituted Cytochrome c: Application to Hydrogen Evolution. Journal of the American Chemical Society 127 (2005) 15120–6.

[75] Rivas FJ, Beltrán FJ, Frades J, Buxeda P. Oxidation of p-hydroxybenzoic acid by Fenton's reagent. Water Research 35 (2001) 387–96.

[76] Lopez A, Pagano M, Volpe A, Di Pinto AC. Fenton’s pre-treatment of mature landfill leachate. Chemosphere 54 (2004) 1005–10.

[77] Primo O, Rivero MJ, Ortiz I. Photo-Fenton process as an efficient alternative to the treatment of landfill leachates. Journal of Hazardous Materials 153 (2008) 834–42.

[78] Kim KH, Ihm SK. Heterogeneous catalytic wet air oxidation of refractory organic pollutants in industrial wastewaters: A review. Journal of Hazardous Materials 186 (2011) 16–34.

[79] Robinson T, McMullan G, Marchant R, Nigam P. Remediation of dyes in textile effluent: a critical review on current treatment technologies with a proposed alternative. Bioresource Technology 77 (2001) 247–55.

[80] Saratale RG, Saratale GD, Chang JS, Govindwar SP. Bacterial decolorization and degradation of azo dyes: A review. Journal of the Taiwan Institute of Chemical Engineers 42 (2011) 138–57.

[81] Mcginnis BD, Adams VD, Middlebrooks EJ. Degradation of ethylene glycol in photo Fenton systems. Water Research 34 (2000) 2346–54.

[82] Brahimi R, Bessekhouad Y, Bouguelia A, Trari M. $CuAlO_2/TiO_2$ heterojunction applied to visible light H_2 production. Journal of Photochemistry and Photobiology A: Chemistry 186 (2007) 242–7.

[83] Korzhak AV, Ermokhina NI, Stroyuk AL, Bukhtiyarov VK, Raevskaya AE, Litvin VI et al. Photocatalytic hydrogen evolution over mesoporous TiO_2/metal nanocomposites. Journal of Photochemistry and Photobiology A: Chemistry 198 (2008) 126–34.

[84] Vohra MS, Selimuzzaman SM, Al-Suwaiyan MS. Aqueous Phase Thiosulfate Removal Using Photocatalysis. International Journal of Environmental Research 5 (2011) 247–54.

[85] Pelaez M, Nolan NT, Pillai SC, Seery MK, Falaras P, Kontos AG et al. A Review on the Visible Light Active Titanium Dioxide Photocatalysts for Environmental Applications. Applied Catalysis B: Environmental 125 (2012) 331–49.

[86] Bandara J, Udawatta CPK, Rajapakse CSK. Highly stable CuO incorporated TiO_2 catalyst for photocatalytic hydrogen production from H_2O. Photochemical & Photobiological Sciences 4 (2005) 857–61.

[87] Jeon MK, Park JW, Kang M. Hydrogen Production from Methanol/Water Decomposition in a Liquid Photosystem Using the Anatase and Rutile Forms of Cu-TiO_2. Journal of Industrial and Engineering Chemistry 13 (2007) 84–91.

[88] Simamora AJ, Hsiung TL, Chang FC, Yang TC, Liao CY, Wang HP. Photocatalytic splitting of seawater and degradation of methylene blue on CuO/nano TiO_2. International Journal of Hydrogen Energy 37 (2012) 13855–8.

[89] Colón G, Maicu M, Hidalgo MC, Navío JA. Cu-doped TiO_2 systems with improved photocatalytic activity. Applied Catalysis B: Environmental 67 (2006) 41–51.

[90] Sakata Y, Yamamoto T, Okazaki T, Imamura H, Tsuchiya S. Generation of visible light response on the photocatalyst of a copper ion containing TiO_2. Chemistry Letters 12 (1998) 1253–4.

[91] Yasomanee JP, Bandara J. Multi-electron storage of photoenergy using Cu_2O–TiO_2 thin film photocatalyst. Solar Energy Materials and Solar Cells 92 (2008) 348–52.

[92] Ou TC, Chang FW, Roselin LS. Production of hydrogen via partial oxidation of methanol over bimetallic Au–Cu/TiO_2 catalysts. Journal of Molecular Catalysis A: Chemical 293 (2008) 8–16.

[93] Xu S, Sun DD. Significant improvement of photocatalytic hydrogen generation rate over TiO_2 with deposited CuO. International Journal of Hydrogen Energy 34 (2009) 6096–104.

[94] Li L, Zhang M. Preparation, Characterization, and Photocatalytic Property of Cu_2O-TiO_2 Nanocomposites. International Journal of Photoenergy 2012 (2012) 1–4.

[95] Li L, Xu L, Shi W, Guan J. Facile preparation and size-dependent photocatalytic activity of Cu_2O nanocrystals modified titania for hydrogen evolution. International Journal of Hydrogen Energy 38 (2013) 816–22.

[96] Xiong L, Yang F, Yan L, Yan N, Yang X, Qiu M et al. Bifunctional photocatalysis of TiO_2/Cu_2O composite under visible light: Ti^{3+} in organic pollutant degradation and water splitting. Journal of Physics and Chemistry of Solids 72 (2011) 1104–9.

[97] Yan J, Zhang L, Yang H, Tang Y, Lu Z, Guo S et al. $CuCr_2O_4$/TiO_2 heterojunction for photocatalytic H_2 evolution under simulated sunlight irradiation. Solar Energy 83 (2009) 1534–9.

[98] Jin Z, Zhang X, Li Y, Li S, Lu G. 5.1% apparent quantum efficiency for hydrogen generation over Eosine-sensitized CuO/TiO_2 photocatalyst under visible light irradiation. Catalysis Communications 8 (2007) 1267–73.

[99] Batzill M, Morales EH, Diebold U. Influence of nitrogen doping on the defect formation and surface properties of TiO_2 rutile and anatase. Physical Review Letters 96 (2006) 026103.

[100] Asahi R, Morikawa T, Ohwaki T, Aoki K, Taga Y. Visible-Light Photocatalysis in Nitrogen-Doped Titanium Oxides. Science 293 (2001) 269–71.

[101] Kim CS, Shin JW, Cho YH, Jang HD, Byun HS, Kim TO. Synthesis and characterization of Cu/N-doped mesoporous TiO_2 visible light photocatalysts. Applied Catalysis A: General 455 (2013) 211–8.

[102] Taylor S, Mehta M, Samokhvalov A. Production of hydrogen by glycerol photoreforming using binary nitrogen-metal-promoted N-M-TiO_2 photocatalysts. Chemphyschem 15 (2014) 942–9.

[103] Canterino M, Di Somma I, Marotta R , Andreozzi R. Kinetic investigation of Cu(II) ions photoreduction in presence of titanium dioxide and formic acid. Water Research 42 (2008) 4498–506.

[104] Xu S, Du AJ, Liu J, Ng J, Sun DD. Highly efficient CuO incorporated TiO_2 nanotube photocatalyst for hydrogen production from water. International Journal of Hydrogen Energy 36 (2011) 6560–8.

[105] Saadi S, Bouguelia A, Trari M. Photoassisted hydrogen evolution over spinel CuM_2O_4 (M = Al, Cr, Mn, Fe and Co). Renewable Energy 31 (2006) 2245–56.

[106] Koriche N, Bouguelia A, Aider A, Trari M. Photocatalytic hydrogen evolution over delafossite $CuAlO_2$. International Journal of Hydrogen Energy 30 (2005) 693–9.

[107] Wu Y, Lu G, Li S. The Role of Cu(I) Species for Photocatalytic Hydrogen Generation Over CuO_x/TiO_2. Catalysis Letters 133 (2009) 97–105.

[108] Cheng P, Li W, Zhou T, Jin Y, Gu M. Physical and photocatalytic properties of zinc ferrite doped titania under visible light irradiation. Journal of Photochemistry and Photobiology A: Chemistry 168 (2004) 97–101.

[109] Bricker CE and Aubrey Vail W. Microdetermination of formaldehyde with chromotropic Acid, Analytical Chemistry 22 (1950) 720–722.

[110] Kum JM, Park YJ, Kim HJ, Cho SO. Plasmon-enhanced photocatalytic hydrogen production over visible-light responsive Cu/TiO_2. Nanotechnology 26 (2015) 125402–125407.

[111] Tung RT. Chemical bonding and Fermi level pinning at metal semiconductor interfaces. Physical Review Letters 84 (2000) 6078–81.

[112] Liu L, Yang W, Li Q, Gao S, Shang JK. Synthesis of Cu_2O nanospheres decorated with TiO_2 nanoislands, their enhanced photoactivity and stability under visible light illumination, and their post-illumination catalytic memory. ACS Applied Materials & Interfaces 6 (2014) 5629–5639.

[113] Hara M, Kondo T, Komoda M, Ikeda S, Shinohara K, Tanaka A, Kondo JN and Domen K. Cu_2O as a photocatalyst for overall water splitting under visible light irradiation. Chemical Communications 3 (1998) 357–358.

[114] Shao F, Sun J, Gao L, Luo J, Liu Y, Yang S. High efficiency semiconductor-liquid junction solar cells based on Cu/Cu_2O. Advanced Functional Materials 22 (2012) 3907–3913.

[115] Lopez R, Gomez R. Band-gap energy estimation from diffuse reflectance measurements on sol–gel and commercial TiO_2: a comparative study. Journal of Sol-Gel Science and Technology 61 (2012) 1–7.

[116] Pestryakov AN, Petranovskii VP, A. Kryazhov A, O. Ozhereliev O, Pfänder N, Knop Gericke A. Study of copper nanoparticles formation on supports of different nature by UV–Vis diffuse reflectance spectroscopy. Chemical Physics Letters 385 (2004) 173–176.

[117] Wu LL, Tsui LK, Swami N, Zangari GJ. Photoelectrochemical Stability of Electrodeposited Cu_2O Films. The Journal of Physical Chemistry C 114 (2010) 11551−11556.

[118] Nosaka Y, Takahashi S, Sakamoto H, Nosaka AY. Reaction mechanism of Cu(II)-grafted visible-light responsive TiO_2 and WO_3 photocatalysts studied by means of ESR

spectroscopy and chemiluminescence photometry. The Journal of Physical Chemistry C 115 (2011) 21283–21290.

[119] Linsebigler AL, Lu G, Yates JT. Photocatalysis on TiO_2 surfaces: principles, mechanisms and selected results. Chemical Reviews 95 (1995) 735–758.

[120] Delk FS, Vavere A. Infrared observations of Rh NCO and Si NCO species formed during the reduction of NO by CO over silica-supported rhodium. Journal of Catalysis 85 (1984) 380–388.

[121] Ferguson MA, Hoffmann MR, Hering JG. TiO_2-Photocatalyzed As(III) Oxidation in queous Suspensions: Reaction Kinetics and Effects of Adsorption. Environmental Science & Technology 39 (2005) 1880–1886

[122] Di Somma I, Clarizia L, Satyro S, Spasiano D, Marotta R, Andreozzi R. A kinetic study of simultaneous removal of EDDS and cupric ions from acidic aqueous solutions by TiO_2-based photocatalysis under artificial solar light irradiation and deaerated batch conditions, Chemical Engineering Journal 270 (2015) 519–527.

[123] Sun Y, Pignatello JJ. Evidence for a Surface Dual Hole- Radical Mechanism in the TiO_2 Photocatalytic Oxidation of 2,4-Dichlorophenoxyacetic Acid. Environmental Science & Technology 29 (1995) 2065-2072.

[124] Kaise M, Kondoh HH, Nishihara C, Nozoye H, Shindo H, Nimuraband S, Kikuchi O. Photocatalytic reactions of acetic acid on platinum-loaded TiO_2: ESR evidence of radical intermediates in the photo-Kolbe reaction. Journal of the Chemical Society, Chemical Communications 4 (1993) 395-396.

[125] Wen B, Li Y, Chen C, Ma W, Zhao J. An unexplored O_2-involved pathway for the decarboxylation of saturated carboxylic acids by TiO_2 photocatalysis: an isotopic probe study. Chemistry - A European Journal 16 (2010) 11859–11866.

[126] Sakata T, Kawai T, Hashimoto K. Heterogeneous photocatalytic reactions of organic acids and water. New reaction paths besides the photo-Kolbe reaction. The Journal of Physical Chemistry 88 (1984) 2344–2350.

[127] Krysa J, Waldner G, Mestankova H, Jirkovsky J, Grabner G. Photocatalytic degradation of model organic pollutants on an immobilized particulate TiO_2 layer. Roles of adsorption processes and mechanistic complexity, Applied Catalysis B: Environmental 64 (2006) 290–301.

[128] Tamaki Y, Furube A, Murai M, Hara K, Katoh R, Tachiya M. Direct observation of reactive trapped holes in TiO_2 undergoing photocatalytic oxidation of adsorbed alcohols: evaluation of the reaction rates and yields. Journal of the American Chemical Society 128 (2006) 416–417.

[129] Chen J, Ollis DF, Rulkens WH, Bruning H. Photocatalyzed oxidation of alcohols and organochlorides in the presence of native TiO_2 and metallized TiO_2 suspensions. Part (II): Photocatalytic mechanisms, Water Research 33 (1999) 669–676.

[130] Clarizia L, Vitiello G, Luciani G, Di Somma I, Andreozzi R, Marotta R. In-situ photodeposited nanoCu on TiO_2 as a catalyst for hydrogen production under UV/visible radiation. Applied Catalysis A: General 518 (2016) 142–149.

[131] Li M, Li Y, Peng S, Lu G, Li S. Photocatalytic hydrogen generation using glycerol wastewater over Pt/TiO_2. Frontiers of Chemistry in China 4 (2009) 32–38.

[132] Dimitrijevic NM, Shkrob IA, Gosztola DJ, Rajh T. Dynamics of interfacial charge transfer to formic acid, formaldehyde, and methanol on the surface of TiO_2 nanoparticles and its role in methane production. Journal of Physical Chemistry, C 116 (2012) 878–885.

[133] Chen J, Ollis DF, Rulkens WH, Bruning H. Kinetic processes of photocatalytic mineralization of alcohols on metalized titanium dioxide. Water Research 33 (1999) 1173–1180.

[134] Matthews RW. Kinetics of photocatalytic oxidation of organic solutes over titanium dioxide. Journal of Catalysis 111 (1988) 264–272.

[135] Yurdakal S, Loddo V, Ferrer BB, Palmisano G, Augugliaro V, Farreras JG, Palmisano L. Optical properties of TiO_2 suspensions: influence of pH and powder concentration on mean particle size, Industrial & Engineering Chemistry Research 46 (2007) 7620–7626.

[136] Bideau M, Claudel B, Otterbein M. Photocatalysis of formic acid oxidation by oxygen in aqueous media. Journal of Photochemistry 14 (1980) 291–302.

[137] Mueller R, Kammler HK, Wegner K, Pratsinis SE. OH surface density of SiO_2 and TiO_2 by thermogravimetric analysis. Langmuir 19 (2003) 160–165.

[138] Spasiano D, Marotta R , Gargano I , Di Somma I, Vitiello G, D'Errico G, Andreozzi R. Kinetic modeling of partial oxidation of benzyl alcohol in water by means of Fe(III)/O_2/UV–solar simulated process. Chemical Engineering Journal 249 (2014) 130–142.

[139] Vohra MS, Selimuzzaman SM, Al-Suwaiyan MS. NH_4^+-NH_3 removal from simulated wastewater using UV-TiO_2 photocatalysis: effect of co-pollutants and pH, Environmental Technology 31 (2010) 641–654.

[140] P. Montes-Navajas, M. Serra, A. Corma, H. Garcia, Catalysis Today 225 (2014) 52– 54.

[141] Obregón S, Munoz-Batista MJ, Fernández-García M, Kubacka A, Colón G. Cu–TiO_2 systems for the photocatalytic H_2 production: Influence of structural and surface support feature. Applied Catalysis B: Environmental 179 (2015) 468–478.

[142] Cabrera MI, Alfano OM, Cassano AE, Absorption and Scattering Coefficients of Titanium Dioxide Particulate Suspensions in Water, The Journal of Physical Chemistry 100 (1996) 20043–20050.

[143] Cassano AE, Alfano OM. Reaction engineering of suspended solid heterogeneous photocatalytic reactors. Catalysis Today 58 (2000) 167–197.

[144] Ryu J, Choi W. Substrate-Specific Photocatalytic Activities of TiO_2 and Multiactivity Test for Water Treatment Application. Environmental Science & Technology 42 (2008) 294–300.

[145] Hussain M, Ceccarelli R, Marchisio DL, Fino D, Russo N, Geobaldo F. Synthesis, characterization, and photocatalytic application of novel TiO_2 nanoparticles. Chemical Engineering Journal 157 (2010) 45–51.

[146] Yurdakal S, Palmisano G, Loddo V, Augugliaro V, Palmisano L. Nanostructured Rutile TiO_2 for Selective Photocatalytic Oxidation of Aromatic Alcohols to Aldehydes in Water. Journal of the American Chemical Society 130 (2008) 1568–1569.

[147] Silvestri B, Pezzella A, Luciani G, Costantini A, Tescione F, Branda F. Heparin conjugated silica nanoparticle synthesis. Materials Science and Engineering: C 32 (2012) 2037–2041.

[148] Reddy KM, Manorama SV, Reddy AR. Bandgap studies on anatase titanium dioxide nanoparticles. Materials Chemistry and Physics 78 (2002) 239–245.

[149] Pallotti D, Orabona E, Amoruso S, Maddalena P, Lettieri S. Modulation of mixed-phase titania photoluminescence by oxygen adsorption. Applied Physics Letters 105 (2014) 031903.

[150] Nasr M, Chaaya AA, Abboud N, Bechelany M, Viter R, Eid C, Khoury A, Miele P. Photoluminescence: A very sensitive tool to detect the presence of anatase in rutile phase electrospun TiO_2 nanofibers. Superlattice Microstructures 77 (2015) 18–24.

[151] Ohtani B, Prieto-Mahaney OO, Li D, Abe R. What is Degussa (Evonik) P25? Crystalline composition analysis, reconstruction from isolated pure particles and photocatalytic activity test. Journal of Photochemistry and Photobiology A: Chemistry 216 (2010) 179–182.

[152] Su R, Bechstein R, Sø L, Vang RT, Sillassen M, Esbjornsson B, Palmqvist A, Besenbacher F, How the Anatase-to-Rutile Ratio Influences the Photoreactivity of TiO_2. The Journal of Physical Chemistry, C 115 (2011) 24287–24292.

[153] Da Vià L, Recchi C, Gonzalez-Yañez EO, Davies TE, Lopez-Sanchez JA. Visible light selective photocatalytic conversion of glucose by TiO_2. Applied Catalysis B: Environmental 202 (2017) 281–288.

[154] Chen WT, Chan A, Al-Azri ZHN, Dosado AG, Nadeem MA, Sun-Waterhouse D, H. Idriss H, Waterhouse GIN. Effect of TiO2 polymorph and alcohol sacrificial agent on the activity of Au/TiO2 photocatalysts for H2 production in alcohol–water mixtures. Journal of Catalysis 329 (2015) 499–513.

[155] Hurum DC, Agrios AG, Gray KA, Rajh T, Thurnauer C. Explaining the Enhanced Photocatalytic Activity of Degussa P25 Mixed-Phase TiO_2 Using EPR. The Journal of Physical Chemistry, B 107 (2003) 4545–4549.

[156] C. Mercado, Z. Seeley, A. Bandyopadhyay, S. Bose, J.L. McHale, ACS Applied Materials & Interfaces 3 (2011) 2281–2288.

[157] Mercado CC, Knorr FJ, McHale JL, Usmani SM, Ichimura AS, Saraf LV. Photoluminescence of Dense Nanocrystalline Titanium Dioxide Thin Films: Effect of Doping and Thickness and Relation to Gas Sensing. Journal of Physical Chemistry, C 116 (2012) 10796−10804.

[158] Scanlon DO, Dunnill CW, Buckeridge J, Shevlin SA, Logsdail AJ, Woodley SM, Catlow CRA, Powell MJ, Palgrave RG, Parkin IP, Watson GW, Keal TW, Sherwood PS, Walsh A, Sokol AA. Band alignment of rutile and anatase TiO_2. Nature Materials 12 (2013) 798–801.

[159] Mi Y, Weng Y. Band Alignment and Controllable Electron Migration between Rutile and Anatase TiO_2. Scientific Report 5 (2015) 11482.

[160] Deak P, Aradi B, Frauenheim T. Band Lineup and Charge Carrier Separation in Mixed Rutile-Anatase Systems. The Journal of Physical Chemistry, C 115 (2011) 3443–3446.

[161] Zhao PJ, Wug R, Hou J, Chang AM, Guan F, Zhang B. One-step Self Assemble of Cu-TiO2 Heterogeneous Nanoparticles Using a Soft Template. Journal of Inorganic Materials 27 (2012) 1003–1008.

[162] Maeda K. Z-Scheme Water Splitting Using Two Different Semiconductor Photocatalysts ACS Catalysis 3 (2013) 1486−1503.

[163] Kumar CP, Gopal NO, Wang TC, Wong MS, Ke SC. EPR Investigation of TiO_2 Nanoparticles with Temperature-Dependent Properties. The Journal of Physical Chemistry, B 110 (2006) 5223–5229.

[164] Park NG, van de Lagemaat J, Frank AJ. Comparison of Dye-Sensitized Rutile- and Anatase-Based TiO_2 Solar Cells. The Journal of Physical Chemistry, B 104 (2000) 8989–8994.

[165] Yan J, Wu G, Guan N, Li L, Li Z, Cao X. Understanding the effect of surface/bulk defects on the photocatalytic activity of TiO_2: anatase versus rutile. Physical Chemistry Chemical Physics 15 (2013) 10978–10988.

[166] Liu F, Lu L, Xiao P, He H, Qiao L, Zhang Y. Effect of Oxygen Vacancies on Photocatalytic Efficiency of TiO_2 Nanotubes Aggregation. Bulletin of the Korean Chemical Society 33 (2012) 2255–2259.

[167] Schaub R, Thostrup P, Lopez N, Lægsgaard E, Stensgaard I, Nørskov JK, Besenbacher F. Oxygen Vacancies as Active Sites for Water Dissociation on Rutile TiO_2 (110) Physical Review Letters 87 (2001) 266104-1–4.

[168] Kubacka A, Fernandez-García M, Colon G. Advanced Nanoarchitectures for Solar Photocatalytic Applications, Chemical Reviews 112 (2012) 1555–1614.

[169] Konstantinou M, Pashalidis I. Competitive sorption of Cu(II), Eu(III) and U(VI) ions on TiO2 in aqueous solutions - A potentiometric study. Colloid Surfaces A: Physicochemical and Engineering Aspects 324 (2008) 217‑221.

[170] Boccuzzi F, Chiorino A, Martra G, Gargano M, Ravasio N, Carrozzini B. Preparation, Characterization, and Activity of Cu/TiO_2 Catalysts. I. Influence of the Preparation Method on the Dispersion of Copper in Cu/TiO_2. J. Catal. 165 (1997) 129–139.

[171] Iliev V, Tomova D, Bilyarska L, Tyuliev G. Influence of the size of gold nanoparticles deposited on TiO2 upon the photocatalytic destruction of oxalic acid. Journal of Molecular Catalysis A: Chemical 263 (2007) 32–38.

[172] Khalid NR, Ahmed E, Hong Z, Ahmad M, Zhang Y, Khalid S. Cu-doped TiO_2 nanoparticles/graphene composites for efficient visible-light photocatalysis. Ceramics International 39 (2013) 7107–7113.

[173] Kaur R, Pal B. Cu nanostructures of various shapes and sizes as superior catalysts for nitro-aromatic reduction and co-catalyst for Cu/TiO_2 photocatalysis Applied Catalysis A: General 491 (2015) 28–36.

[174] Eisel C, Tausch MW. Molecular hydrogen from hydrochloric acid and copper under UV light irradiation. Journal of Photochemistry and Photobiology A: Chemistry 128 (1999) 151–154.

[175] Horváth O. Photochemistry of copper(I) complexes. Coordination Chemistry Reviews 135–136 (1994) 303–324.

[176] Litter MI. Heterogeneous photocatalysis: Transition metal ions in photocatalytic systems. Applied Catalysis B: Environmental 23 (1999) 89–114.

[177] Davis DD, Stevenson KL, Davis CR. Photooxidation of dichloro- and trichlorocuprate(I) ions in acid solution. Journal of American Chemical Society 100 (1978) 5344–5349.

[178] Chiarello GL, Di Paola A, Palmisano L, Selli E. Effect of titanium dioxide crystalline structure on the photocatalytic production of hydrogen. Photochemical & Photobiological Sciences 10 (2011) 355–360.

[179] Reklaitis GV, Ravindran A, Regsdell KM. Engineering Optimization. Wiley, New York, 1983.

[180] Park JY, Renzas JR, Hsu BB, Somorjai GA. Interfacial and chemical properties of Pt/TiO_2, Pd/TiO_2, and Pt/GaN catalytic nanodiodes influencing hot electron flow. Journal of Physical Chemistry C 111 (2007) 15331-15336.

[181] Subramanian V, Wolf EE, Kamat P. Catalysis with TiO_2/gold nanocomposites: effect of metal particle size on the Fermi level equilibration. Journal of American Chemical Society 126 (2004) 4943–4950.

[182] Zhou X, Liu G, Yu J, Fan W. Surface plasmon resonance-mediated photocatalysis by noble metal-based composites under visible light. Journal of Materials Chemistry 22 (2012) 21337–21354.

[183] Zhang X, Chen YL, Liu RS, Tsai DP. Plasmonic photocatalysis. Reports on Progress in Physics 76 (2013) 046401.

[184] Warren SC, Thimsen E. Plasmonic solar water splitting. Energy & Environmental Science 5 (2012) 5133–5146.

[185] Koca A, Sahin M. Photocatalytic hydrogen production by direct sun light from sulfide/sulfite solution. International Journal of Hydrogen Energy 27 (2002) 363–367.

[186] Lee K, Nam WS, Han GY. Photocatalytic water-splitting in alkaline solution using redox mediator. 1: parameter study. International Journal of Hydrogen Energy 29 (2004) 1343–1347.

[187] Bamwenda GR, Arakawa H. The photoinduced evolution of suspension O_2 and H_2 from a WO_3 aqueous suspension in the presence of Ce^{4+}/Ce^{3+}. Solar Energy Materials for Solar Cells 70 (2001) 1–14.

[188] Kuhn HJ, Braslavsk SE, Schmidt R. Chemical actinometry (IUPAC Technical Report). Pure and Applied Chemistry 76 (2004) 2105–2146.

[189] Zepp RG, Gumz MM, Miller WL, Gao H. Photoreaction of valerophenone in aqueous solution. Journal of Physical Chemistry, A, 102 (1998) 5716–5723.